

AFRL-ML-WP-TR-1999-4173

**PHOTO-ASSISTED CHEMICAL
BEAM EPITAXY FOR DIRECT
WRITE EPITAXY**



**B.Q. SHI
C.W. TU**

**DEPARTMENT OF ELECTRICAL AND COMPUTER ENGINEERING
UNIVERSITY OF CALIFORNIA, SAN DIEGO
9500 GILMAN DRIVE
LA JOLLA, CA 92093-0407**

AUGUST 1999

FINAL REPORT FOR 09/01/1995 – 07/08/1999

APPROVED FOR PUBLIC RELEASE; DISTRIBUTION UNLIMITED

**MATERIALS AND MANUFACTURING DIRECTORATE
AIR FORCE RESEARCH LABORATORY
AIR FORCE MATERIEL COMMAND
WRIGHT-PATTERSON AIR FORCE BASE OH 45433-7750**

DTIC QUALITY INSPECTED 4

20000901 073

NOTICE

USING GOVERNMENT DRAWINGS, SPECIFICATIONS, OR OTHER DATA INCLUDED IN THIS DOCUMENT FOR ANY PURPOSE OTHER THAN GOVERNMENT PROCUREMENT DOES NOT IN ANY WAY OBLIGATE THE US GOVERNMENT. THE FACT THAT THE GOVERNMENT FORMULATED OR SUPPLIED THE DRAWINGS, SPECIFICATIONS, OR OTHER DATA DOES NOT LICENSE THE HOLDER OR ANY OTHER PERSON OR CORPORATION OR CONVEY ANY RIGHTS OR PERMISSION TO MANUFACTURE, USE, OR SELL ANY PATENTED INVENTION THAT MAY RELATE TO THEM.

THIS REPORT IS RELEASEABLE TO THE NATIONAL TECHNICAL INFORMATION SERVICE (NTIS). AT NTIS, IT WILL BE AVAILABLE TO THE GENERAL PUBLIC, INCLUDING FOREIGN NATIONS.

THIS TECHNICAL REPORT HAS BEEN REVIEWED AND IS APPROVED FOR PUBLICATION.



WILLIAM C. MITCHEL, Project Engineer
Sensor Materials Branch
Survivability & Sensor Materials Division



ROBERT L. DENISON, Chief
Sensor Materials Branch
Survivability and Sensor Materials Division



WILLIAM R. WOODY, Chief
Survivability and Sensor Materials Division
Materials & Manufacturing Directorate

Do not return copies of this report unless contractual obligations or notice on a specific document require its return.

REPORT DOCUMENTATION PAGE			Form Approved OMB No. 0704-0188	
Public reporting burden for this collection of information is estimated to average 1 hour per response, including the time for reviewing instructions, searching existing data sources, gathering and maintaining the data needed, and completing and reviewing the collection of information. Send comments regarding this burden estimate or any other aspect of this collection of information, including suggestions for reducing this burden, to Washington Headquarters Services, Directorate for Information Operations and Reports, 1215 Jefferson Davis Highway, Suite 1204, Arlington, VA 22202-4302, and to the Office of Management and Budget, Paperwork Reduction Project (0704-0188), Washington, DC 20503.				
1. AGENCY USE ONLY (Leave blank)	2. REPORT DATE AUGUST 1999	3. REPORT TYPE AND DATES COVERED FINAL REPORT FOR 09/01/1995 - 07/08/1999		
4. TITLE AND SUBTITLE PHOTO-ASSISTED CHEMICAL BEAM EPITAXY FOR DIRECT WRITE EPITAXY		5. FUNDING NUMBERS C F33615-95-C-5441 PE 62102 PR 4348 TA 71 WU 05		
6. AUTHOR(S) B.Q. SHI C.W. TU				
7. PERFORMING ORGANIZATION NAME(S) AND ADDRESS(ES) DEPARTMENT OF ELECTRICAL AND COMPUTER ENGINEERING UNIVERSITY OF CALIFORNIA, SAN DIEGO 9500 GILMAN DRIVE LA JOLLA, CA 92093-0407		8. PERFORMING ORGANIZATION REPORT NUMBER TU-AFWL-99		
9. SPONSORING/MONITORING AGENCY NAME(S) AND ADDRESS(ES) MATERIALS AND MANUFACTURING DIRECTORATE AIR FORCE RESEARCH LABORATORY AIR FORCE MATERIEL COMMAND WRIGHT-PATTERSON AFB, OH 45433-7750 POC: WILLIAM C. MITCHEL, AFRL/MLPO, 937-255-4474 EXT. 3252		10. SPONSORING/MONITORING AGENCY REPORT NUMBER AFRL-ML-WP-TR-1999-4173		
11. SUPPLEMENTARY NOTES				
12a. DISTRIBUTION AVAILABILITY STATEMENT APPROVED FOR PUBLIC RELEASE, DISTRIBUTION UNLIMITED.		12b. DISTRIBUTION CODE		
13. ABSTRACT (Maximum 200 words) <p>Deposition of thin epitaxial films is required for the fabrication of many microelectronic devices. Often, these layers must be patterned by photolithographic processes, whereupon further layers are deposited to build up complex structures. Selected-area growth of thin films would greatly simplify this procedure. Consequently, there has been considerable interest in laser-assisted direct-write epitaxy.</p> <p>It is known that an argon ion laser, compared to an excimer laser, is easier to operate and does not cause the problem of plastic deformation of crystal lattices associated with large thermal stresses. In this report, an Ar⁺⁺-laser (488 nm) is used to assist metalorganic (chemical beam epitaxy of phosphides and doped GaAs. In addition, results from Ar⁺⁺-laser assisted epitaxy are analyzed.</p> <p>Lateral variations in growth rates, doping levels and compositions of epitaxial layers have been successfully induced with laser irradiation. To investigate the mechanisms responsible for the observed laser-induced effects, numerical models for chemical beam epitaxy have been developed in this work. It is demonstrated that properly combining reaction schemes derived from surface-science desorption studies enables us to predict well the growth rate and doping concentration without adjustable parameters. Based on analyses of simulated variations of concentrations of surface species with temperature, it is found that photo-decomposition of adsorbed group-III and dopant species, along with laser-induced temperature rise, is responsible for growth-rate and doping enhancements.</p> <p style="text-align: right;">(continued)</p>				
14. SUBJECT TERMS GaAs, Inp, InGaP, argon ion laser, MOMBE, CBE, Si, Cargon, doping, simulation, kinetic model		15. NUMBER OF PAGES 166		
		16. PRICE CODE		
17. SECURITY CLASSIFICATION OF REPORT UNCLASSIFIED	18. SECURITY CLASSIFICATION OF THIS PAGE UNCLASSIFIED	19. SECURITY CLASSIFICATION OF ABSTRACT UNCLASSIFIED	20. LIMITATION OF ABSTRACT SAR	

13. Abstract (continued)

Numerical simulation reveals that site-blocking effects of surface group-V species control the surface coverage of group-III and dopant species. Photo-decomposition pathways of surface species upon absorption of visible-wavelength photons are discussed. The criteria for selecting precursors of appropriate chemical-physics properties in order to maximize laser-induced doping enhancements are proposed.

TABLE OF CONTENTS

Section	Page
TABLE OF CONTENTS.....	iii
LIST OF FIGURES.....	vii
LIST OF TABLES.....	xiii
Chapter 1. PROGRAM INTRODUCTION.....	1
1.1 Program Motivations.....	1
1.2 Program Aims and Approaches.....	3
1.3 Outline of this Report.....	5
References.....	7
Chapter 2. A KINETIC MODEL FOR TRIETHYLGALLIUM SURFACE CHEMISTRY.....	8
2.1 Introduction.....	8
2.2 Triethylgallium Surface-Decomposition Reactions.....	8
2.3 Formulation of Reaction Kinetics.....	11
2.4 Summary.....	15
References.....	18
Chapter 3. A KINETIC MODEL FOR TRIS(DIMETHYLAMINO)ARSENIC DECOMPOSITION ON GaAs SURFACES.....	19
3.1 Introduction.....	19
3.2 Review of Experimental Studies on TDMAAs Decomposition on GaAs(100)....	20
3.3 Reaction Mechanism and Assumptions on Arrhenius Parameters.....	22
3.4 Modeling Results.....	25

3.5 Discussion.....	28
3.6 Conclusion.....	30
References.....	33
Chapter 4. A REACTION MODEL FOR CHEMICAL BEAM EPITAXY WITH TRIETHYLGALLIUM AND TRIS(DIMETHYLAMINO)ARSENIC.....	35
4.1 Introduction.....	35
4.2 Reaction Schemes for TEGa and TDMAs Interactions on GaAs Surfaces.....	36
4.3 Simulation, Experiment and Comparison.....	38
4.4 Summary.....	45
References.....	48
Chapter 5. EVALUATIONS OF Ar⁺-LASER INDUCED TEMPERATURE RISE OF SEMICONDUCTOR SURFACES.....	49
5.1 Introduction.....	49
5.2 Solutions of a Heat diffusion equation for semiconductors.....	50
5.3 Calculation of Laser-Induced Temperature Rise.....	56
5.4 Summary.....	63
References.....	64
Chapter 6. INVESTIGATIONS ON THE MECHANISMS RESPONSIBLE FOR Ar⁺-LASER INDUCED GaAs GROWTH ENHANCEMENTS.....	65
6.1 Introduction.....	65
6.2 Simulation of Ar ⁺ -Laser-Induced Pyrolytic Effects.....	67
6.3 Evaluation of Laser-Enhanced Catalytic Effects.....	69

6.4 Investigation on Ar ⁺ -Laser-Induced Photolytic effects.....	72
6.5 Summary.....	80
References.....	82
Chapter 7. MODELING STUDY OF SILICON INCORPORATION	
FROM SiBr₄ IN GaAs LAYERS GROWN BY	
CHEMICAL BEAM EPITAXY.....	83
7.1 Introduction.....	83
7.2 Experimental Methods.....	84
7.3 Analyses of Si Incorporation from SiBr ₄	86
7.4 Results and Discussion.....	89
7.5. Summary.....	91
References.....	93
Chapter 8. EXPERIMENTAL AND NUMERICAL STUDIES OF Ar⁺-LASER	
ASSISTED Si DOPING OF GaAs WITH SiBr₄ BY	
CHEMICAL BEAM EPITAXY.....	94
8.1 Introduction.....	94
8.2 Experimental Methods.....	95
8.3 Results and Discussion.....	97
8.4 Summary.....	103
References.....	106
Chapter 9. LASER-ASSISTED CBE GROWTH OF PHOSPHIDES	
.....	107
9.1 Introduction.....	107
9.2 Chemical Beam Epitaxy of InP with Ar ⁺ Laser Irradiation.....	107

9.3 Ar ⁺ -Laser Assisted CBE of GaInP.....	117
9.4 Summary.....	119
References.....	123
Chapter 10. ACCOMPLISHMENT SUMMARY AND	
RECOMMENDATIONS.....	124
10.1 Accomplishments.....	124
10.2 Recommendations.....	125
Appendix A. CHEMICAL BEAM EPITAXY OF AIAs USING	
NOVEL GROUP-V PRECURSORS.....	128
A1 Introduction.....	128
A2 Experimental Methods.....	130
A3 Results and Discussion.....	131
A4 Summary.....	136
References.....	139
Appendix B. EFFECTS OF Ar⁺ LASER AND HYDROGEN ATOMS ON	
CARBON DOPING OF GaAs WITH CBr₄.....	140
B1 Introduction.....	140
B2 Experimental Methods.....	140
B3 Results and Discussion.....	141
B4 Summary.....	143
References.....	147
Appendix C. PUBLICATIONS AND PRESENTATIONS.....	148
C1 Publications.....	148
C2 Presentations.....	149

LIST OF FIGURES

Page		Figure
2.1.	Triethylgallium Surface Chemistry.....	9
2.2.	Hydrocarbon Surface Chemistry.....	10
2.3.	Calculated Surface Coverage During a TPD Sweep.....	16
3.1.	TDMAAs Surface Chemistry.....	23
3.2.	Calculated TPD Spectrum for Initial TDMAAs Coverage of 0.5 ML and Heating Rate of 2K/s.....	28
3.3.	Schematic Drawing of the Experimental TPD Data Reported in the Paper by Xi, et al. [3.14] for Summation of Signals m/e=44 and m/e=45 (Dotted Line) and Summation of Signals m/e=42 and m/e=43 (Solid Line).....	30
3.4.	Calculated Relative Desorption Fluxes Under CBE Conditions (Lines) and Measured Relative Desorption Intensities (Data Points).....	31
3.5.	Calculated Surface Coverage During a TPD Sweep.....	32
3.6.	Calculated Steady-state Surface Coverage Under CBE Conditions.....	32
4.1.	As-controlled Growth Rate as a Function of Substrate Temperature.....	41
4.2.	Growth Rate as a Function of Substrate Temperature	42
4.3.	Growth Rate as a Function of Substrate Temperature	44
4.4.	Calculated Sensitivity Coefficients $\frac{A_i}{R_g} \frac{\Delta R_g}{\Delta A_i}$ of Reactions (2-5) and (11) of Table 4.1. ΔR_g is the Change in the Growth Rate Corresponding to a Change in the Pre-exponential Factor of the i^{th} Reaction by ΔA_i	45

4.5.	Growth Rate as a Function of Substrate Temperature Under Two Sets of Growth Conditions.....	46
4.6.	Surface Coverage as a Function of Substrate Temperature During GaAs Growth with Incident Fluxes of Fig. 4.2.....	47
4.7.	Time as a Function of Substrate Temperature for the Growth to Reach a Steady State with Incident Fluxes of Fig. 4.3 (Solid Curve).....	47
5.1.	Schematic Diagram of the CBE System and Laser Optics Used in this Study.....	49
5.2.	Schematic Diagram of Gaussian Intensity Distribution of a Laser Beam.....	51
5.3.	Schematic Diagram of the z Coordinate.....	52
5.4.	Calculated Surface Temperature Rises at the Center of a 488nm Stationary Laser Beam. Laser power is 4 W.....	58
5.5.	Calculated Surface Temperature Rises at Center of the Area Scanned by a 488 nm Laser Beam	60
5.6.	Calculated Surface Temperature Rise at Center of the Area Scanned by a 488 nm Laser Beam	61
5.7.	Calculated Surface Temperature Rise at Center the Area Scanned by a 488 nm Laser Beam.....	62
5.8.	Calculated Surface Temperature Rises at Ccenter the Area Scanned by a 488 nm Laser Beam	63
6.1.	Measured Growth Rate of GaAs by CBE Using TEGa and TDMAAs without Laser Irradiation (Open Square) and with Laser Irradiation (Solid Star) [6.1].....	66

6.2.	Comparison Between Simulated and Observed Growth Enhancement.....	68
6.3.	Growth Rates With Simulated Steady-state Surface Coverage of Normal Growth at Temperature 20 °C Higher than (Solid Line) and at the Same Temperature (Solid Square) as the Substrate Temperature as Initial Conditions	70
6.4.	Illustration of Drift Hole Current and Thermionic Electron Current for n-type GaAs.....	71
6.5.	Schematic Illustration of Multi-layer Adsorption on a Substrate Surface.....	73
6.6.	Calculated Coverage of TDMAAs (Dashed Line) and TEGa (Solid Line) in the Second Adsorption Layer as a Function of Substrate Temperature.....	76
6.7.	Temporal Average of DEGa Coverage (Solid Curve) and Irradiation-density Weighted Temporal Average of DEGa Coverage (Dotted Curve) from Simulation of Scanning-Ar ⁺ -laser Assisted Growth at the Center of the Scanned Area.....	79
6.8.	Temporal Averages of Surface Coverages of Arsenic (Dotted Line), Mono(dimethylamino)arsenic (Solid Line+Square) and Diethylgallium (Solid Line) as a Function of Substrate Temperature from Simulation of Laser-assisted Growth.....	81
7.1.	Data Points used to Obtain (E_a -Q) and A_3 . The straight line is for fitting.	90
7.2.	Comparison Between Predicted Dopant Concentration and Measured Net Carrier Concentration at Various Growth Conditions.....	92
8.1.	Measured Carrier Concentrations at Different Substrate Temperatures With	

	and Without Laser Irradiation	99
8.2.	Hall Mobility of Samples Grown With and Without Laser Irradiation.....	102
8.3.	Ratios of Carrier Concentrations in Films Grown With Laser to Those Grown Without Laser Irradiation at Different Substrate Temperatures.....	103
8.4.	Simulated Variation of Total Surface Coverage and Dissociative Chemisorption Rate with Substrate Temperature.....	105
8.5.	Simulated Surface Coverage of Physisorbed SiBr_4 as a Function of Substrate Temperature.....	106
9.1.	Variation of RHEED Intensity at (00) Rod on (1 -1 0) Recording Plane while Overlapping of Laser and e-beam is being Reached.....	109
9.2.	Surface Reconstruction Patterns on (1 -1 0) Recording Plane Without Laser (a) and With Laser (b).....	110
9.3	RHEED Intensity Oscillations Without Laser (Dashed Line) and With Laser (Solid Line).....	111
9.4	RHEED Intensity Variation Recorded During a Growth Run at 207 °C. The Normal Vector of the Recording Plane was (1 1 0).	113
9.5.	Growth Rates With and Without Laser Irradiation. The Three Data at Temperatures Lower than 250 °C were from Correction of Measured Growth Rates for Viewport Coating Condition.....	115
9.6.	Photoluminescence Spectra of Films Grown With Laser (Solid Lines) and Without Laser (Dashed Lines) at Various Substrate Temperatures ($T_s = 370^\circ\text{C}$, 420°C , and 450°C).....	116
9.7.	X-ray Rocking Curves of Non-irradiated (Dashed Line) and Laser-irradiated Films (Solid Line) of the Sample Grown at 450°C	117

9.8.	(400)-Lattice-plane X-ray Rocking Curves of Non-irradiated (Fig. 8a) and Laser-irradiated GaInP Films (Fig. 8b).....	118
9.9.	Change in Gallium Composition of GaInP Films Resulted from Laser Irradiation at Various Substrate Temperatures.	121
9.10.	Measured Growth Rate as a Function of Substrate Temperature with Laser (Star) and Without Laser (Open Square) Under Growth Conditions of Fig. 9.9.....	122
9.11.	Ratio of Laser-induced Thickness Enhancement to Thickness from Normal Growth.....	122
A1.	Group-III Induced RHEED Intensity Oscillations with 0.2 sccm TMA and 0.95 ML/s Cracked TBA (Upper Diagram) or TDMAAs (Lower Diagram)	132
A2.	Group-III Induced RHEED Intensity Oscillations with 0.2 sccm TMA and 0.95 ML/s Cracked TBA (Upper Diagram) or TDMAAs (Lower Diagram)	134
A3.	RHEED Surface Reconstruction Patterns During Growth with TBA.....	135
A4.	Variation of Growth Rate with TMA Flow Rate While TDMAAs Flux is Fixed at 0.95 ML/s	136
A5.	Growth Rates with Different TDMAAs Incident Fluxes and 0.95 sccm (Solid Square) or 0.75 sccm TMA (Empty Square).	137
A6.	Hole Concentration and Mobility Data of Samples Grown.	138
B.1.	RHEED Observation of Atomic Hydrogen Cleaning of GaAs.	142
B.2.	Measured Net-carrier Concentration as a Function Of Substrate Temperature Without (Plus) and With (Solid Square) H-atom Irradiation of	

	Growing Surface.....	144
B.3.	Measured Net-carrier Concentration from Growth Runs of 300 W/cm ² Ar ⁺ -laser Irradiation Without (Plus) and With (Solid Square) H Atoms from H ₂ Cracker.....	145
B.4.	Measured Mobility of the Samples for which the Carrier Concentrations are Plotted in Figs. B.2 and B.3.....	146

LIST OF TABLES

Table 2.1.	Reaction scheme For TEGa decomposition.....	11
Table 2.2.	Rate equations For TEGa decomposition.....	17
Table 3.1.	Reaction Scheme for TDMAAs decomposition.....	22
Table 5.1.	Constants used in calculations of laser-induced temperature rise in GaAs.....	57
Table 6.1.	Constants used in calculations of TEGa and TDMAAs coverage in the second adsorption layer.....	75

CHAPTER 1

PROGRAM INTRODUCTION

1.1 Program motivations

Molecular beam epitaxy (MBE) [1.1], metalorganic vapor-phase epitaxy (MOVPE) [1.2] and chemical beam epitaxy (CBE) [1.3] have been successfully used to synthesize high-quality III-V compound semiconductor materials. Metalorganic precursors are used both in MOVPE and CBE, unlike MBE which employs vapors of atoms from furnaces of solid-phase sources. In MOVPE and CBE, pyrolytic decomposition of metalorganic precursors leads to formation of constituent atoms for growth of materials. The main difference between MOVPE and CBE is that CBE utilizes ultra-high vacuum systems and the chamber pressure during growth is typically 10^{-5} Torr, while the MOVPE growth pressure is larger than 10^{-2} Torr and can be as large as the atmosphere pressure. The consequence of this difference is that gas-phase collisions between gas molecules in a CBE chamber are negligible and pyrolytic decomposition occurs almost only on a heated wafer surface, while in an MOVPE reactor, decomposition can occur both in the gas-phase and on the surface. Because of negligible collisions between molecules inside a CBE chamber, the precursor molecules effusing from an injector of the chamber impinge on substrates as a beam. The beam nature of CBE precursors brings about monolayer abruptness and thickness control for growth of compound semiconductor heterostructures.

Deposition of thin epitaxial films is required for the fabrication of many microelectronic devices. Often, these layers must be patterned by photolithographic processes, whereupon further layers are deposited to build up complex structures. Selected-area growth of thin films would greatly simplify this procedure. Consequently, there has been a considerable interest in using lasers to stimulate, overlocalized areas, decomposition of metalorganic species for growth and doping by CBE or MOVPE.

It is known that an argon ion laser, compared to an excimer laser, is easier to operate and does not cause the problem of plastic deformation of the crystal lattice associated with large thermal stresses. Also, use of laser beams as the stimulation energy source in MOVPE reactors encounters complications due to Rayleigh scattering [1.4] of the laser beams by gas molecules and dispersion of possible gas-phase photogenerated intermediate products. Therefore, there have been many reports in the literature on Ar⁺-laser-enhanced growth by CBE [1.5-1.18].

Sugiura et al. [1.5-1.9] investigated Ar⁺-laser-assisted CBE of GaAs using triethylgallium (TEGa) and cracked AsH₃ as precursors. With 400 W/cm² power density, they observed growth-rate enhancements in the substrate temperature range from 350 °C to 500 °C. Haike et al. [1.10-1.12] reported growth enhancements in the growth temperature range of 250 °C to 500 °C using 400 W/cm² power density and TEGa and tris(dimethylamino)arsenic (TDMAs) as precursors for Ar⁺-laser-assisted CBE of GaAs. It was noted in those reports, as a straightforward observation, that the growth-rate enhancements could not be accounted for by the estimated laser-induced temperature rises (20 °C~ 25 °C). On the other hand, Haike et al. [1.12-1.14] found that growth-rate changes resulting from the substrate temperature rise due to 400 W/cm² Ar⁺-laser irradiation could explain the observed growth rate enhancements in the case of the group-V species being As₄ from an effusion cell of solid arsenic.

In one of the studies conducted by Sugiura et al. [1.5], no dependence of the GaAs growth rate enhancement on the substrate type (n-type, p-type or semi-insulating) was observed, indicating no effect on the enhancement of the band bending which might facilitate transport of photogenerated electrons or holes to the growing surface. They concluded that catalytic (electrochemical) reactions involving photogenerated carriers could be ruled out as the mechanisms responsible for the observed growth enhancement and postulated that the mechanisms responsible for the growth rate enhancement were of a photolytic nature. However, there were several important questions unanswered, such as, 1) what physical processes dictate the temperature window for growth enhancement ? 2) which species undergo photodecomposition, the intermediate decomposition products or the parent molecules? and where are they, in the physisorption state or chemisorption

state? 3) how large would the photoabsorption cross sections have to be to account for the enhancement? and 4) what are the likely photodecomposition reaction pathways? In addition, the issue of why photoinduced carriers had a negligible effect on rates at which semi-insulating GaAs layers grew with Ar⁺-laser irradiation was not addressed in the report by Sugiura et al. [1.5].

Besides the theoretical questions raised above for explanation of observed GaAs growth-rate enhancements, there were important experiments which needed to be carried out in order to realize the full potential of Ar⁺-laser assisted CBE. Haike et al. [1.11, 1.13] experimented Ar⁺-laser-induced selected-area doping using disilane (Si₂H₆) as the dopant precursor by CBE. The maximum doping enhancement ratio they achieved was only 3.2. Therefore, there was a need to investigate whether it was possible and how to obtain larger doping enhancement ratios using Ar⁺-laser stimulation. Iga et al. [1.15] measured the thickness of InP films grown by CBE with trimethylindium (TMIn) or triethylindium (TEIn), cracked phosphine and a CW argon ion laser. With TMIn, they found occurrence of growth-rate enhancement by laser irradiation in the substrate temperature range of 350-480 °C. However, the substrate temperature was varied only in the range of 350-525 °C and the temperature window for growth-enhancement was not explored. Iga et al. [1.16] and Haike et al. [1.12-1.13, 1.17-1.18] demonstrated that Ar⁺ lasers could induce lateral variations in the indium composition of InGaAs ternary layers grown on InP or GaAs substrates. There was a need to extend the Ar⁺-laser assisted CBE work to the case of InGaP layers, since InGaP has many advantages over Al_{0.3}Ga_{0.7}As, e.g., having no DX centers, which is advantageous for high electron-mobility transistors (HEMTs); smaller ΔE_c and larger ΔE_v , which is good for heterojunction bipolar transistors (HBTs); a higher breakdown field; and a good etching selectivity over GaAs.

1.2 Program aims and approaches

The aims of this study are 1) to perform additional experiments of Ar⁺-laser assisted epitaxy; 2) to develop adsorption, growth and doping models for simulating surface chemistry of CBE; 3) to develop models for evaluating Ar⁺-laser induced temperature rises and free carriers on the surface of substrates; and 4) to demonstrate involvement of and to obtain description of the surface photochemical processes in Ar⁺-laser assisted CBE.

The experiments carried out in this study would further explore the potential of Ar⁺-laser assisted CBE. Also, the experimental data collected in this study provide data additional to those already reported in the literature for understanding of the mechanisms responsible for laser-induced effects. The setup of the CBE system has been described elsewhere [1.13, 1.19]. The films grown in this study were characterized by Dektak stylus profiler, photoluminescence, double-crystal X-ray diffraction and/or van der Pauw-Hall measurements.

Since photodecomposition rates of surface species are functions of their surface coverage, it is imperative to look quantitatively into the concentrations of precursors and their intermediate decomposition products in chemisorption or physisorption state under CBE growth conditions. Models, therefore, have been developed for simulating adsorption and reactions of CBE precursors on surfaces with dangling bonds. The models are based on 1) surface science studies reported in the literature, 2) thermodynamic properties of metalorganic species, and 3) CBE growth data collected in this study or reported in the literature. Furthermore, properly combining reaction mechanisms of individual species enables us to predict the growth rate and doping concentration. In this study, the growth and doping models are applications oriented with data readily available to CBE crystal growers as inputs. Comparisons between simulations and experiments provide verification of and feedback to the models.

To investigate the physical and chemical mechanisms responsible for observed laser-induced effects, it is also imperative to evaluate laser-induced temperature rises and

concentrations of photogenerated carriers on wafer surfaces. Heat diffusion differential equations are solved in this study. Detailed parameterization formula of semiconductor properties from the literature are used as inputs to calculate pyrolytic effects of Ar⁺-laser irradiation on the growth rate and the doping concentration. Ar⁺-laser-generated carrier concentrations are also examined in details in this study with surface recombination taken into account.

The dominant photolytic reactions occurring in laser-assisted CBE are based on 1) calculation of pyrolytic effects associated with Ar⁺-laser irradiation; 2) the correlation between simulated variations of concentrations of surface species with temperature and observed temperature windows of growth and doping modifications; 3) the Ar⁺-laser photon energy and bond strengths of metalorganic species; 4) gas-phase photochemistry and absorption cross sections of metalorganic species; and 5) the photo absorption cross sections required to reproduce the observed modifications. The end products of this investigation include 1) a fundamental understanding of Ar⁺-laser-induced effects on CBE, 2) criteria for selecting precursors of appropriate chemical-physics properties for laser-assisted syntheses of solid-state materials and 3) efficient and intelligent designs of growth conditions for direct-write syntheses of solid-state materials using lasers.

1.3 Outline of this report

In Chapters 2 and 3, development of reaction models for TEGa and TDMAAs thermal decomposition on GaAs(100) surfaces, based on surface-science studies, will be presented, respectively. Mathematical formulation utilizing principals of chemical physics for numerical simulation of the nonlinear reaction systems will be rigorously derived. Chapter 4 will be about how to properly combine surface decomposition models for individual species to develop a CBE growth model with TEGa and TDMAAs as precursors. Procedures will also be developed in Chapter 4 for using tools readily available to crystal growers to obtain inputs to the growth model. In Chapter 5, surface temperature rise associated with laser irradiation of substrates will be investigated. A general solution to the heat diffusion equation and a computational model specific for the

experimental setup of this study will be reported. Implications of the results from temperature-rise calculation will be discussed for the purpose of better simulating pyrolytic effects of laser irradiation on surface chemistry. Chapter 6 will utilize models developed in previous chapters to investigate the mechanisms responsible for Ar^+ -laser induced growth enhancement of GaAs. Calculation will also be performed there to obtain amount of precursors in the physisorption state and surface excess carriers associated with laser irradiation. A model for simulating dopant concentrations resulted from Si doping of GaAs with SiBr_4 will be presented in Chapter 7. Since dopant precursors are typically tracer species in comparison to those for growth, it will be shown that growth models can be used as platforms for constructing doping models. Results from laser-assisted Si doping of GaAs with SiBr_4 will be analyzed in Chapter 8. The mechanism responsible for doping enhancement with Ar^+ -laser irradiation will be looked into with the doping model of Chapter 7. Chapter 9 will consist of experimental results from Ar^+ -laser assisted CBE of InP and GaInP as well as those from Ar^+ -laser-assisted and/or H-atom-assisted carbon doping of GaAs with CBr_4 by CBE. It will be shown there that results of Chapter 9 corroborate conclusions drawn in previous chapters.

References

- [1.1] A. Y. Cho and J. R. Arthur, *Prog. Solid State Chem.* **10**, 157 (1975).
- [1.2] G. B. Stringfellow, *Organometallic Vapor-Phase Epitaxy: Theory and Practice*, Academic Press, Inc., San Diego, California (1989).
- [1.3] W. T. Tsang, *Appl. Phys. Lett.* **45**, 1234 (1984).
- [1.4] J. H. Seinfeld, *Atmospheric Chemistry and Physics of Air Pollution*, Section 7.5, John Wiley & Sons, Inc. (1986).
- [1.5] H. Sugiura, R. Iga, T. Yamada, and M. Yamaguchi, *Appl. Phys. Lett.* **54** (4), 335-337 (1989).
- [1.6] H. Sugiura, T. Yamada and R. Iga, *Jpn. J. Appl. Phys.* **29** (1), L1-L3 (1990).
- [1.7] T. Yamada, R. Iga and H. Sugiura, *Jpn. J. Appl. Phys.*, L1883-L1885 (1989).
- [1.8] R. Iga, H. Sugiura and T. Yamada, *Appl. Phys. Lett.* **55** (5), 451-453 (1989).
- [1.9] H. Sugiura, R. Iga and T. Yamada, *J. Cryst. Growth* **120**, 389-394 (1992).
- [1.10] H. K. Dong, N. Y. Li, C. W. Tu, M. Geva and W. C. Mitchel, *Mat. Res. Symp. Proc.* **340**, 173 (1994).
- [1.11] C. W. Tu, H. K. Dong and N. Y. Li, *J. Cryst. Growth* **163**, 187-194 (1996).
- [1.12] C. W. Tu, H. K. Dong and N. Y. Li, *Mat. Chem. & Phys.* **40** (4), 260-266 (1995).
- [1.13] H. K. Dong, *Ph. D Thesis*, University of California, San Diego (1995).
- [1.14] H. K. Dong, B. W. Liang, M. C. Ho, S. Hung and C. W. Tu, *J. Cryst. Growth* **124**, 181-185 (1992).
- [1.15] R. Iga, H. Sugiura and T. Yamada, *Jpn. J. Appl. Phys.* **29**, 475-478 (1990).
- [1.16] R. Iga, H. Sugiura and T. Yamada, *Jpn. J. Appl. Phys.* **30** (1A), L4-L6 (1991).
- [1.17] H. K. Dong, S. C. H. Hung and C. W. Tu, *J. Electron. Mater.* **24**, 327-333 (1995).
- [1.18] H. K. Dong, N. Y. Li and C. W. Tu, *J. Electron. Mater.* **24**, 827-832 (1995).
- [1.19] N. Y. Li, *Ph. D Thesis*, University of California, San Diego (1995).

CHAPTER 2

A KINETIC MODEL FOR TRIETHYLGALLIUM SURFACE CHEMISTRY

2.1 Introduction

There have been a number of surface science studies of the interactions of triethylgallium (TEGa) with GaAs(100) (e.g., [2.1-2.4]). These studies employed a variety of monitoring instruments to identify and probe quantitatively the surface species resulted from deposition of TEGa on GaAs surfaces. Among the instruments typically used were X-ray photoelectron spectroscopy (XPS), temperature programmed desorption (TPD), high resolution electron energy loss spectroscopy (HREELS) and Augur electron spectroscopy (AES). Several authors [2.2, 2.5-2.7] have published kinetic models for decomposition of TEGa on GaAs(100) based on these experimental observations. The reaction model proposed by Foord et al. [2.7] included physical effects, which had been partially or totally neglected in earlier studies, involving surface site blocking due to adsorbed species and lateral interactions between surface species. Their reaction scheme and assumptions on reaction chemical physics are adopted in this study.

2.2 Triethylgallium surface-decomposition reactions

Fig. 2.1 is a schematic diagram of TEGa surface chemistry. For a large molecule such as TEGa at thermal energies, it is reasonable to assume that the trapping probability on the bare part of a surface is unity. This trapping is due to the van der Waals force between surface atoms and TEGa. Molecules attached on a surface by physical forces are called physisorbed molecules [2.8]. Trapped molecules on a surface are most likely located at sites of surface atoms and can move on the surface through hopping motions. A trapped molecule can also evaporate back into the gas phase if it happens to have acquired enough energy. The evaporation pathway as included in Fig. 2.1 is important for TEGa surface chemistry on GaAs(100). During the stay of a TEGa molecule on a

GaAs surface, the interactions between its ligands and dangling bonds of surface atoms can bring about its decomposition. As depicted in Fig. 2.1, the decomposition involves breaking up of one Ga-C₂H₅ bond and formation of bonds of diethylgallium (DEGa) and the breaking-away C₂H₅ radical with surface atoms. Attachments of DEGa and ethyl radicals to surface atoms in the process are similar to chemical reactions and the bonds formed are strong. Their adsorption on the surface is called chemisorption. The decomposition process is reversible, that is, a DEGa and a C₂H₅ radical neighboring each other can recombine with formation of TEGa as the result. Further decomposition of DEGa is much like that of TEGa, involving interactions of the remaining ligands and dangling bonds of surface atoms.

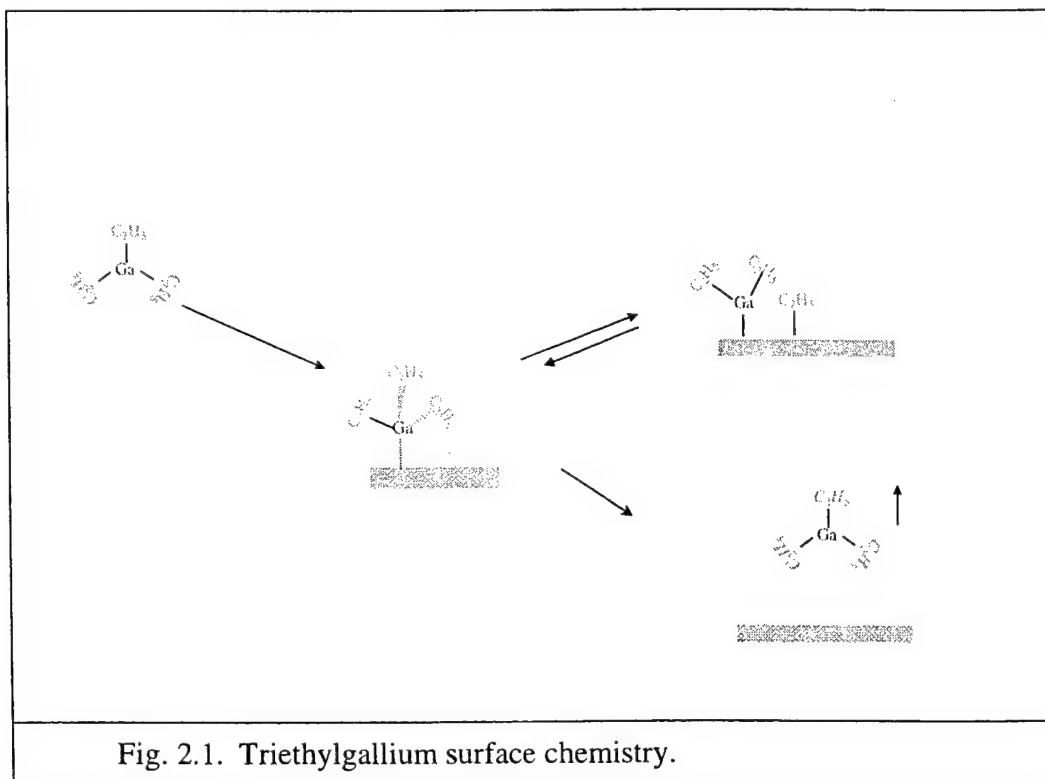


Fig. 2.2 is a schematic diagram of hydrocarbon surface chemistry. An ethyl radical adsorbed on a GaAs surface can undergo a surface hydrogen-transfer reaction with formation of an ethylene (C₂H₄) molecule. The C₂H₄ is either ejected directly into the gas phase or leaves the surface immediately through the evaporation process because

it is weakly physisorbed on the surface. An ethyl radical can also recombine with a surface H atom, if it is present at one of the neighboring surface atoms of the ethyl radical. The fate of the ethane (C_2H_6) molecule resulted from the recombination is similar to that of ethylene from the surface hydrogen-transfer reaction. Two surface hydrogen atoms can also leave the surface as H_2 through a recombination reaction between them when they neighbor each other.

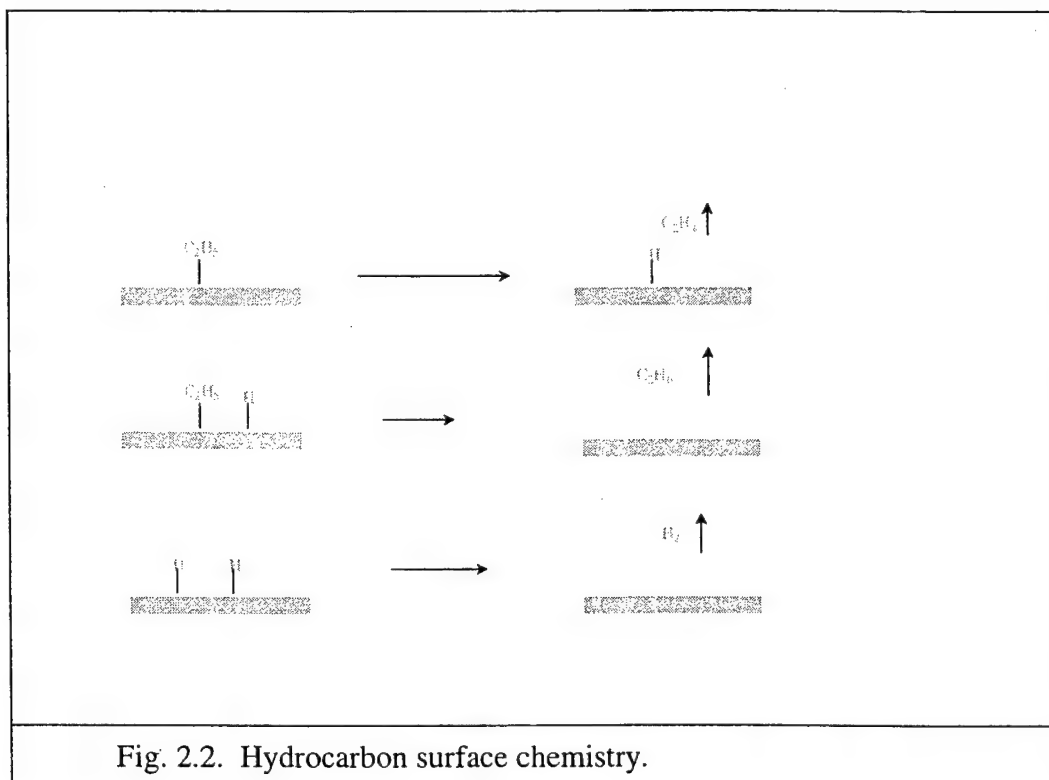


Table 2. 1 lists the full reaction scheme implemented in this study for TEGa decomposition on GaAs (100), where “(ads)” refers to a physisorption or chemisorption state while “(g)” a gas-phase state, and “e.s.” an empty surface site. Surface sites are sites of dangling bonds where adsorption and reactions occur as discussed above. The density of surface sites on a clean GaAs surface is equal to the surface atom density. All reactions that increase the number of surface species are assumed to require the presence of adjacent vacant surface sites. As illustrated in Figs. 2.1 and 2.2, for a bimolecular reaction to occur, the reactants must occupy adjacent sites. Also given in Table 2.1 are

the kinetic parameters for each of the reactions, which will be discussed, along with the concept of Langmuir adsorption kinetics, in the next section.

2.3 Formulation of reaction kinetics

The first reaction of Table 2.1 is the physisorption process of TEGa on a GaAs surface. Assuming that every molecule coming from the gas phase that strikes a molecule already adsorbed on the surface is elastically reflected, the Langmuir adsorption kinetics gives the rate of physisorption:

$$\text{Physisorption rate} = \alpha_0(1-\theta)F_{\text{TEGa}}, \quad (2.1)$$

where α_0 is the condensation coefficient of TEGa on a bare surface, $1-\theta$ the fraction of a surface that is bare and F_{TEGa} is the absolute incident flux of TEGa from the gas phase. The value of α_0 is always close to unity [2.8].

Table 2.1. Reaction Scheme For TEGa decomposition

	$A(s^{-1})$	$E \text{ (kJ/mol)}$
(0) TEGa (g) + e.s. \longrightarrow TEGa (ads)	(a)	0
(1) TEGa (ads) \longrightarrow TEGa (g) + e.s.	10^{11}	50
(2) TEGa (ads) + e.s. \longrightarrow DEGa (ads) + C_2H_5 (ads)	10^{14}	55
(3) DEGa (ads) + C_2H_5 (ads) \longrightarrow TEGa (ads) + e.s.	10^{11}	105
(3a) DEGa (ads) \longrightarrow DEGa (g) + e.s.	10^{14}	165
(4) DEGa (ads) + e.s. \longrightarrow Ga + 2 C_2H_5 (ads)	10^{12}	135
(5) C_2H_5 (ads) \longrightarrow C_2H_5 (g) + H (ads)	10^{12}	147
(6) C_2H_5 (ads) + H (ads) \longrightarrow C_2H_6 (g) + 2 e.s.	10^{14}	165
(7) H(ads) + H(ads) \longrightarrow H_2 (g) + 2 e.s.	10^{13}	126

e.s., an empty site

(ads), adsorbed species

(g), gas-phase species

(a), Langmuir adsorption kinetics

It is a common practice to model the rate of a chemical reaction using an Arrhenius-type expression. In the case of a surface reaction, the Arrhenius expression is

$$\text{Reaction rate} = A (\text{coverage term}) \exp\left(-\frac{E_a}{RT}\right), \quad (2.2)$$

where A is the pre-exponential factor, E_a the activation energy for the reaction and R the gas constant. For a reaction involving only one species, the coverage term is the surface concentration of the species, while for a reaction involving two species, it is the concentration of nearest neighbor pairs of the two species. In Foord et al.'s reaction model [2.7], pairs of adsorbed DEGa occupying adjacent sites are assigned an interaction energy for their lateral repulsion based on surface-science findings. They invoked the quasi-chemical approximation [2.9] to calculate concentrations of nearest neighbor pairs and activation energies of surface reactions. Specifically, within the content of the approximation, the distribution of adsorbed species is assumed to be in equilibrium and for reactions eliminating surface DEGa molecules, the activation energies are dependent on the surface coverage of DEGa because the total energy of the surface is changed by these reactions. The quasi-chemical approximation is also used to derive expressions for reaction rates implemented in this study. Table 2.2 lists the derived reaction rates corresponding to the reactions of Table 2.1. The expressions for Reactions (3), (3a) and (4) in this study are different from those given in Foord et al.'s paper [2.7]. Derivations of the rates of Reactions (3), (3a) and (4) will be shown in details. The expressions for other reactions of Table 2.2 can be obtained following the same arguments.

The following notation is employed. An unoccupied surface site is designated to be O; an occupied site, X, where X is one of the adsorbed species; a pair of near-neighbor sites neither of which is occupied by DEGa, OO; a pair of near-neighbor sites with one of them being occupied by DEGa, DO; a pair of near-neighbor sites filled with DEGa molecules, DD. Surface concentrations, are respectively, N_O , N_X , N_{OO} , N_{DO} and N_{DD} . Assuming that there is no attraction or repulsion between an adsorbed DEGa molecule and an adsorbed H, TEGa or Et, where Et stands for an ethyl radical, we can have

$$\text{The probability of a DO pair being Et-DEGa} = \frac{N_{Et}}{N_{Et} + N_H + N_{TEGa} + N_O}. \quad (2.3)$$

With N_s being the total number of surface sites per unit area, which is equal to $6.4 \times 10^{14} \text{ cm}^{-2}$ for GaAs(100) surfaces, the surface coverage is defined as

$$\theta_x = \frac{N_x}{N_s}, \quad (2.4)$$

The unit of θ_x is monolayer(s) (ML). Utilizing the fact that $N_s = N_{\text{Et}} + N_{\text{H}} + N_{\text{TEGa}} + N_{\text{O}} + N_{\text{DEGa}}$ and Equation (2.3), we can have

$$\text{rate3} = a_3 N_{\text{DO}} \frac{\theta_{\text{Et}}}{(1 - \theta_{\text{DEGa}})} \exp\left(-\frac{E_{a3}}{RT}\right). \quad (2.5)$$

N_{DO} , N_{OO} and N_{DD} are typically normalized as the following:

$$N_{\text{DO}} = \theta_{\text{DO}} Z N_s / 2, \quad N_{\text{OO}} = \theta_{\text{OO}} Z N_s / 2, \quad \text{and} \quad N_{\text{DD}} = \theta_{\text{DD}} Z N_s / 2, \quad (2.6)$$

where Z is the number of near-neighbor sites (4 for a GaAs(100) surface). Defining a_3 as $A_3 Z / 2$, the rate of Reaction (3) in terms of monolayers per second (ML/s) is

$$\text{RATE3} = A_3 \frac{\theta_{\text{DO}} \theta_{\text{Et}}}{(1 - \theta_{\text{DEGa}})} \exp\left(-\frac{E_{a3}}{RT}\right). \quad (2.7)$$

Likewise, we can have the reaction rate in ML/s of Reaction (4)

$$\text{RATE4} = A_4 \frac{\theta_{\text{DO}} \theta_{\text{O}}}{(1 - \theta_{\text{DEGa}})} \exp\left(-\frac{E_{a4}}{RT}\right), \quad (2.8)$$

where $\theta_{\text{O}} = 1 - \theta$, with θ being the total coverage of adsorbed species. For Reaction (3a), since it has only one species on the reactant side, the reaction rate is simply

$$\text{RATE3a} = A_{3a} \theta_{\text{DEGa}} \exp\left(-\frac{E_{a3a}}{RT}\right), \quad (2.9)$$

To derive expressions for θ_{DO} , θ_{OO} , and θ_{DD} , we first note that the normalization conditions [2.9] are:

$$2N_{OO} + N_{DO} = ZN_O \quad (2.10)$$

$$2N_{DD} + N_{DO} = ZN_{DEGa} \quad (2.11)$$

The equilibrium properties of monolayers of adsorbed species can be derived by the use of the grand partition function [2.10]. For the surface adsorption system we are considering,

$$\frac{4N_{OO}N_{DD}}{N_{DO}^2} = \exp\left(\frac{\omega_1}{kT}\right), \quad (2.12)$$

where ω_1 is the decrease in the surface free energy when a new pair of DEGa molecules is removed. Solving Equations (2.10)-(2.12) and using Equation (2.6), we can find that

$$\theta_{DD} = \theta_{DEGa} - \frac{2\theta_{DEGa}(1-\theta_{DEGa})}{1 + \sqrt{1.0 - 4\theta_{DEGa}(1-\theta_{DEGa})\left(1 - \exp\left(\frac{\omega}{RT}\right)\right)}}, \quad (2.13)$$

$$\theta_{OO} = 1 - 2\theta_{DEGa} + \theta_{DD}, \text{ and} \quad (2.14)$$

$$\theta_{DO} = 2(\theta_{DEGa} - \theta_{DD}). \quad (2.15)$$

where $\omega = N_A \omega_1$ and N_A the Avogadro number.

The surface free energy is lowered by the reactions which eliminate DEGa molecules from the surface. The energy due to the repulsion between DEGa molecules is $-\omega_1 N_{DD}$, which is a function of N_{DEGa} . The change in the surface free energy resulted from removal of one DEGa molecule is

$$\omega_1 \frac{dN_{DD}}{dN_{DEGa}} = 0.5Z\omega_1 \left(1 - \frac{1 - 2\theta_{DEGa}}{\sqrt{1.0 - 4\theta_{DEGa}(1-\theta_{DEGa})\left(1 - \exp\left(\frac{\omega}{RT}\right)\right)}} \right). \quad (2.16)$$

In the context of quasi-chemical approximation, the activation energy of Reactions (3) is parameterized as

$$E_{a3} = E_3 + 0.5Z\omega \left(1 - \frac{1 - 2\theta_{\text{DEGa}}}{\sqrt{1.0 - 4\theta_{\text{DEGa}}(1 - \theta_{\text{DEGa}}) \left(1 - \exp\left(-\frac{\omega}{RT}\right) \right)}} \right) \quad (2.17)$$

where E_3 is the activation energy when the surface coverage of DEGa molecules is negligible. Likewise, we can obtain expressions for the activation energies of Reactions (3a) and (4) as shown in Table 2.2.

The values of kinetic parameters listed in Table 2.1 were derived by Foord, et al. [2.7]. The most important criterion used by them in the determination of the kinetic parameters for TEGa decomposition was that the reaction model reproduced satisfactorily the temperature programmed desorption (TPD) and other experimental surface-science data of Murrell et al. [2.2]. It turns out that only when the reaction kinetic data of Table 2.1 are coupled with the rate equations of Table 2.2 derived in this study, can the results published in Foord et al.'s paper [2.7] be reproduced.

Fig. 2.3 shows the computed surface coverage as a function of temperature in a TPD experiment in which 0.5 ML of TEGa is adsorbed on the model surface at low temperatures. We can see that a small amount of TEGa desorbs at low temperatures before the onset of TEGa dissociation into Et and DEGa. The surface concentrations of DEGa and Et then decrease with temperature due to the recombination (Reaction (3)) and desorption (Reaction (1)) of TEGa, but their concentrations remain equal until 500 °C, where DEGa desorption (Reaction (3a)) and decomposition of DEGa to Et plus Ga (Reaction (4)) become important, increasing the Et coverage and decreasing that of DEGa. A small amount of hydrogen is also seen at this temperature from β -elimination of Et. At the end of the TPD desorption sweep only 0.19 ML of Ga has been deposited on the surface, which is otherwise free from adsorbates. We, therefore, see that unlike the case of gallium atoms from a solid Ga source, the TEGa flux incident on a surface can not be directly converted to the rate of Ga incorporation and growth.

2.4 Summary

Thermal decomposition processes of TEGa on GaAs(100) have been described. Reaction rates of the decomposition reactions have been formulated. A numerical model has been developed to simulate TPD of TEGa. Simulation with the model reveals that in principal, the amount of TEGa on a surface can not be equated to that of Ga incorporation resulted from substrate heating.

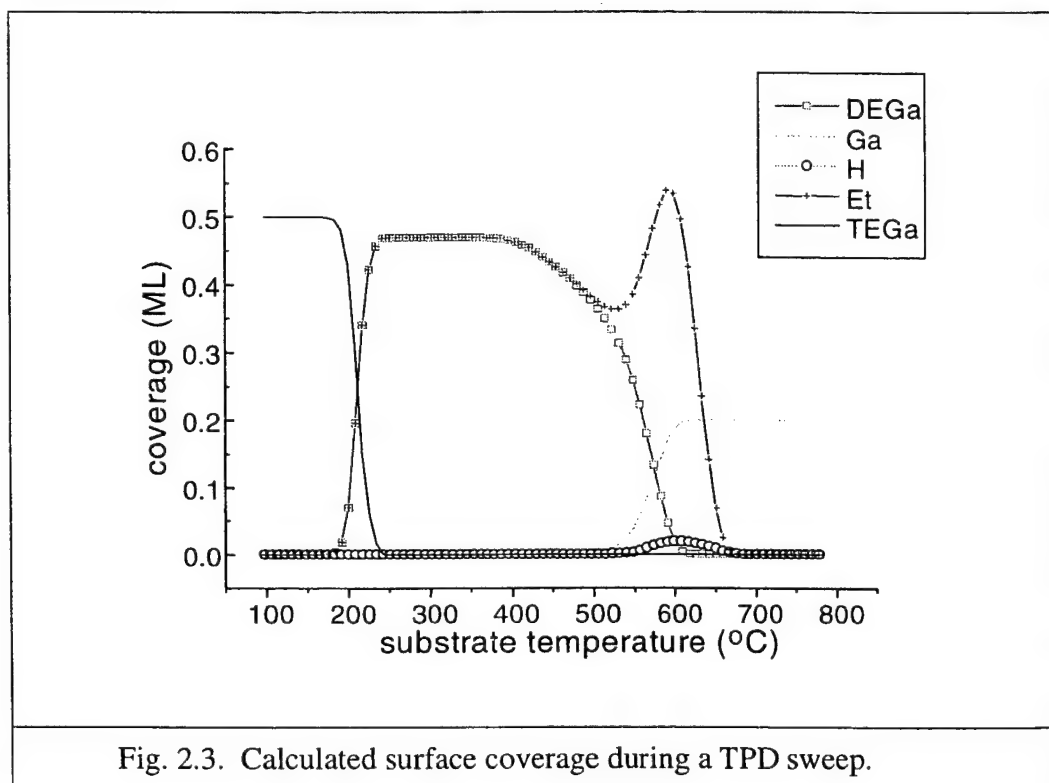


Table 2.2. Rate equations For TEGa decomposition

$$\text{RATE0} = F_{\text{TEGa}} (1 - \theta)$$

$$\text{RATE1} = A_1 \theta_{\text{TEGa}} \exp\left(-\frac{E_1}{RT}\right)$$

$$\text{RATE2} = 2A_2 \frac{\theta_{\text{OO}} \theta_{\text{TEGa}} (1 - \theta)}{(1 - \theta_{\text{DEGa}})^2} \exp\left(-\frac{E_2}{RT}\right)$$

$$\text{RATE3} = A_3 \frac{\theta_{\text{DO}} \theta_{\text{Et}}}{(1 - \theta_{\text{DEGa}})} \exp\left\{-\frac{1}{RT} [E_3 + 0.5Z\omega(1 - \frac{1 - 2\theta_{\text{DEGa}}}{\sqrt{1.0 - 4\theta_{\text{DEGa}}(1 - \theta_{\text{DEGa}})(1 - \exp(\frac{\omega}{RT}))}})]\right\}$$

$$\text{RATE3a} = A_{3a} \theta_{\text{DEGa}} \exp\left\{-\frac{1}{RT} [E_{3a} + 0.5Z\omega(1 - \frac{1 - 2\theta_{\text{DEGa}}}{\sqrt{1.0 - 4\theta_{\text{DEGa}}(1 - \theta_{\text{DEGa}})(1 - \exp(\frac{\omega}{RT}))}})]\right\}$$

$$\text{RATE4} = A_4 \frac{\theta_{\text{DO}} (1 - \theta)}{1 - \theta_{\text{DEGa}}} \exp\left(-\frac{E_4}{RT}\right)$$

$$\text{RATE5} = A_5 \theta_{\text{Et}} \exp\left(-\frac{E_5}{RT}\right)$$

$$\text{RATE6} = 2A_6 \frac{\theta_{\text{OO}} \theta_{\text{Et}} \theta_{\text{H}}}{(1 - \theta_{\text{DEGa}})^2} \exp\left(-\frac{E_6}{RT}\right)$$

$$\text{RATE7} = 2A_7 \frac{\theta_{\text{OO}} \theta_{\text{H}} \theta_{\text{H}}}{(1 - \theta_{\text{DEGa}})^2} \exp\left(-\frac{E_7}{RT}\right)$$

θ , total surface coverage; θ_x , surface coverage of species x;
 θ_{OO} , surface coverage of near-neighbor site pairs with no DEGa;
 θ_{DO} , surface coverage of pairs of near-neighbor sites with one DEGa;
 $\omega = -10$ kJ/mole for DEGa pairs; $Z = 4$ for GaAs(100) surfaces.

References

- [2.1] E. T. FitzGerald, and J. S. Foord, *J. Cryst. Growth* **120**, 57-62 (1992).
- [2.2] A. J. Murrell, A. T. S. Wee, D. H. Fairbrother, N. K. Singh, J. S. Foord, G. J. Davies and D. A. Andrews, *J. Appl. Phys.* **68**, 4053 (1990).
- [2.3] M. E. Pemble, D. S. Buhaenko, S. M. Francis, P. A. Goulding and J. T. Allen, *J. Cryst. Growth* **107**, 37 (1991).
- [2.4] B. A. Banse and J. R. Creighton, *Surf. Sci.* **257**, 221 (1991).
- [2.5] A. Robertson Jr, T. H. Chiu, W. T. Tsang and J. E. Cunningham, *J. Appl. Phys.* **64**, 877 (1988).
- [2.6] C. L. French and J. S. Foord, *J. Cryst. Growth* **120**, 63 (1992).
- [2.7] J. S. Foord, C. L. French, C. L. Levoguer and G. J. Davies, *Phil. Trans. R. Soc. Lond. A* **344** 507 (1993).
- [2.8] S. Brunauer, *The Adsorption of Gases and Vapors*, Chapter I and IV, Princeton University Press (1945).
- [2.9] C.G. Goymour and D.A. King, *J. Chem. Soc. Faraday I* **69**, 749 (1973).
- [2.10] R. Fowler and E.A. Guggenheim, *Statistical Thermodynamics*, Section 1011, University Press, Cambridge (1952).

CHAPTER 3

A KINETIC MODEL FOR TRIS(DIMETHYLAMINO)ARSENIC DECOMPOSITION ON GaAs SURFACES

3.1 Introduction

There has been considerable interest in the development of liquid organometallic arsenic reagents as replacements for the highly toxic, gaseous arsine. In the case of metalorganic molecular beam epitaxy (MOMBE) or chemical beam epitaxy (CBE), the desirable precursors must have moderate vapor pressures and must not only lead to low-level carbon incorporation, but also decompose at low temperatures to avoid having to precrack the organometallic reagents. Tris(dimethylamino)arsenic (TDMAAs) has been synthesized as a promising alternative arsenic source for CBE as well as organometallic vapor phase epitaxy (OMVPE). This compound is distinct from other arsenic precursors by having arsenic bonded directly only to nitrogen and, thus, no carbon-arsenic bond. It also has the required moderate vapor pressure and long term stability to be of practical use in CBE and OMVPE.

TDMAAs has been shown to turn a Ga-rich GaAs(100) surface into an As-rich surface at low temperatures and low pressures (e.g., 450 °C and 2×10^{-7} Torr) without precracking [3.1]. In CBE studies by Abernathy et al. [3.2, 3.3], GaAs and AlGaAs films were grown at relatively low temperatures without precracking when using trimethylgallium (TMGa), triethylgallium (TEGa), trimethylamine alane (TMAAl) and TDMAAs. Their results showed that carbon concentrations measured by secondary ion mass spectroscopy (SIMS) analysis in GaAs layers were lower than those obtained using a similar flux of AsH₃. In addition, carbon was reduced more than two orders of magnitude in GaAs films grown with TMGa and TDMAAs as compared to TMGa and AsH₃. TDMAAs has also been utilized in atomic layer epitaxy (ALE) of GaAs and AlAs [3.4-3.6]. Dong et al. [3.7-3.10] achieved better electrical properties of GaAs grown using TEGa and TDMAAs than those of GaAs samples reported by other groups. Their laser-assisted growth of GaAs with TEGa and TDMAAs showed a wider range of growth enhancement at lower substrate temperatures.

Surface chemical kinetics as opposed to mass-transport-limited epitaxial growth can, in principal, occur in CBE and OMVPE. The surface chemistry of metalorganic

species allows us a large degree of freedom in intelligently designing the epitaxial process for a given application. It is therefore desirable to reach a detailed understanding of the fundamental surface reactions of metalorganic species, like TDMAAs, which have been shown possessing unique and superior characteristics for the epitaxy of III-V semiconductors. In addition, accurate models for the dependence of the incorporation rates of the Group III and V atoms on growth temperature, precursor fluxes and external energy settings (e.g., laser irradiation power density) can be used to determine optimum operating conditions for minimizing the sensitivity of epitaxial processes to variation in these parameters.

The purpose of this chapter is to propose a simple model of the surface chemical kinetics governing the pyrolytic decomposition of TDMAAs on GaAs(100) based on surface science investigations reported in literature [3.1, 3.11-3.16]. This model is used for research on laser-assisted growth of GaAs with TEGa and TDMAAs, which will be reported in Chapter 6. In this chapter, we will first review surface science studies on TDMAAs and proceed to present arguments on the reaction scheme and assumptions on Arrhenius parameters. We will then show results from computer modeling with the reaction mechanism.

3.2 Review of experimental Studies on TDMAAs decomposition on GaAs(100)

There have been several experimental studies of decomposition of TDMAAs on GaAs(100). Kouji et al. proposed that a monomethyl amine species (NCH_3) is the key decomposition intermediate in the dissociative adsorption of TDMAAs onto GaAs, based on transient mass spectrometry measurements during CBE and ALE [3.1, 3.11-3.12].

Salim et al. [3.13] used *in situ* mass spectroscopy at CBE conditions to show that TDMAAs thermal decomposition was completed at 450 °C, which is significantly lower than temperatures needed for complete decomposition of both tertiarybutylarsine (t-BuAsH_2) and arsine. The major products were found to be dimethylamine ($\text{HN}(\text{CH}_3)_2$), hydrogen, aziridine ($\text{HN}(\text{CH}_2)_2$) and methyldimethyleneimine ($\text{H}_2\text{C}=\text{NCH}_3$). Two decomposition pathways of TDMAAs on GaAs(100) were suggested: simple scission of arsenic and nitrogen bond of the parent followed by reaction of the dimethylaminyl radical with hydrogen to form dimethylamine; and hydrogen elimination reaction to form aziridine or methyldimethyleneimine and surface hydrogen.

Xi et al. [3.14] investigated surface decomposition of TDMAAs on GaAs(100) using low energy electron diffraction and temperature-programmed desorption (TPD) under ultra-high vacuum conditions. TDMAAs adsorbed onto GaAs(100)-(4x6) was found to decompose with 100% efficiency. Ions with $m/e=29$ (NCH_3) were observed, but the spectrum showed no additional features other than those of $m/e=42-45$. This implies that the observed NCH_3 signal can be attributed to fragmentation of $\text{H}_2\text{C}=\text{NCH}_3$ ($m/e=43$) and $\cdot\text{N}(\text{CH}_3)_2$ ($m/e=44$) desorbing from the surface. Results from coadsorption of submonolayer of deuterium atoms and TDMAAs strongly suggested that the signal of $m/e=44$ evolving at $\sim 165^\circ\text{C}$ was due to dimethylaminy radicals and that the signal of $m/e=45$ resulted from abstraction of hydrogen atoms adsorbed on the inside wall of the mass spectrometer shield. The difference in desorption intensities at 280°C between TPD spectra of $m/e=44, 45$ and that of $m/e=42, 43$ confirmed the presence of the two surface reaction pathways. In correlation with the results from studies on gas-phase pyrolysis of TDMAAs, they established that methyldimethylamine, and not aziridine, was the product of the surface β -hydrogen transfer reaction.

Xi et al. [3.15] also investigated chemisorption and decomposition of tris(dimethylamino) phosphine (TDMAP) on GaAs(100) using temperature-programmed reaction spectroscopy. The measured fragmentation pattern of TDMAP turned out to be analogous to that reported for TDMAAs. They found no evidence of the formation of monomethylamine species (NCH_3), which was proposed by Kouji et al. as a key decomposition intermediate in the dissociative adsorption of TDMAAs onto GaAs. Transferring methyl groups to the surface was not observed either. The general features of interaction of TDMAAs and TDMAP with GaAs surfaces were compared to those reported for TEGa. They concluded that the observation of two channels involving either radical formation or β -hydrogen elimination was similar to the reported reactions of group III species, specifically, TEGa.

In their studies of TDMAAs decomposition on a clean GaAs(100) substrate in a CBE reactor using modulated beam mass spectrometry (MBMS), Whitaker et al. [3.16] found that the major signals were $m/e=42, 44$ and those of fragmentation products of the parent molecule. They also found a significant variation with the substrate temperature of the signal corresponding to As atoms from decomposition of TDMAAs. The As signal peaked around 500°C . In addition, their studies indicated a change in

decomposition behavior above ~ 480 °C with an increase in the desorption of high mass As-containing species (mainly $\text{AsN}(\text{CH}_3)_2$).

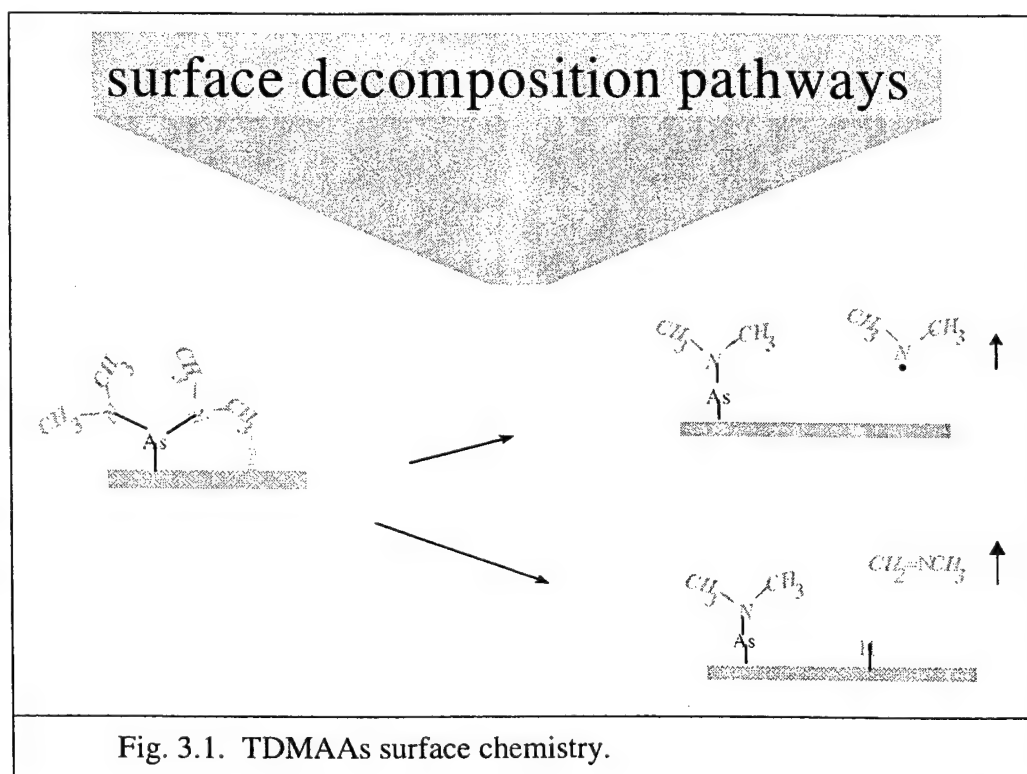
3.3 Reaction Mechanism and Assumptions on Arrhenius Parameters

The reactions chosen by us to describe TDMAAs decomposition on the GaAs(100) surface are listed as reactions (1) to (9) in Table 1. The decomposition pathways are illustrated in Fig. 3.1. A ligand of a TDMAAs molecule is removed either through a direct bond scission or a β -hydrogen surface transfer reaction

Table 3.1. Reaction Scheme for TDMAAs decomposition		
	$A(\text{s}^{-1})$	E (kJ/mol)
(1) $\text{As}(\text{N}(\text{CH}_3)_2)_3 (\text{g}) + \text{e.s.} \longrightarrow \text{As}(\text{N}(\text{CH}_3)_2)_3 (\text{ads})$	(a)	0
(2) $\text{As}(\text{N}(\text{CH}_3)_2)_3 (\text{ads}) \longrightarrow \text{As}(\text{N}(\text{CH}_3)_2)_2 (\text{ads}) + \cdot\text{N}(\text{CH}_3)_2 (\text{g})$	6×10^{13}	120
(3) $\text{As}(\text{N}(\text{CH}_3)_2)_2 (\text{ads}) \longrightarrow \text{AsN}(\text{CH}_3)_2 (\text{ads}) + \cdot\text{N}(\text{CH}_3)_2 (\text{g})$	9×10^{11}	120
(4) $\text{AsN}(\text{CH}_3)_2 (\text{ads}) \longrightarrow \text{As}(\text{ads}) + \cdot\text{N}(\text{CH}_3)_2 (\text{g})$	7×10^9	120
(5) $\text{As}(\text{N}(\text{CH}_3)_2)_3 (\text{ads}) + \text{e.s.} \longrightarrow \text{As}(\text{N}(\text{CH}_3)_2)_2 (\text{ads}) + \text{H} (\text{ads}) + \text{H}_2\text{C}=\text{NCH}_3 (\text{g})$	(b)	
(6) $\text{As}(\text{N}(\text{CH}_3)_2)_2 (\text{ads}) + \text{e.s.} \longrightarrow \text{AsN}(\text{CH}_3)_2 (\text{ads}) + \text{H} (\text{ads}) + \text{H}_2\text{C}=\text{NCH}_3 (\text{g})$	6×10^{14}	120
(7) $\text{AsN}(\text{CH}_3)_2 (\text{ads}) + \text{e.s.} \longrightarrow \text{As} (\text{ads}) + \text{H} (\text{ads}) + \text{H}_2\text{C}=\text{NCH}_3 (\text{g})$	2×10^{10}	120
(8) $\text{As} (\text{ads}) + \text{As} (\text{ads}) \longrightarrow \text{As}_2 (\text{g}) + 2 \text{e.s.}$	1×10^{11}	125
(9) $\text{H} (\text{ads}) + \text{H} (\text{ads}) \longrightarrow \text{H}_2 (\text{g}) + 2 \text{e.s.}$	1×10^{13}	126
e.s., an empty site (ads), adsorbed species (g), gas-phase species (a), Langmuir adsorption kinetics (b), relatively negligible		

Reaction (1) is for TDMAAs chemisorption. TDMAAs molecules adsorbed at a submonolayer coverage are assumed to decompose irreversibly. This assumption is based on observations in TPD studies of TDMAAs decomposition [3.14], but we need to be cautious when invoking this assumption (see the discussion section below). Reactions (2) to (4) are for simple scission of the arsenic-nitrogen bond similar to those proposed for gas-phase pyrolysis of TDMAAs [3.14]. Dimethylamino radicals are assumed to be ejected into the gas-phase directly. We should note that it is possible that dimethylamino

ligands are first transferred to the surface. These ligands, however, may be very weakly bound to the surface so that they start desorbing immediately from the surface at a low enough temperature before reactions between themselves and reactions (5) to (9) kick in, since Xi et al. [3.15] showed that the possibility could be eliminated of $(\text{CH}_3)_2\text{NH}$ being formed by recombination with surface H atoms and by H atom transfer between dimethylamino ligands. The breaking-away of these ligands from the parent may produce the surface sites necessary for initial onset of reactions (5) to (7). The overall process of scission of the arsenic-nitrogen bond and desorption of dimethylamino radicals can thus be represented by reactions (1) to (4). Reactions (5) to (7) are for hydrogen transfer reactions forming methyldimethylamine $\text{CH}_3\text{N}=\text{CH}_2$. These reactions increase the number of surface species and are thus assumed to require the presence of adjacent vacant surface sites.



For a large molecule such as TDMAAs at thermal energies it is reasonable to assume that the trapping probability at zero coverage is unity, independent of temperature. Adsorption of TDMAAs is computed by using Langmuir adsorption kinetics with a clean surface sticking probability of unity. Precursor-mediated adsorption

which may be important at low temperatures (< 600 K) [3.17] is not taken into account in our model. The effect of this assumption on the kinetic parameters we establish for this model will be discussed with consideration of the uncertainties in experimental data based on which we derive the parameters. The rate constant of each of reactions (2) to (9) is modeled by the Arrhenius expression, $A\exp(-E/RT)$, with A being the pre-exponential factor and E the activation energy for the reaction. We used the method of fitting to determine the kinetic parameters in Table 3.1. The most important criterion used in the determination of the kinetic parameters for TDMAAs decomposition was that they simulate satisfactorily the mass spectroscopy data of Xi et al. [3.14]. We assume that the pre-exponential factors for reactions (2) to (4) satisfy $A_2 > A_3 > A_4$. This assumption was made partially because of consideration of the bulkiness of $\text{As}(\text{N}(\text{CH}_3)_2)_3$, $\text{As}(\text{N}(\text{CH}_3)_2)_2$ and $\text{AsN}(\text{CH}_3)_2$, and partially because the experimental data can be reproduced satisfactorily with this assumption. Also we assume that the pre-exponential factors for reactions (5) to (7) satisfy that A_5 is negligible and $A_6 \gg A_7$. These assumptions are analogous to the constraints imposed by Donnelly and Robertson [3.17] for TEGa decomposition scheme on GaAs(100). A_5 being negligible implies that the dominant process for the parent molecule is scission of As and N bond after its impingement onto the surface. In the trial process to achieve fitting, it turned out that these assumptions are necessary to reproduce satisfactorily the desorption features observed in the surface science studies done by Xi et al. [3.14]. With all the above assumptions, removal of the last dimethylamino ligand is essentially the rate limiting step of the overall decomposition of TDMAAs.

The activation energy for reaction (6) is assumed to be equal to that for reaction (7). This assumption is the same as that determined by Donnelly and Robertson [3.17] for $\text{Ga}(\text{C}_2\text{H}_5)_2(\text{ads})$ and $\text{GaC}_2\text{H}_5(\text{ads})$ dissociation in the process of TEGa decomposition on GaAs(100). The activation energies for reactions (2) to (4) are assumed to be identical to those for reactions (6) and (7). An equivalent assumption is that the two reaction pathways are resulted from the same transition-state complex formed due to the interaction of TDMAAs with the surface. This assumption stems mainly from the experimental fact that dimethylaminyl radicals and methylmethyleimine desorb at approximately the same temperature and have the same desorption temperature peaks (165 °C and 280 °C). The As-N bond strength in a TDMAAs molecule was estimated to be 43.5 Kcal/mole [3.15, 3.18]. In theory, the bond energy of the last dimethylamino radical (DMA) in gas-phase pyrolysis of $\text{As}(\text{N}(\text{CH}_3)_2)_3$ is larger than the previous DMA-arsenic bond energies [3.19]. As we discussed above, however, reactions (2)-(4) are

likely to be surface mediated with a desorption of the dimethylamino radical, and it can be reasonable to assume that they are of the same activation energy.

An ordinary differential equation set is constructed for the reaction system listed in Table 3.1:

$$\frac{dC_i}{dt} = \sum_{j=1}^9 \nu_{ji} k_j \prod_l C_{jl} \quad (3.1)$$

where C_i is the surface coverage, ν_{ji} the stoichiometric coefficient of species i in reaction j , k_j the reaction constant of reaction j and C_{jl} the surface coverage of reactant l of reaction j . The equation set is solved numerically with the Gear's method for stiff problems [3.20]. A steady state of the system is determined to be reached when the magnitude of dC_i/dt is much less than those of terms on the right hand side of Equation (3.1). The kinetic parameters for hydrogen recombination reaction and arsenic recombination reaction are taken from Foord et al.'s paper [3.21]. In deriving the remaining six kinetic parameters, we required that the constraints we assumed above be satisfied and focused on reproducing the TPD characteristic temperatures of TDMAAs decomposition (see discussion on Fig. 3.2 in the following section) and relative magnitudes of the TPD desorption peaks of TDMAAs decomposition [3.14]. The Arrhenius parameters we determined are shown in Table 3.1. The values of the parameters are within a reasonable range for surface pyrolysis and adsorption-desorption phenomena.

3.4 Modeling results

Using a quadrupole mass spectrometer (QMS), Xi et al. [3.14] followed ions of desorption products corresponding to $m/e=42$ ($H_2C=NCH_2\cdot$), 43 ($H_2C=NCH_3$), 44 ($\cdot N(CH_3)_2$) and 45 ($HN(CH_3)_2$) after an 8-Langmuir dose of TDMAAs onto GaAs(100). Salim et al.'s decomposition study [3.13] was performed by dosing TDMAAs until the pressure of an ultra-high-vacuum chamber reached 10^{-5} Torr and then collecting QMS mass spectra in 50 °C temperature increments from 50 to 650 °C. The desorption behavior of either $As(N(CH_3)_2)_2$ or $AsN(CH_3)_3$ was used to represent that of the parent. $m/e=44$, 45 can result only from a dimethylamine molecule or a dimethylaminyl radical, whereas $m/e=42$, 43 can derive either from fragmentation of

dimethylamine/dimethylamino radicals or from methylmethyleimine. However, the data of relative ion intensities of dimethylamine show that approximately 15% of dimethylamine molecules are detected as $m/e=42$ and 43 signals [3.15, 3.22]. In our analysis we therefore assume that the summation of $m/e=42$ and 43 signals in Xi et al.'s TPD experiment resulted almost exclusively from the flux of methylmethyleimine desorbing from the GaAs(100) surface.

Given a chamber pressure P , the flux of TDMAAs onto a GaAs surface is calculated from

$$\text{TDMAAs Flux} = \frac{P}{\sqrt{2\pi kmT}} \quad (3.2)$$

where T is the chamber temperature, m the molecular mass and k the Boltzman constant. When comparing the predicted thermal desorption spectra to QMS experimental data, we only intended to achieve a good qualitative agreement for the following reasons. Transmissions of quadruple filters are known to be sometimes mass-dependent [3.15]. The cracking pattern of a species is known to be temperature dependent [3.17]. Also because of these reasons, we did not attempt to incorporate into our model a formulation for the possible precursor-mediated adsorption of TDMAAs by introducing additional unknown parameters.

Fig. 3.2 gives the predicted temperature programmed desorption of the dimethylamino radical (dashed line) and $\text{H}_2\text{C}=\text{NCH}_3$ (solid line). The spectra of $\text{H}_2\text{C}=\text{NCH}_3$ show two desorption peaks at 165 °C and 280 °C, while the latter is a less developed shoulder in the spectra of dimethylamino radicals. Dimethylamino radicals evolve at a relatively higher rate than $\text{H}_2\text{C}=\text{NCH}_3$ below 155 °C, whereas the reverse behavior holds above 155 °C. All these features simulated by our model are in a very good agreement with results from Xi et al.'s TPD studies [3.14]. A schematic plot of their TPD data is in Fig. 3.3.

Fig. 3.4 shows relative desorption fluxes of TDMAAs decomposition products as a function of temperature with the surface reaction system being at steady state at each temperature. The plateau, which begins at 450 °C, demonstrates that the thermal decomposition of TDMAAs is complete at temperatures as low as 450 °C. TDMAAs starts to decompose significantly at $T=300$ °C. Whitaker et al. [3.16] also found in their MBMS studies that the onset of decomposition occurred at 300 °C. Also displayed on

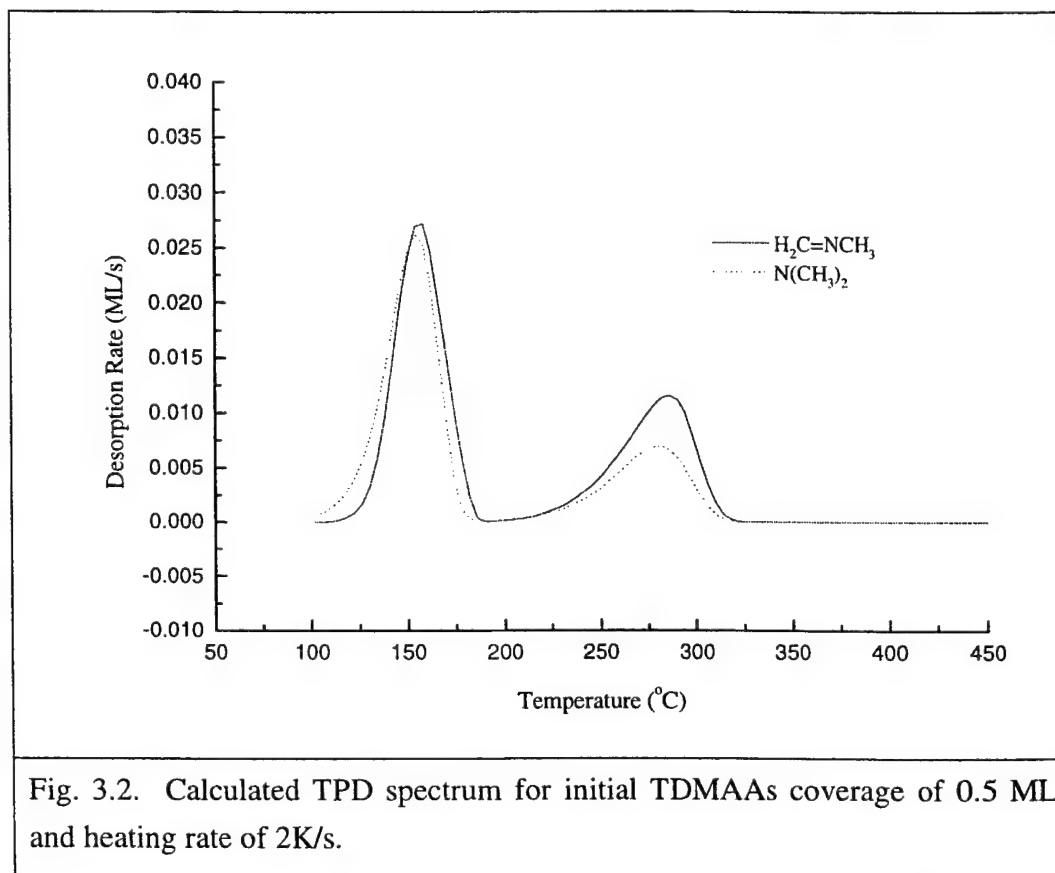
Fig. 3.4 are the experiment data reported by Salim et al. [3.13]. The overall features of results from their experiment are reproduced reasonably well in Fig. 3.4. Desorption fluxes from the first adsorption layer of TDMAs are simulated in this model. At lower temperatures, multilayer physisorption of TDMAs occurs. The discrepancies at lower temperatures between simulation and experimental data are likely due to contribution of multilayers of physisorbed TDMAs formed on the substrate when the chamber was filled with TDMAs prior to heating up the substrate. The fact that the agreement between simulation and experiment becomes better at higher temperatures indicates that at high temperatures, only the physical and chemical processes in the first adsorption layer are needed to be considered. 50% conversion was achieved at 350 °C in their experiment. This is in agreement with our simulation results. Our modeling, however, indicates that the temperature for 50% conversion is somewhat sensitive to the chamber pressure. In Fig. 3.4 the TDMAs chamber pressure is 4×10^{-6} Torr. The mean free path of a TDMAs molecule in the gas phase can be estimated from the following formula,

$$\lambda = \frac{1}{\sqrt{2}\pi\sigma^2N} \quad 3)$$

where N is the number of molecules per unit volume and σ the diameter of the molecule. With $T=300$ K, $P=10^{-5}$ Torr and $\sigma \sim 10$ Å, λ is calculated to be 700 mm. The quadrupole mass spectrometer and dosers in Salim et al.'s experiment were mounted 40 mm and 50 mm away respectively in front of the substrate. It is therefore very likely that velocities of TDMAs molecules adjacent to the substrate were not in an equilibrium distribution as assumed in Equation 2). Over the plateau of the curve for TDMAs desorption which begins at 450 °C, one would expect that the flux of total nitrogen atoms leaving the substrate is independent of temperature. Yet the results presented by Salim et al. did not follow this expectation. It is known that at temperatures higher than 400 °C, the gas-phase dimethylaminy radical decomposes to form a methyl radical and methyleneimine [3.23]. The decrease of dimethylamine yields starting at 400 °C, as reported by them, indicates possible decomposition of the dimethylaminy radical en route to the QMS ion detector.

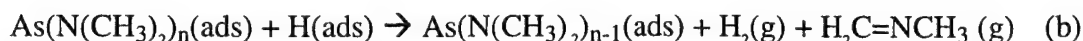
Figs. 3.5 and 3.6 show calculated surface coverages corresponding to experimental conditions of Figs. 3.1 and 3.3, respectively. As we can see from Figs. 3.2 and 3.5, the peak of $H_2C=NCH_3$ desorption at 280 °C corresponds to a low H coverage on the surface. This result can be explained in terms of hydrogen recombination controlling available sites for β -hydrogen elimination reactions (5)-(7). All H_2 atoms

desorbing from the surface result from recombination of hydrogen atoms transferred to the surface. Therefore we can see from Fig. 3.4 that each TDMAAs parent molecule can contribute approximately two surface hydrogen atoms at high temperatures. The steady-state hydrogen coverage is small, as shown in Fig. 3.6. It may seem in appearance that since adsorbed hydrogen atoms once formed from β -hydrogen transfer reactions quickly recombine and leave the surface, adsorbed hydrogen atoms do not play a role in controlling crystal growth and crystal electrical properties. But if there are other surface hydrogen removal processes competing with the recombination reaction, such as methane or ethane formation, the significance of TDMAAs on GaAs(100) surfaces as a hydrogen atom provider will certainly distinguish itself from other As precursors.



3.5 Discussion

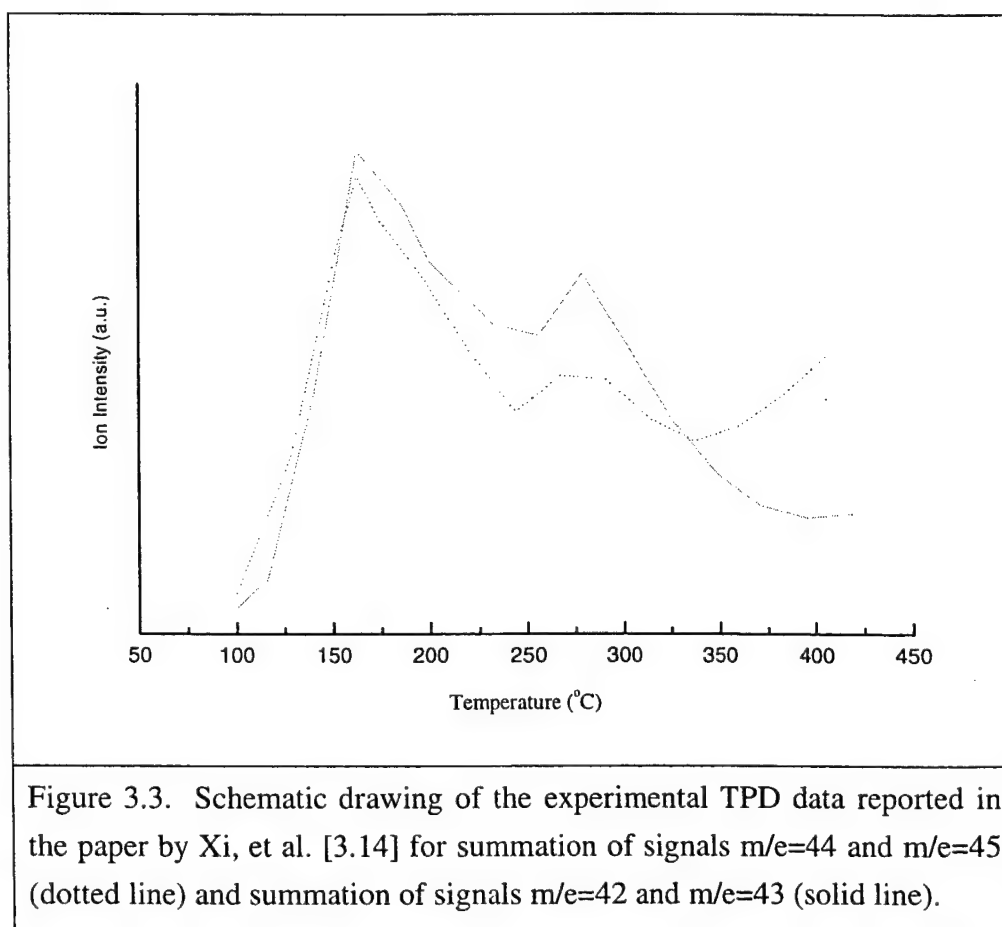
In light of gas-phase pyrolysis pathways of TDMAs [3.23] and consideration of species most likely chemisorbed on the GaAs(100) surface, one may be compelled to consider the importance of the following two surface reaction pathways.



Xi et al. [3.14] did not observe a large increase in $(\text{CH}_3)_2\text{ND}$ formation in their D atom co-adsorption experiment on the GaAs surface. Reaction (a) is therefore not important as a reaction involving hydrogen addition from the surface would be affected by the presence of D atoms on the surface. Likewise, we can safely neglect reaction (b) because the amount of $\text{H}_2\text{C}=\text{NCH}_3$ formed in their co-adsorption experiment actually decreased in comparison to that from after the same TDMAs exposure, but without D atom coadsorption. The same conclusion may also be drawn from the modeling results in Fig. 3.4, since the importance of reaction (b) might have led to a desorption peak of $\text{H}_2\text{C}=\text{NCH}_3(\text{g})$ at around 200 °C, in correspondence to high H and surface $\text{AsN}(\text{CH}_3)_2$ coverages.

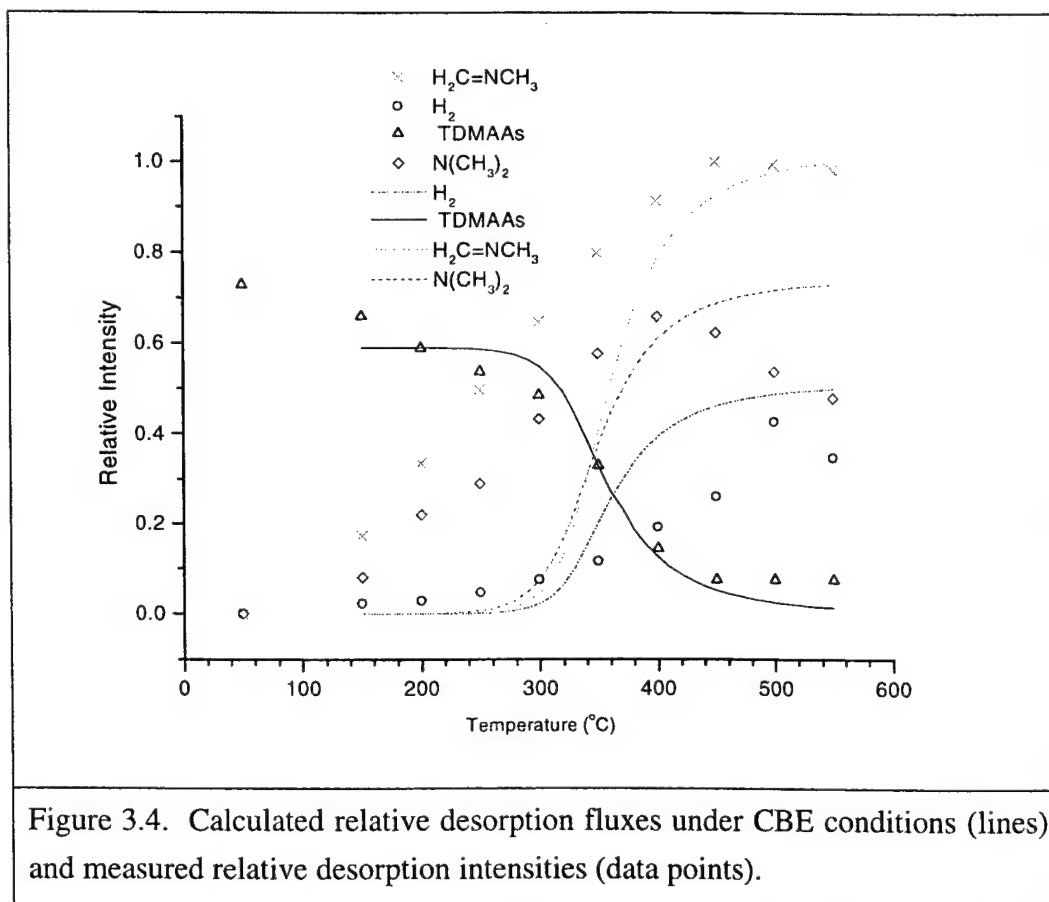
The dosing of TDMAs in Xi et al.'s TPD study cited in this paper was carried out at a temperature much lower than typical CBE growth temperatures. In our model, TDMAs molecules adsorbed at a submonolayer coverage are assumed to decompose irreversibly in accordance to their experimental observation. We would like to point out, however, that we cannot rule out for certain the possibility that a noticeable fraction of TDMAs molecules impinging on GaAs surfaces at high growth temperatures may go through the desorption pathway, as opposed to the dissociation reaction pathway. Similarly, it is also possible that reaction pathways other than those in Table 3.1 for adsorbed TDMAs and intermediate species may be important at high growth temperatures. Since the surface coverage is expected to be small at high growth temperatures under typical CBE conditions, we may nevertheless still be able to safely neglect those reactions which involve two adsorbed species but not constituent atoms of the substrate.

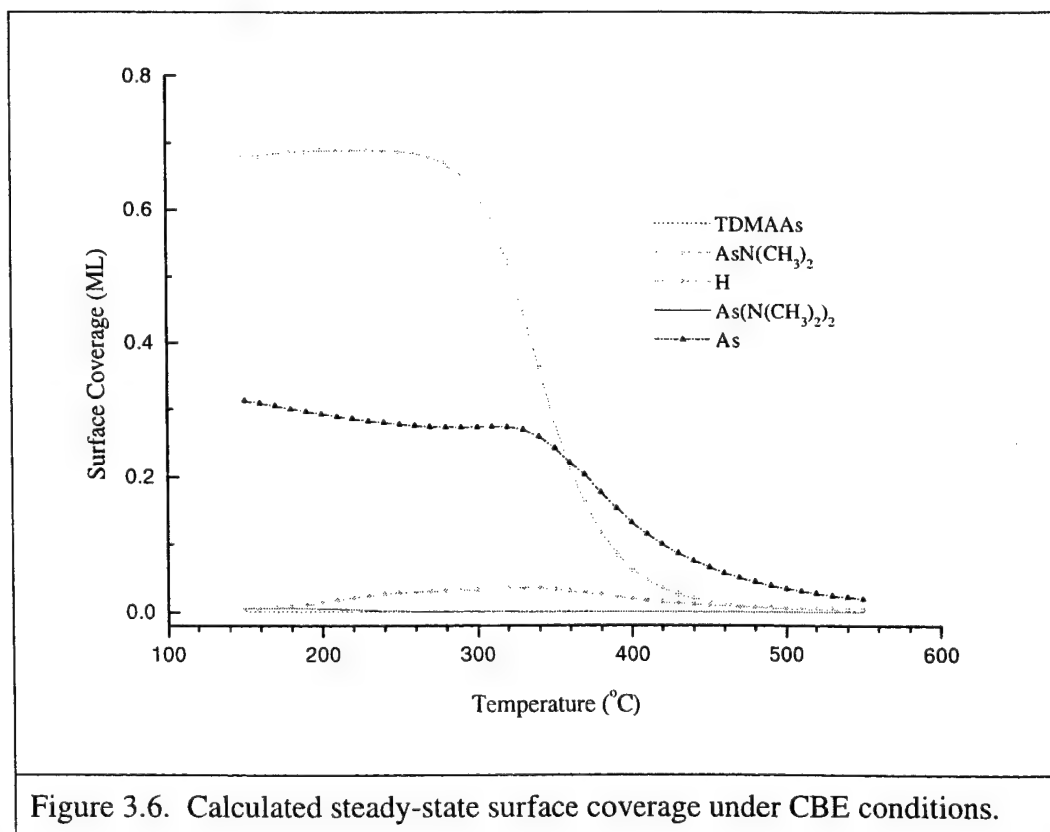
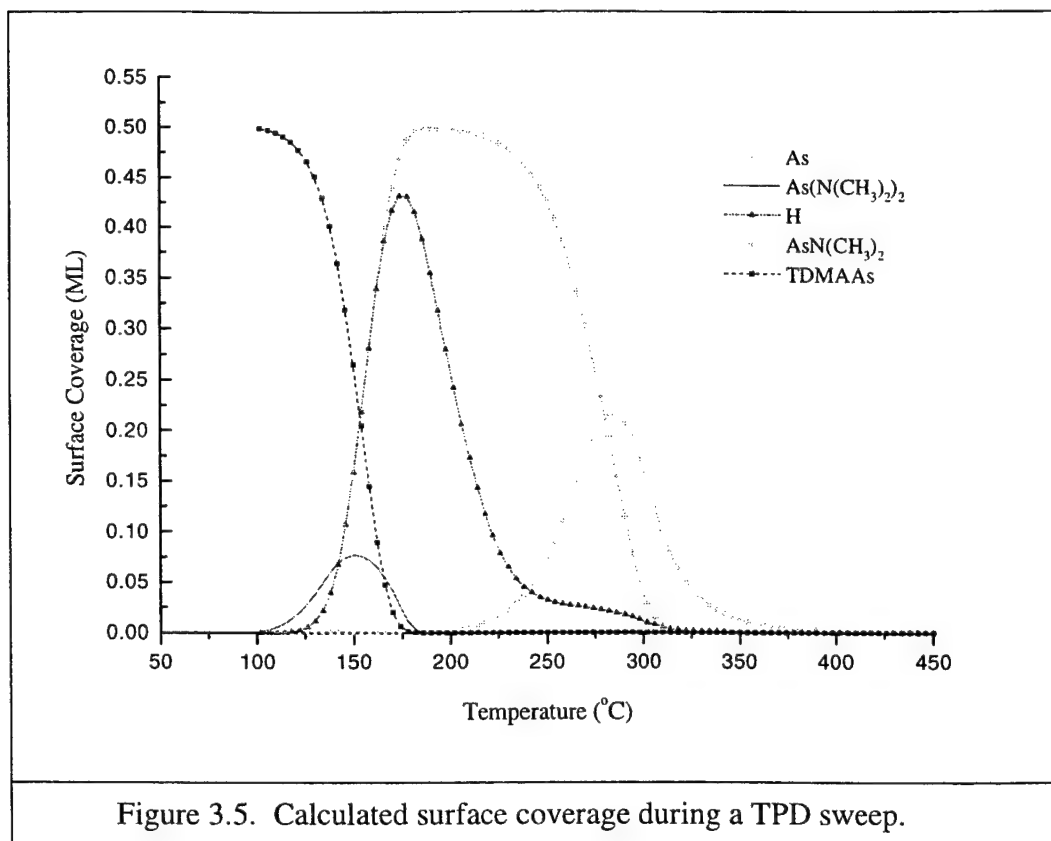
In surface science studies, the quadrupole mass spectrometer is usually mounted right in front of a substrate surface to measure desorption fluxes from the surface. Even though the total gas pressure inside the QMS shield may be very low, at high substrate temperatures we may have to take into account gas-phase reactions inside the shield when calculating desorption fluxes. This is because rates of reactions between thermally activated species from the substrate can be much larger at high substrate temperatures. When interpreting the As signal variation with the substrate temperature recorded in Whitaker et al.'s studies [3.16], it is possible that we need to consider both the fragmentation pattern of TDMAAs and gas-phase reactions in the QMS shield which might be important at high substrate temperatures.



3.6 Conclusion

The detailed arguments involved in developing a kinetic model describing surface pyrolysis of tris(dimethylamino) arsine on GaAs(100) surfaces have been outlined. Two decomposition pathways of TDMAAs on GaAs(100) are explicitly taken into account: simple scission of the arsenic and nitrogen bond and surface β -hydrogen transfer reaction. The activation energies for the two reaction pathways are assumed to be the same based on TPD measurement. An equivalent assumption is that the two reaction pathways resulted from the same transition-state complex formed due to the interaction of TDMAAs with the surface. The dominant process for the parent molecule is assumed to be scission of As and N bond after its impingement onto the surface. Removal of the last dimethylamino ligand is assumed to be essentially the rate-limiting step of the overall decomposition of TDMAAs. The chemical kinetic parameters have been derived based on TPD data reported in literature. We have demonstrated that the model can reproduce well the behavior of desorption data from surface science studies of TDMAAs thermal decomposition on GaAs(100) surfaces.





References

- [3.1] K. Hamaoka, I. Suemune, K. Fujii, T. Kouji, A. Kishimoto and M. Yamanishi, Japan J. Appl. Phys. 30, L1579 (1991).
- [3.2] C. R. Abernathy, P. W. Wisk, S. J. Pearton, F. Ren, D. A. Bohling and G. T. Muhr, J. Crystal Growth 124, 64 (1992).
- [3.3] C. R. Abernathy, P. W. Wisk, D. A. Bohling and G. T. Muhr, Appl. Phys. Lett. 60, 2421 (1992).
- [3.4] K. Fujii, and I. Suemune, Appl. Phys. Lett. 60, 1498 (1992).
- [3.5] K. Fujii and I. Suemune, Appl. Phys. Lett. 61, 2577 (1992).
- [3.6] K. Fujii and I. Suemune, Appl. Phys. Lett. 62, 1420 (1993).
- [3.7] H. K. Dong, N. Y. Li and C. W. Tu, J. Electronic Materials 24, 69 (1995).
- [3.8] N. Y. Li, H. K. Dong, W. S. Wong and C. W. Tu, Vol. 164, J. Crystal Growth 164, 112 (1996).
- [3.9] C. W. Tu, H. K. Dong and N. Y. Li, Materials Chemistry and Physics 40, 260 (1995).
- [3.10] H. K. Dong, Ph. D Thesis, (University of California at San Diego, La Jolla, California, 1995).
- [3.11] T. Kouji, I. Suemune, K. Miyakoshi, K. Fujii and M. Yamanishi, Jpn. J. Appl. Phys. 31, L1272 (1992).
- [3.12] T. Kouji, et al. in Extended Abstracts of the 1991 International Conference on Solid State Devices and Materials, (Yokohama, Japan, 1991).
- [3.13] S. Salim, J. P. Lu, K. F. Jensen, J. Crystal Growth 124, 16 (1992).
- [3.14] M. Xi, S. Salim, K. F. Jensen and D. A. Bohling, Mat. Res. Soc. Symp. Proc. 334, 169 (1994).
- [3.15] M. Xi and K. F. Jensen, Surface Science 339, 310 (1995).
- [3.16] T. J. Whitaker, T. Martin, A. D. Johnson, A. J. Pidduck and J. P. Newey, J. Crystal Growth 164, 125 (1996).
- [3.17] V. M. Donnelly and A. Robertson, Jr., Surface Science 293, 93 (1993).
- [3.18] C. A. Larsen, N. I. Buchan, S. H. Li and G. B. Stringfellow, J. Crystal Growth 94, 663 (1989).
- [3.19] M. G. Jacko and S. W. Price, Can. J. Chem. 41, 1560 (1963).
- [3.20] C. W. Gear, Numerical Initial Value Problems in Ordinary Differential Equations, (Prentice-Hall, Englewood Cliffs, N. J., 1971).
- [3.21] J. S. Foord, C. L. French, C. L. Levoguer and G. J. Davies, Phil. Trans. R. Soc. Lond. A 344, 507 (1993).

[3.22] S. R. Heller and G. W. Milne, EPA/NIH Mass Spectral Data Base.

[3.23] S. Salim and K.F. Jensen, Chemistry of Materials 7, 507 (1995).

CHAPTER 4

A REACTION MODEL FOR CHEMICAL BEAM EPITAXY WITH TRIETHYLGALLIUM AND TRIS(DIMETHYLAMINO)ARSENIC

4.1 Introduction

Surface chemical-kinetics-limited as opposed to mass-transport-limited epitaxial growth of semiconductors can, in principal, occur in epitaxy of semiconductors involving metalorganic species. The surface chemistry of metalorganic species allows a large degree of freedom in intelligently designing the epitaxial process for a given application. It is therefore desirable to reach a detailed understanding of the fundamental surface reactions of metalorganic species. In addition, accurate models for the dependence of the incorporation rates of constituent atoms and dopant atoms on growth temperature, precursor fluxes and external energy settings (e.g., laser irradiation power density) can be used to determine optimum operating conditions for minimizing the sensitivity of epitaxial processes to variation in these parameters.

The mechanism of GaAs growth on GaAs(100) surfaces using the ultra-high vacuum (UHV) technique of metalorganic molecular beam epitaxy (MOMBE) with solid arsenic and triethylgallium (TEGa) has been extensively investigated in recent years. Robertson et al. [4.1] proposed a stepwise mechanism for TEGa decomposition on GaAs(100), estimated the relative magnitudes of the kinetic parameters, and fitted these parameters to observed GaAs growth rates. The data for the incident flux in monolayer per second (ML/s) corresponding to one mass flow controller (MFC) setting was obtained by including the flux as a fitting parameter along with the kinetic parameters. The incident fluxes at other flow rates were then derived by scaling, as was done experimentally. Donnelly and Robertson [4.2] extended Robertson's previous model by including new reactions and Arrhenius parameters reported in UHV studies. Liang and Tu [4.3] developed an analytical model for MOMBE growth of GaAs by assuming that surface As_2 could enhance the rate of both TEGa desorption and surface dimethylgallium

(DEGa) decomposition. Foord et al. [4.4-4.6] developed a numerical model of GaAs MOMBE growth with TEGa and As₂ on GaAs(100) surfaces.

In this chapter, a reaction model of chemical beam epitaxy of GaAs with TEGa and tris(dimethylamino)arsenic (TDMAs) on GaAs(100) will be reported. TDMAs is believed to be a promising, less toxic alternative to the toxic, gaseous arsine [4.7]. Epitaxy of III-V semiconductors with TDMAs has shown that it possesses unique and superior characteristics for lowering background carbon incorporation, improving electrical properties of semiconductors and *in situ* etching [4.8-4.9]. In this chapter, the practice is also developed of inputting growth data obtained experimentally from the group-V induced intensity oscillations of reflection high-energy electron diffraction (RHEED) as group-V ML/s incident fluxes needed in III-V semiconductor growth models. The decomposition mechanisms of TEGa and TDMAs implemented in this GaAs growth model are described in Chapters 2 and 3. The reactions of the mechanisms are renumbered in Table 4.1 for discussion of this chapter.

4. 2 Reaction schemes for TEGa and TDMAs interactions on GaAs surfaces

Co-dosing experiments carried out by Salim et al. [4.13] with TDMAs and trimethylgallium or deuterium-labeled trimethylgallium (Ga(CD₃)₃) revealed that methane and methylarsenic were major reaction products in addition to the nitrogen-containing species, methylmethyleimine (H₂C=NCH₃) and dimethylamine (HN(CH₃)₂). By analogy with their findings, there should be formation of ethane and ethylarsenic in the case of growth with TEGa and TDMAs. Since the recombination reaction of an ethyl radical with a hydrogen atom is included in the TEGa decomposition model, the effect of TDMAs as a hydrogen atom provider on GaAs growth is thus explicitly taken into account with the TDMAs decomposition model developed in Chapter 3. Evidence of desorption of ethyl-arsenic radicals was found using mass spectroscopy during GaAs growth with TEGa [4.14], but these species were present in concentrations several orders of magnitude lower than ethylene. Therefore, reactions between adsorbed arsenic atoms and ethyl radicals are ignored in this growth model. In a later report by Xi et al. [4.12], it

was concluded that dimethylamine radicals ($\cdot\text{N}(\text{CH}_3)_2$), instead of dimethylamine molecules, were the products evolving from GaAs(100) surfaces dosed with TDMAs and dimethylamine-molecule formation was due to involvement of hydrogen atoms adsorbed on the inside wall of their mass spectrometer. Thus, no reaction producing the molecules is assumed in this growth model.

Table 4.1

Reaction Scheme For TEGa decomposition

	$A(\text{s}^{-1})$	E (kJ/mol)
(1) TEGa (g) + e.s. \longrightarrow TEGa (ads)	(a)	0
(-1) TEGa (ads) \longrightarrow TEGa (g) + e.s.	10^{11}	50
(2) TEGa (ads) + e.s. \longrightarrow DEGa (ads) + C_2H_5 (ads)	10^{14}	55
(-2) DEGa (ads) + C_2H_5 (ads) \longrightarrow TEGa (ads) + e.s.	10^{11}	105
(3) DEGa (ads) \longrightarrow DEGa (g) + e.s.	10^{14}	165
(4) DEGa (ads) + e.s. \longrightarrow Ga + 2 C_2H_5 (ads)	10^{12}	135
(5) C_2H_5 (ads) \longrightarrow C_2H_5 (g) + H (ads)	10^{12}	147
(6) C_2H_5 (ads) + H (ads) \longrightarrow C_2H_6 (g) + 2 e.s.	10^{14}	165
(7) H(ads) + H(ads) \longrightarrow H_2 (g) + 2 e.s.	10^{13}	126

e.s., an empty site

(ads), adsorbed species

(g), gas-phase species

(a), Langmuir adsorption kinetics

Reaction Scheme for TDMAs decomposition

	$A(\text{s}^{-1})$	E (kJ/mol)
(8) $\text{As}(\text{N}(\text{CH}_3)_2)_3$ (g) + e.s. \longrightarrow $\text{As}(\text{N}(\text{CH}_3)_2)_3$ (ads)	(a)	0
(9) $\text{As}(\text{N}(\text{CH}_3)_2)_3$ (ads) \longrightarrow $\text{As}(\text{N}(\text{CH}_3)_2)_2$ (ads) + $\cdot\text{N}(\text{CH}_3)_2$ (g)	6×10^{13}	120
(10) $\text{As}(\text{N}(\text{CH}_3)_2)_2$ (ads) \longrightarrow $\text{AsN}(\text{CH}_3)_2$ (ads) + $\cdot\text{N}(\text{CH}_3)_2$ (g)	9×10^{11}	120
(11) $\text{AsN}(\text{CH}_3)_2$ (ads) \longrightarrow As(ads) + $\cdot\text{N}(\text{CH}_3)_2$ (g)	7×10^9	120
(12) $\text{As}(\text{N}(\text{CH}_3)_2)_3$ (ads) + e.s. \longrightarrow $\text{As}(\text{N}(\text{CH}_3)_2)_2$ (ads) + H (ads) + $\text{H}_2\text{C}=\text{NCH}_3$ (g)	(b)	
(13) $\text{As}(\text{N}(\text{CH}_3)_2)_2$ (ads) + e.s. \longrightarrow $\text{AsN}(\text{CH}_3)_2$ (ads) + H (ads) + $\text{H}_2\text{C}=\text{NCH}_3$ (g)	6×10^{14}	120
(14) $\text{AsN}(\text{CH}_3)_2$ (ads) + e.s. \longrightarrow As (ads) + H (ads) + $\text{H}_2\text{C}=\text{NCH}_3$ (g)	2×10^{10}	120
(15) As (ads) + As (ads) \longrightarrow As_2 (g) + 2 e.s.	1×10^{11}	125
(16) H (ads) + H (ads) \longrightarrow H_2 (g) + 2 e.s.	1×10^{13}	126

(b), relatively negligible

Prior to Salim et al.'s work [4.13], it had been hypothesized [4.15] that CBE GaAs growth with TMGa and TDMAAs involves a simple transfer of methyl from TMGa to the dimethylamine, leading to the formation of the stable compound, trimethylamine ($\text{HN}(\text{CH}_3)_3$). But no trimethylamine was detected as a surface reaction product in Salim et al.'s experimental investigation [4.13]. Based on Salim et al.'s finding we propose that interactions between dimethylamino ligands of TDMAAs and TEGa or its decomposition products including ethyl radicals are not important.

The GaAs growth rate is equated to the rate at which adsorbed TEGa species become converted to surface Ga. It is also assumed in our model that with every Ga atom incorporated into the lattice of a substrate, an adsorbed arsenic atom is also incorporated into the lattice, yielding an empty surface site. In addition to the role of TDMAAs species as a provider of surface hydrogen atoms, TDMAAs and its decomposition products affect the growth rates also by occupying surface sites and therefore inhibiting TEGa adsorption and decomposition processes. TDMAAs decomposition is also dependent on the growth rate since Ga incorporation into the lattice depletes adsorbed arsenic atoms and TDMAAs surface decomposition critically depends on the number of surface sites available.

4.3. Simulation, experiment and comparison

An ordinary differential equation set is constructed for the reaction systems listed in Table 4.1:

$$\frac{d\theta_i}{dt} = \sum_{j=1} v_{ji}(\text{rate})_j \quad (4.1)$$

where θ_i is the surface coverage (ML) of species i , v_{ji} the stoichiometric coefficient of species i in reaction j and $(\text{rate})_j$ the reaction rate of reaction j of Table 4.1. Formulation of the reaction rates is described in previous chapters. The equation set is solved numerically with the Gear's method for stiff problems [4.16]. A steady state of the

system is determined to be reached when the magnitude of $d\theta_i/dt$ is much less than those of terms on the right-hand side of Equation (4.1).

Experimental growth rates were measured by means of *in situ* RHEED intensity oscillations. In our experiment, TEGa is introduced into the growth chamber through a vapor source mass flow controller, while TDMAAs is carried by hydrogen and injected into the chamber through a leak valve. Since the relationship between the TDMAAs flow rate and the flow rate of hydrogen carrier gas involves nonlinear fluid dynamics, we determine the absolute incident flux of TDMAAs using the RHEED oscillations of group V-induced growth, i.e., RHEED intensity oscillations induced by a group V-injection onto a Ga-rich substrate resulted from deposition of several monolayers of TEGa [4.17]. Fig. 4.1 shows group V-induced growth rate as a function of substrate temperature, while the insert a typical example of group V-induced RHEED oscillations. The practice of equating the group V-induced growth rate to the TDMAAs flux in ML/s can be valid under three conditions. They are 1) every TDMAAs molecule impinging on a Ga-rich surface decomposes and contributes an adsorbed As atom on the surface, 2) all adsorbed As atoms are incorporated into the lattice of the substrate, and 3) As_2 desorption from the GaAs lattice is negligible.

It is well known that the As sticking coefficient is unity on a Ga-rich surface [4.18]. It is reasonable to assume that all As atoms resulted from decomposition of TDMAAs on a Ga-rich surface are incorporated into the lattice. As_2 desorption from the GaAs lattice would be expected to occur only at high substrate temperatures. Therefore, we can assume that on a Ga-rich surface, conditions 2) and 3) listed in the last paragraph are satisfied when the substrate temperature is not too high ($< 480^\circ C$). The condition 1) can also be met when desorption of As-containing species from the surface is relatively slower than their surface decomposition and when the total surface coverage of adsorbed species is very small so that their site-blocking effect on initial adsorption of TDMAAs from the gas-phase is negligible. Xi et al. [4.12] detected no other species with higher masses than dimethylamine desorbing from a GaAs(100) surface during temperature ramping from $100^\circ C$ to $500^\circ C$ after an 8×10^6 Torr-s dose of TDMAAs onto the surface. Desorption rates of TDMAAs and its As-containing intermediate decomposition products

at typical growth temperatures are very likely much slower than those of their decomposition reactions. Reaction-kinetics studies of TDMAAs surface decomposition in Chapter 3 revealed that with TDMAAs impingement, heated GaAs(100) surfaces are mainly covered by $\text{AsN}(\text{CH}_3)_2$ and As. Based on the studies there, it is reasonable to assume that the total surface coverage is negligible (< 0.1) when the substrate temperature is larger than 420 °C. In fact, our published experimental data [4.8] show that with a fixed TDMAAs flow rate, the group V-induced growth rate (Fig. 4.1) is of little variation in the temperature region of 420 °C to 470 °C. This experimental observation is not surprising and is in agreement with our discussion of satisfaction of the three conditions listed in last paragraph. In the following discussion, the absolute TDMAAs fluxes in ML/s were determined by measuring group V-induced growth rates when the substrate temperature was between 420 °C and 470 °C. Even though the absolute incident TEGa flux is unknown and dependent on growth system configuration, the relative fluxes between different mass-flow-controller flow rates are accurately known. We obtained absolute TEGa incident fluxes in ML/s in the same way as Robertson et al. did [4.1]; that is, the incident flux in ML/s corresponding to one TEGa flow rate was obtained by treating the flux as a fitting parameter to reproduce the profile of growth rate vs. substrate temperature, while incident fluxes at other flow rates were then calculated by means of linear interpolation.

Fig. 4.2 shows the experimental data points of Tu et al. [4.8] and the simulated variation of the growth rate with the substrate temperature corresponding to their growth conditions. The insert shows a typical example of RHEED oscillation with simultaneous injection of group III and group V species [4.17]. The TDMAAs flux used, 1.7 ML/s, was from Fig. 4 of their paper. An incident flux of 1.45 ML/s corresponding to TEGa MFC setting at 0.5 sccm was found to agree well with the experimental data. As described above, the kinetic parameters of this reaction model were all obtained based on data from surface-science desorption studies. Yet, with the TEGa incident flux as the only adjusting parameter, variation of the GaAs growth rate with the substrate temperature is reproduced.

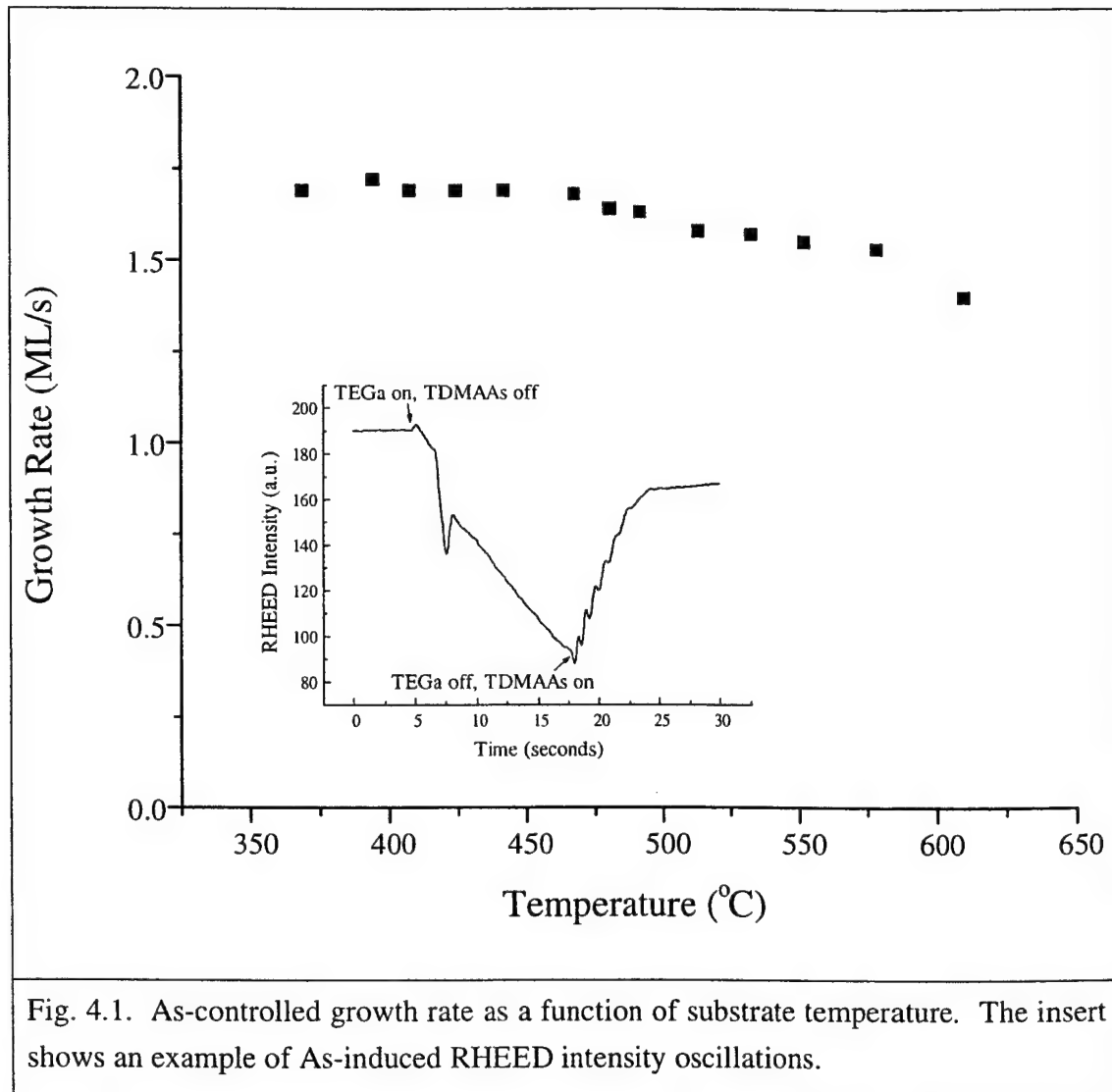


Fig. 4.3 gives simulated growth rates under a different set of incident fluxes of TEGa and TDMAAs. The TDMAAs flux, 0.79 ML/s, was determined experimentally as discussed above. With the TEGa MFC setting at 0.3 sccm, a linear scaling gives us the value of the TEGa absolute incident flux, which is 0.87 ML/s. We can see from Fig. 4.3 that even without any adjustable parameters, the simulated growth rate as a function of substrate temperature agrees very well with the experimental data.

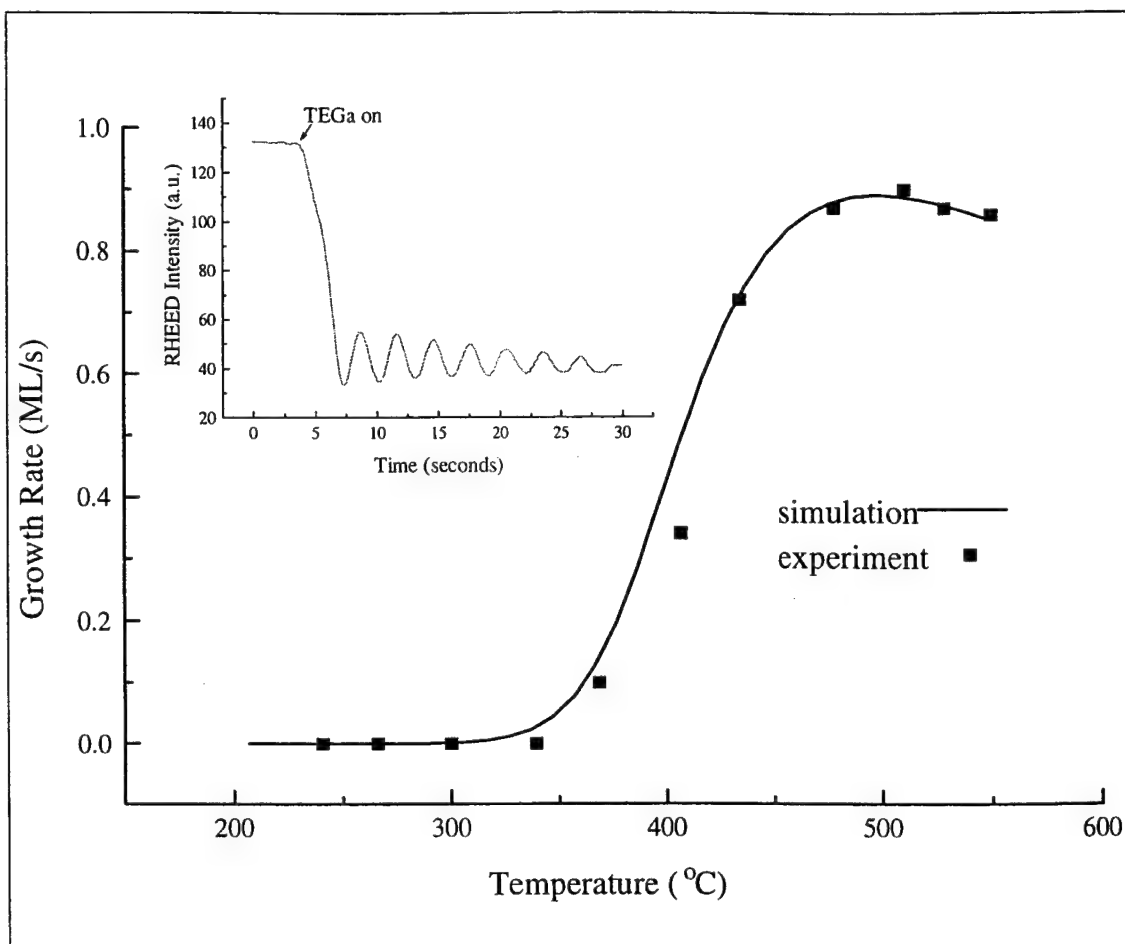


Fig. 4.2. Growth rate as a function of substrate temperature. TEGa = 0.5 sccm and TDMAAs = 1.7 ML/s.

To develop an understanding of the growth-rate variation with the substrate temperature, simulation runs for probing the sensitivities of the growth rate to reaction constants were carried out using the incident fluxes of Fig. 4.3 as inputs. Sensitivity analyses used $\frac{A_i}{R_g} \frac{\Delta R_g}{\Delta A_i}$ as the measure, where R_g is the simulated growth rate, A_i the pre-exponential factor of the i^{th} reaction in Tables 4.1 and ΔR_g the change in the growth rate corresponding to a change in A_i by ΔA_i . A series of simulation runs was performed and in one single run, the A factor of one of the reactions of Tables 4.1 was increased to five times of the value listed for the reaction in the tables. The difference in the computed growth rate between the sensitivity simulation run and that for generating Fig. 4.3 was

used to calculate the sensitivity coefficient $\frac{A_i}{R_g} \frac{\Delta R_g}{\Delta A_i}$ for the reaction. Fig. 4.4 plots the calculated coefficients of Reactions (2)-(5) and (11) of Table 4.1. These are the reactions which have larger sensitivity-coefficient values in comparison to those of other reactions. We can see that the decrease in the growth rate at elevated temperatures corresponds to the importance, as measured by the sensitivity coefficient, of the DEGa desorption reaction (Reaction (3)) at those temperatures. We can also learn from Fig. 4.4 that under the growth conditions of Fig. 4.3, the onset of growth is mainly controlled by the TEGa dissociative chemisorption reaction (Reaction (2)) and the decomposition reaction of surface ethyl species to desorb C_2H_4 (Reaction (5)). Furthermore, Fig. 4.4 reveals that group-V chemistry can affect the growth kinetics mainly through the rate-limiting step [4.7] of TDMAAs surface decomposition (Reaction (11)). This is because As-containing species can block surface sites for TEGa adsorption and decomposition, while As-containing species can leave the surface through conversion to chemisorbed As atoms and the recombinative reaction of chemisorbed As atoms (Reaction (15)). Fig. 4.5 shows the simulated growth rate with the same TEGa flow rate but a different TDMAAs incident flux (3ML/s) from that of Fig. 4.3. We can see that significant concentrations of surface group-V species can decrease the GaAs growth rate.

Fig. 4.6 displays coverage of surface species under the incident fluxes of Fig. 4.2. The surface coverages of the parent molecules (TEGa and TDMAAs) are very small because they dissociate immediately once physisorbed onto a GaAs(100) surface. The intermediate decomposition products $Ga(C_2H_5)_2$ and $As(N(CH_3)_2)_2$ also decompose quickly and thus, exhibit small surface concentrations. Surface species which have relatively longer lifetimes are chemisorbed As atoms, ethyl radicals and monodimethylamino arsine ($AsN(CH_3)_2$). The coverages of $AsN(CH_3)_2$ and As are significant up to 420 °C. Our investigation on the mechanisms responsible for Ar⁺-laser induced GaAs growth enhancements, which will be reported elsewhere, reveals that observed temperature windows of growth-enhancements correlate well with predicted DEGa surface-coverage variations with the substrate temperature. The successful predication of DEGa surface coverage at low growth temperatures implies that this reaction model delineates the underlining surface chemistry well.

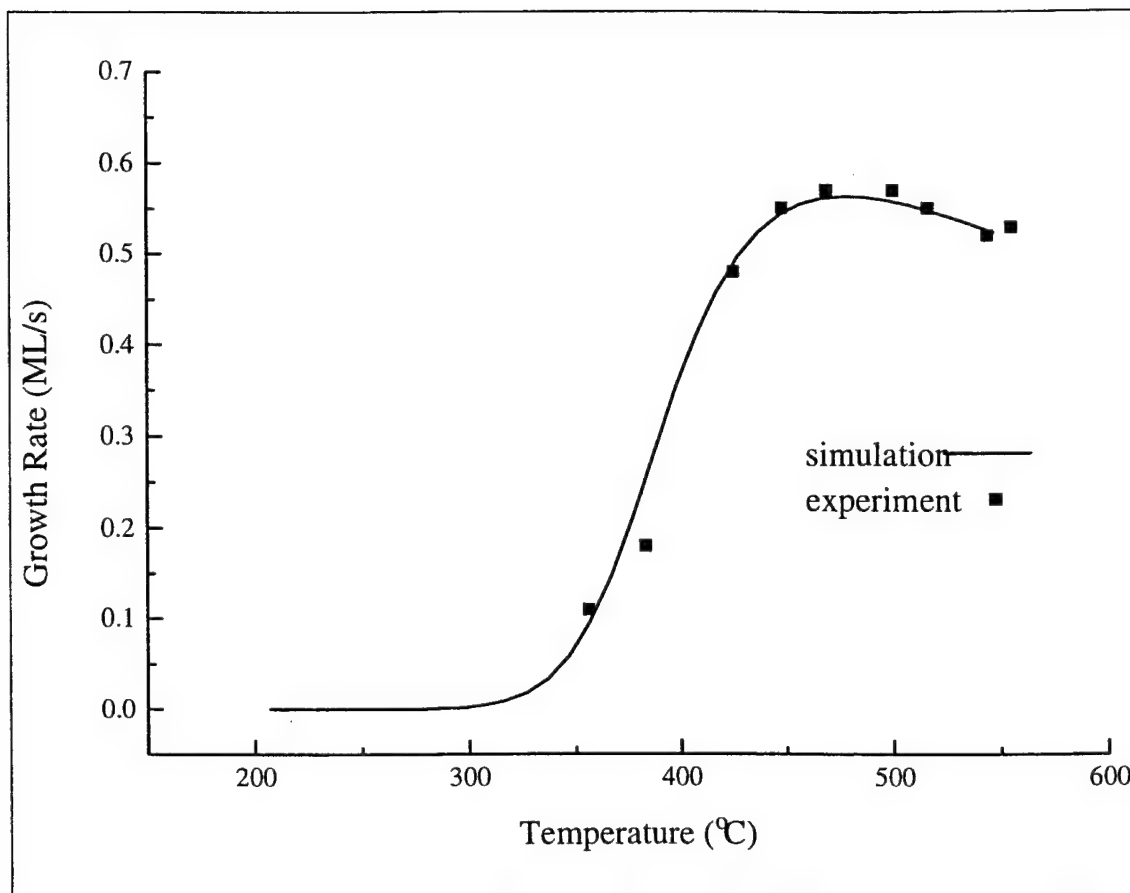


Fig. 4.3. Growth rate as a function of substrate temperature. TEGa = 0.3 sccm and TDMAAs = 0.79 ML/s.

In chemical beam epitaxy, metalorganic species may not decompose immediately after their impingement onto a substrate surface. Therefore, the steady state of a CBE surface reaction system may not be established for a certain amount of time after onset of growth, especially when the substrate temperature is low. To explore this issue, we use our reaction model to simulate the transient growth which resulted from incidence of a TEGa flux and a TDMAAs flux onto a substrate on which a steady state has already been established under the TDMAAs flux. The TEGa and TDMAAs flux values are identical to those of Fig. 4.3. The curve of Fig. 4.7 gives the time for the growth to reach a steady state as a function of the substrate temperature. The onset temperature of monodimethylamino arsine ($\text{AsN}(\text{CH}_3)_2$) decomposition is around 270 °C. Between 270

°C and 300 °C, the decomposition is not efficient enough that the species is the slowest among all surface species to reach a steady state, limiting the speed of the whole surface phase to reach a steady state. This is why the solid curve exhibits a smaller slope in that temperature region. We can see from Fig. 4.7 that it can take up to tens of seconds for the surface system to reach steady states at low temperatures.

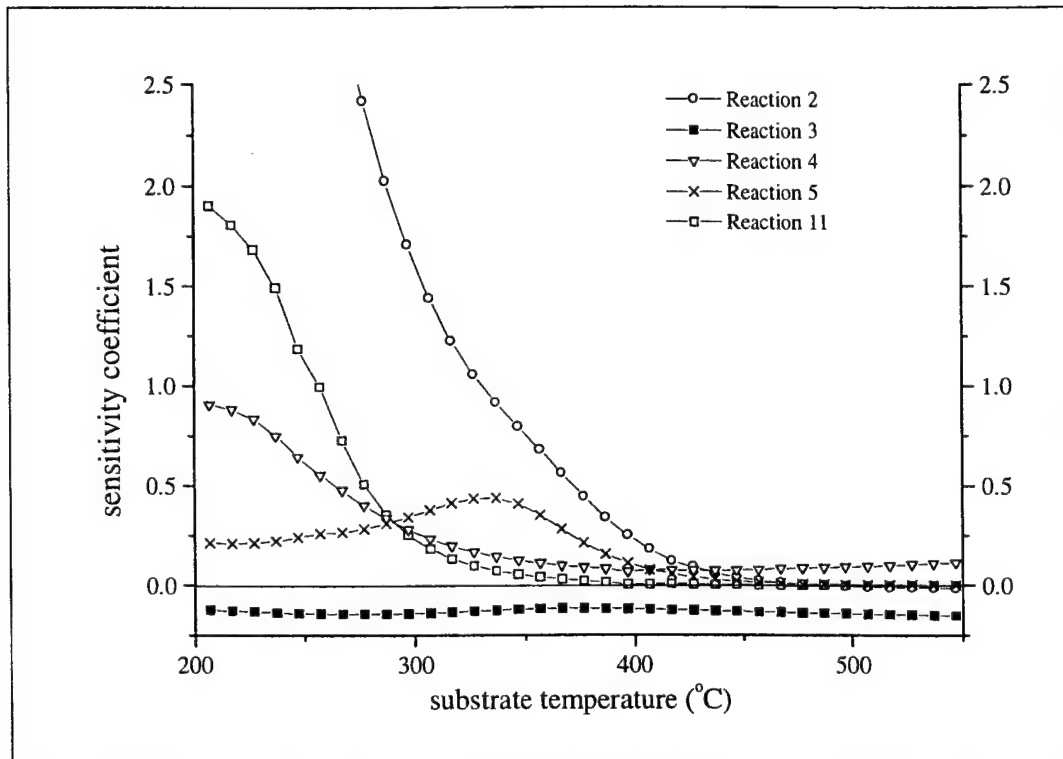


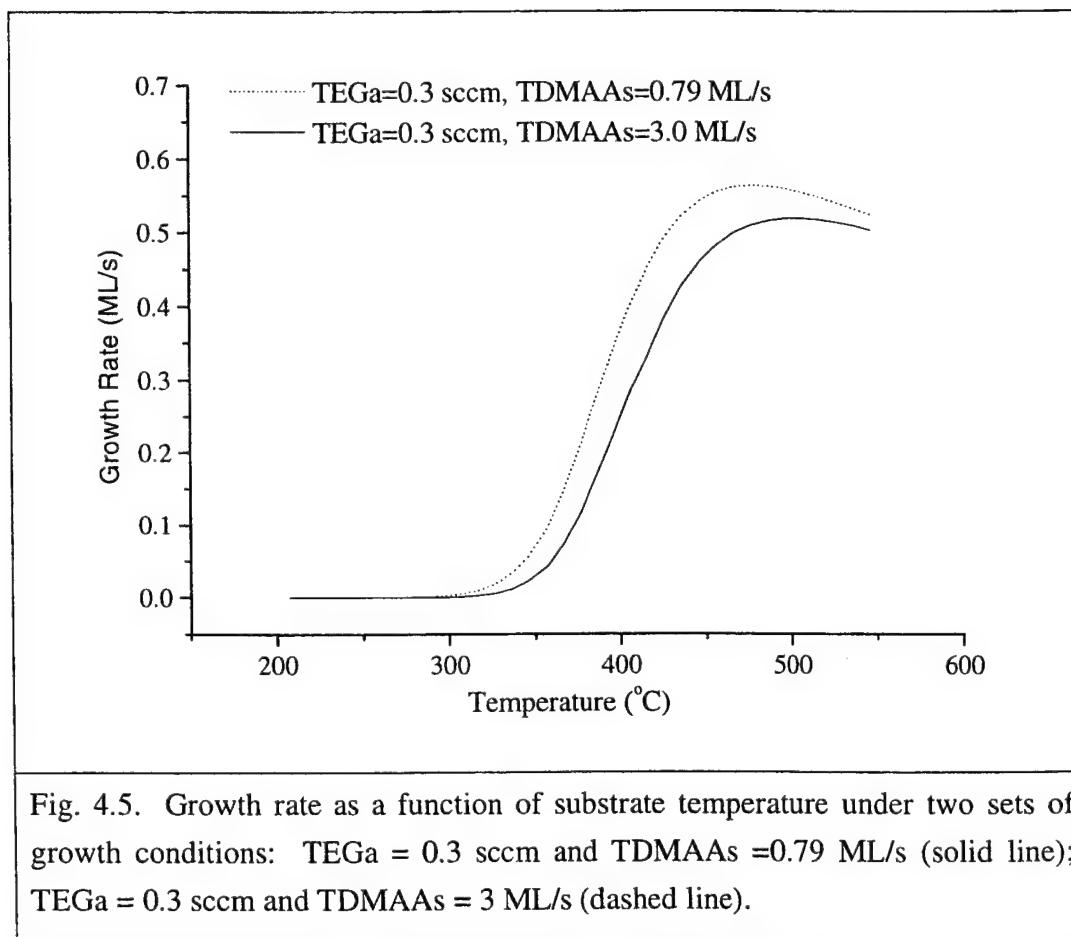
Fig. 4.4. Calculated sensitivity coefficients $\frac{A_i}{R_g} \frac{\Delta R_g}{\Delta A_i}$ of Reactions (2-5) and (11) of

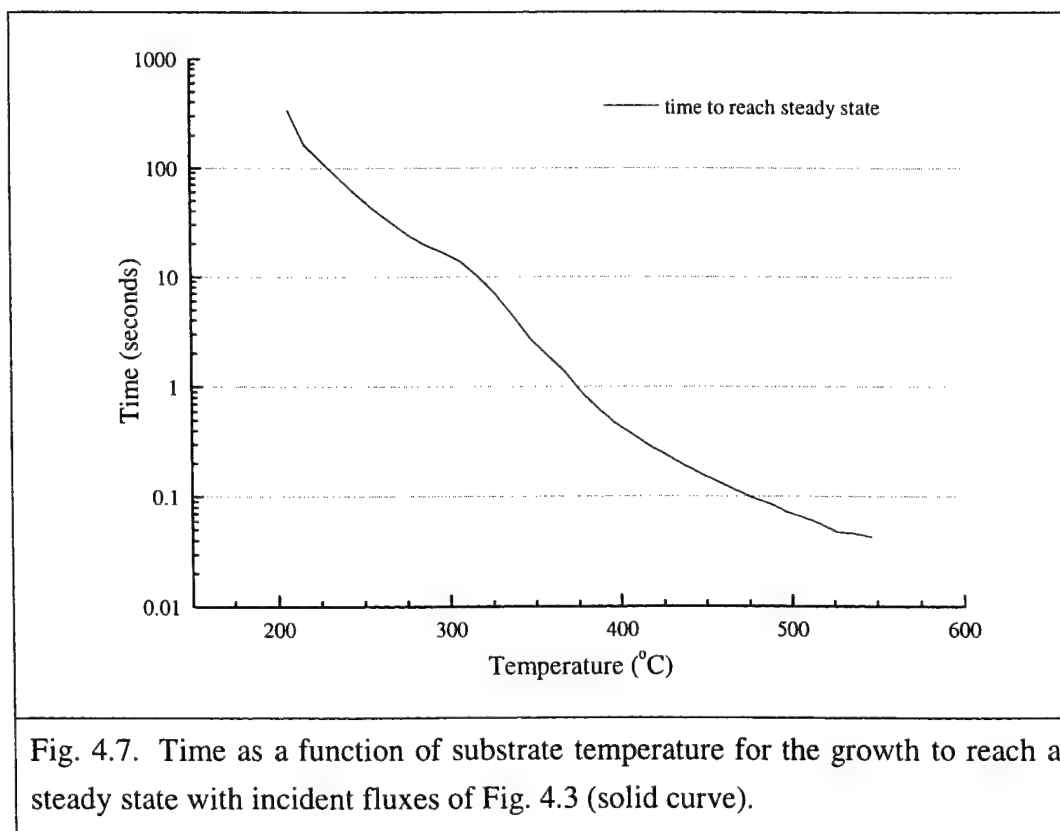
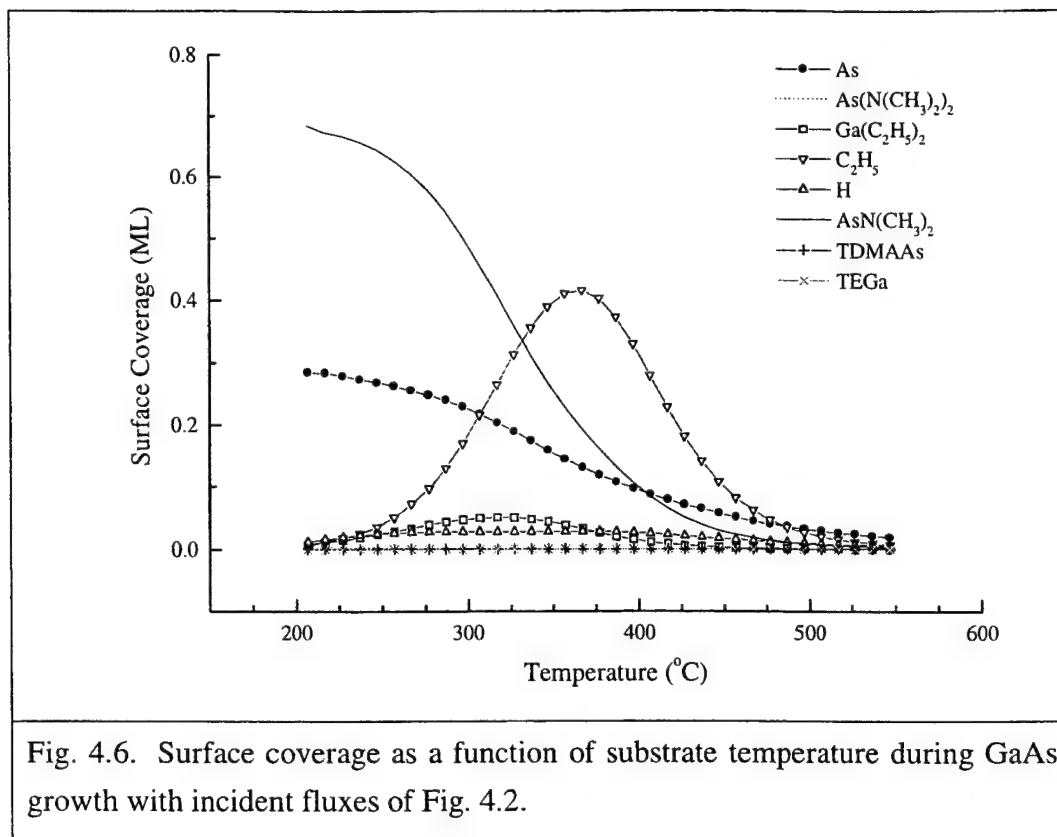
Table 4.1. ΔR_g is the change in the growth rate corresponding to a change in the pre-exponential factor of the i^{th} reaction by ΔA_i . The precursor incident fluxes assumed for computing R_g and ΔR_g are those of Fig. 4.3.

4.4 Summary

A GaAs CBE reaction model has been developed. This model is different from previous GaAs growth models in the literature in that it involves surface decomposition

and interaction of two metalorganic species, each of which possesses complicated surface decomposition kinetics. Arguments have been presented regarding developing a technique for obtaining the absolute group-V incident flux directly from experiment. It has been demonstrated that properly combining reaction mechanisms derived from surface-science desorption studies enables us to predict the growth rate without adjustable parameters. In addition, sensitivity analyses have been performed to develop a understanding of GaAs CBE growth kinetics. The model is also used to predict how fast a CBE reaction system reaches a steady state.





References

- [4.1] A. Robertson, Jr., T.H. Chiu, W.T. Tsang and J.E. Cunningham, *J. Appl. Phys.* 64 (1988) 877.
- [4.2] V.M. Donnelly and A. Robertson, Jr., *Surface Science* 293 (1993) 93.
- [4.3] B.W. Liang and C.W. Tu, *Appl. Phys. Lett.* 57 (1990) 689.
- [4.4] A.J. Murrell, A.T.S. Wee, D.H. Fairbrother, N.K. Singh, J.S. Foord, G.J. Davies and D.A. Andrews, *J. Appl. Phys.* 68 (1990) 4053.
- [4.5] C.L. French and J.S. Foord, *J. Crystal Growth* 120 (1992) 63.
- [4.6] J.S. Foord, C.L. French, C.L. Levoguer and G.J. Davies, *Phil. Trans. R. Soc. Lond. A* 344 (1993) 507.
- [4.7] B.Q. Shi and C.W. Tu, *J. Electr. Mat.*, Vol. 28, No. 1, (1999) 43-49.
- [4.8] C.W. Tu, H.K. Dong and N.Y. Li, *Materials Chemistry and Physics* 40 (1995) 260.
- [4.9] H.K. Dong, Ph. D Thesis (University of California at San Diego, 1995).
- [4.10] R. Fowler and E.A. Guggenheim, *Statistical Thermodynamics* (University Press, Cambridge, 1952).
- [4.11] C.G. Goymour and D.A. King, *J. Chem. Soc. Faraday I* 69 (1973) 749.
- [4.12] M. Xi, S. Salim, K.F. Jensen and D.A. Bohling, *Mat. Res. Soc. Symp. Proc.* 334 (1994) 169.
- [4.13] S. Salim, J.P. Lu, K.F. Jensen, *J. Crystal Growth* 124 (1992) 16.
- [4.14] K. Kimura, S. Horiguchi, K. Kamon, M. Mashita, M. Mihara and M. Ishii, *Jpn. J. Appl. Phys.* 26 (1987) 419.
- [4.15] C.R. Abernathy, P.W. Wisk, D.A. Bohling and G.T. Muhr, *Appl. Phys. Letters* 60 (1992) 2421.
- [4.16] C.W. Gear, *Numerical Initial Value Problems in Ordinary Differential Equations* (Prentice-Hall, Englewood Cliffs, New Jersey, 1971).
- [4.17] H.Q. Hou, B.W. Liang, T.P. Chin, and C.W. Tu, *Appl. Phys. Lett.* 59 (1991) 292.
- [4.18] J.R. Arthur, *Surface Sci.* 43 (1974) 449.

CHAPTER 5

EVALUATIONS OF Ar^+ -LASER INDUCED TEMPERATURE RISE OF SEMICONDUCTOR SURFACES

5.1 Introduction

The CBE system used in this study is a modified Perkin-Elmer 425 MBE system, equipped with gas lines for metalorganic species and a 1600 l/s turbomolecular pump. Fig. 5.1 is a schematic cross-sectional view of the system with addition of laser optics. The reflection mirrors R1 and R2 are galvanometer-controlled turning mirrors. Motions of the two mirrors allow scanning the laser beam over the substrate surface. The center of the laser-scanned area is controlled by the offset settings of the two galvanometers. The laser-irradiated areas used here for investigations of laser-assisted growth and doping of GaAs and InP by CBE were 1 mm x 1 mm or 1.5 mm x 1.5 mm rectangles. The laser power varied from 4 W to 7 W. Different combinations of frequencies of the rotating mirrors R1 and R2 were employed in this study.

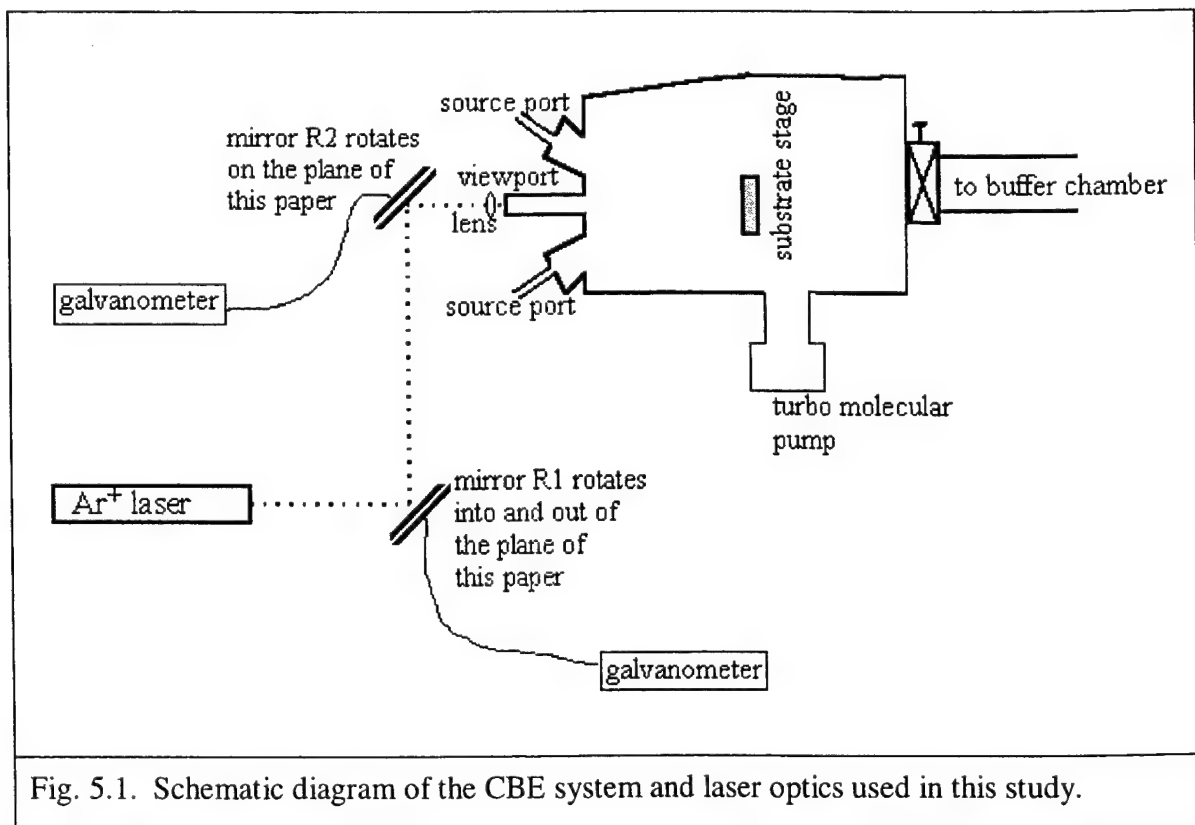


Fig. 5.1. Schematic diagram of the CBE system and laser optics used in this study.

The photon energy of the Ar⁺ laser used in this study is 2.54 eV, while the bandgaps of GaAs and InP are 1.43 eV and 1.35 eV, respectively [5.1]. Therefore, GaAs and InP substrates are not transparent to the laser light and there exist localized heating and photo-generated carriers associated with Ar⁺-laser assisted epitaxy of GaAs and InP. Decomposition reactions of a metalorganic molecule on a substrate surface involve breaking up of covalent bonds within the molecule and formation of new covalent bonds between atoms of the molecule and/or surface dangling bonds. Breaking up of a chemical bond is a process of overcoming an energy barrier which resulted from mutual attractions of the two pairing electrons of the bond. Thus, an activation energy is required for a decomposition reaction to occur. An adsorbed molecule in equilibrium with the substrate surface can acquire thermal energy through its interactions with the substrate lattice. The probability that the molecule acquires enough thermal energy to activate its decomposition processes depends on the substrate temperature. The higher the substrate temperature, the more likely its decomposition can be activated. Therefore, it is imperative for us to consider laser-induced heating of substrates in any attempt to explain laser-induced growth and doping modulations. In this chapter, a heat diffusion equation for semiconductors is solved analytically and temperature rise associated with the scanning laser beam of Fig. 5.1 is calculated for the case of the substrate being GaAs.

5.2 Solutions of a heat diffusion equation for semiconductors

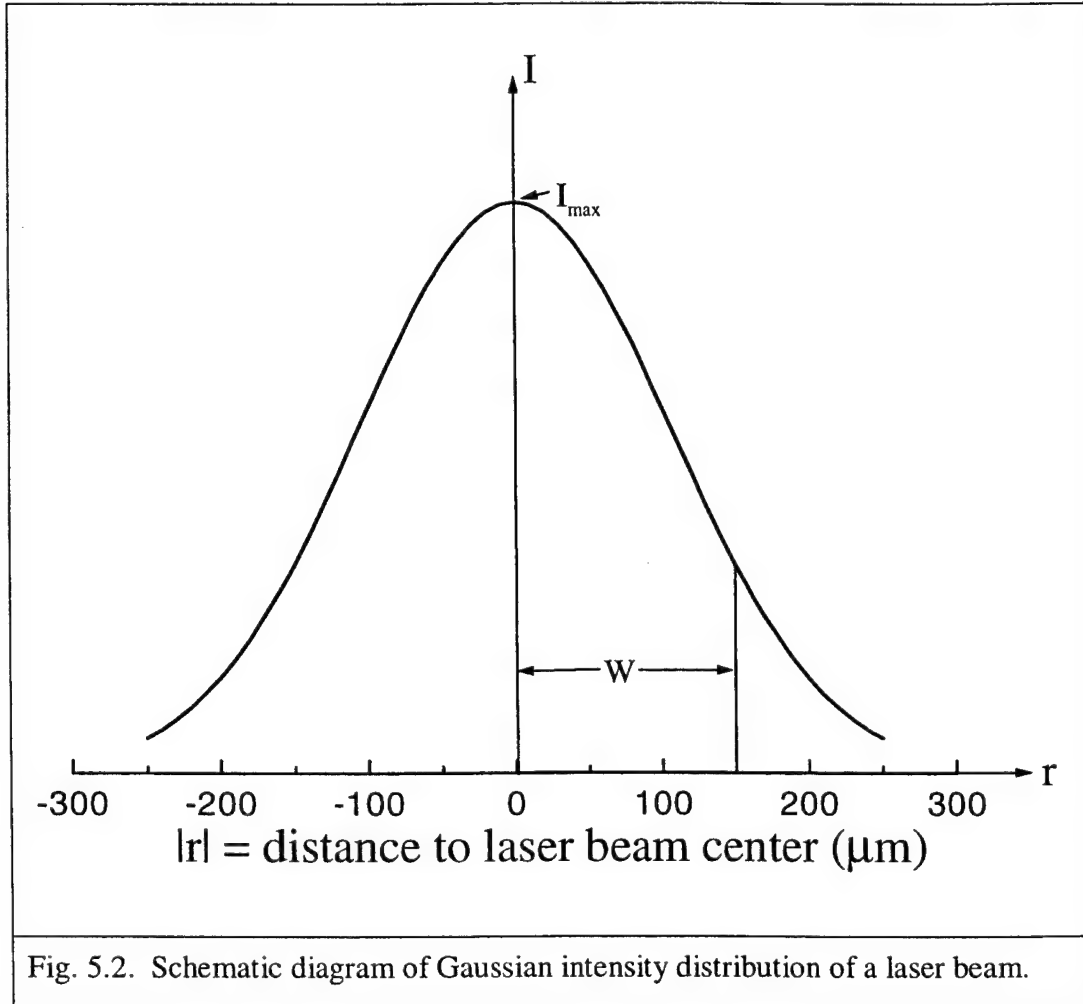
The laser beam of Fig. 5.1 has a Gaussian intensity distribution as depicted in Fig. 5.2,

$$I = I_{\max} \exp\left(-\frac{r^2}{w^2}\right), \quad (5.1)$$

where I is the power intensity of the laser beam, r the distance from the beam center, and w the beam waist. In our experimental setup, the laser beam passes a focusing lens prior to its entrance into the chamber and the diameter of the laser beam on the substrate is approximated 400 μm [5.2]. Therefore, the beam waist w is approximately 150 μm . With the assumption that the absorption coefficient of the substrate does not vary laterally on the substrate plane, the beam width w can be treated as a constant (i.e.,

without dependence on the depth into the substrate). The total incident power P is the integration of I over the substrate surface plane and

$$P = \int_0^{\infty} I_{\max} \exp\left(-\frac{r^2}{w^2}\right) 2\pi r dr = I_{\max} \pi w^2. \quad (5.2)$$



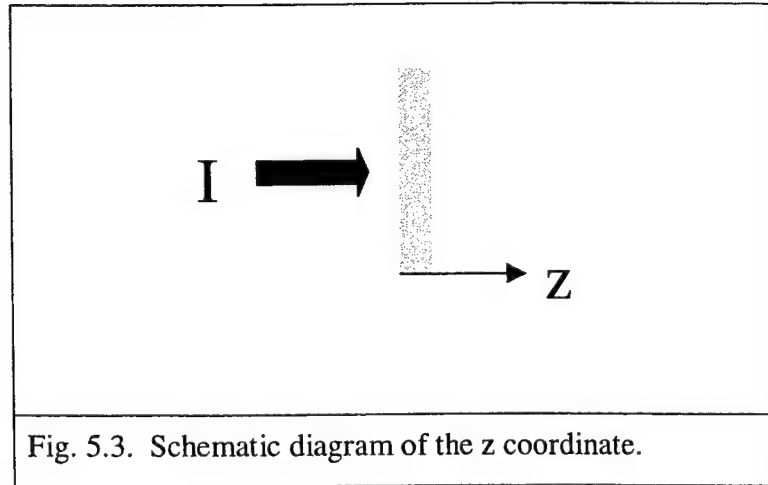
The conventional equation for temperature in a solid can be written [5.3]

$$c\rho \frac{\partial T}{\partial t} = K_0 \nabla \cdot (\nabla T) + Q \quad (5.3)$$

where T is the temperature, c the specific heat capacity, ρ the mass density of the solid, K_0 the thermal conductivity and Q the heat energy input rate per unit volume. In writing down Equation (5.3), an assumption has been made that the variation of K_0 with temperature is sufficiently small so that K_0 can be treated as a constant in the solid. This assumption implies that Ar^+ -induced temperature rises are not large enough so that we do not have to take into account the variation of K_0 . For the case of a laser beam parallel to the z axis and impinging on the surface of a uniform semiconductor at $z = 0$ (Fig. 5.3), the Q term can be expressed as

$$Q = \alpha I_{\max} (1 - R) \exp(-\alpha z) \exp\left(-\frac{r^2}{w^2}\right), \quad (5.4)$$

where α is the absorption coefficient of the semiconductor at the wavelength of the laser and R the surface reflectivity of the semiconductor.



Outside of the laser-irradiated area, the temperature is also governed by Equation (5.3) with $Q = 0$. Far away from the laser-irradiated area, the temperature is not affected by laser irradiation and is equal to the normal growth temperature without laser irradiation T_n . Let ζ be the difference between T and T_n ,

$$\zeta = T - T_n \quad (5.5)$$

The boundary conditions on the plane of the substrate is then

$$\zeta \rightarrow 0 \text{ as } x \rightarrow \pm \infty \text{ or } y \rightarrow \pm \infty. \quad (5.6)$$

The boundary condition on the semiconductor surface exposed to the vacuum of the chamber is

$$R(T_s) = K_0 \frac{\partial T}{\partial z}, \text{ at } z=0, \quad (5.7)$$

where $R(T_s)$ is the radiation from the surface into the vacuum and R is a function of the semiconductor surface temperature T_s . Neglecting the increase in R associated with temperature rise on the Ar^+ -laser irradiated area, we can have the boundary condition for the laser-induced temperature rise ζ ,

$$0 = K_0 \frac{\partial \zeta}{\partial z}, \text{ at } z=0. \quad (5.8)$$

ζ computed using the boundary condition (5.8) should, in principal, overestimate the temperature rise because R increases with temperature. But the variation of R with temperature is small and the boundary condition should be a good approximation if the Ar^+ -laser induced temperature rises are only tens of Celsius degrees. The boundary condition on the side of the substrate where thermal contact for heating is made is more complicated. Two cases are investigated in this chapter. In one case, the semiconductor is assumed to be of an infinite thickness and therefore,

$$\zeta \rightarrow 0 \text{ as } z \rightarrow \infty. \quad (5.9)$$

In the other case, the temperature rise which resulted from laser irradiation is assumed to dissipate completely at the thermal contact, that is,

$$\zeta = 0 \text{ at } z = h, \quad (5.10)$$

where h is the thickness of the substrate. Since in reality the thermal contact at $z = h$ actually acts as a heat sink for the laser-induced temperature rise, the actual temperature

rise should be in between the computed results using Conditions (5.9) and (5.10). In the next section, sensitivity of the temperature rise on the vacuum-side surface of a GaAs substrate to the setting of the boundary condition on the other side will be evaluated. Our investigation of Ar⁺-laser induced temperature rise, thus, involves solving the partial differential equation

$$c\rho \frac{\partial \zeta}{\partial t} = K_0 \nabla \cdot (\nabla \zeta) + Q \quad (5.11)$$

along with Conditions (5.4), (5.6), (5.8) and (5.9) or (5.10).

Lax [5.4] performed analytic studies of Equation (5.11) with Conditions (5.4), (5.6), (5.8) and (5.9) for the case of a stationary laser beam and derived the steady-state temperature rise in a semiconductor associated with laser irradiation of the semiconductor. He showed that the steady-state surface temperature rise at the center of the laser beam

$$\zeta(r=0, t=\infty) \rightarrow \frac{P}{2K_0 w \sqrt{\pi}}, \text{ as } \alpha \rightarrow \infty. \quad (5.12)$$

Cline et al. [5.5] investigated the temperature rise associated with a circular cw laser beam doing line scans at constant velocities. The governing equation and conditions used were the same as those used by Lax [5.4]. Nissim et al. [5.6] used Equation (5.11) with Conditions (5.6), (5.8) and (5.9) and a modified version of Condition (5.4) for an elliptical cw laser beam to evaluate the temperature rise in a semiconductor resulted from irradiation of the laser moving along a straight line at various velocities. Since in our experiments the Ar⁺-laser of Fig. 1 moves in both x and y directions on the substrate plane, a more general mathematical solution is needed to evaluate the laser induced temperature rise. A standard Green's function analysis [5.3] is used here.

The Green's function corresponding to Conditions (5.6), (5.8) and (5.9) or (5.10) is

$$G(\vec{x}, t; \vec{x}_0, t_0) = \left[\frac{1}{4\pi k(t-t_0)} \right]^{3/2} \left\{ \exp \left[-\frac{(x-x_0)^2 + (y-y_0)^2 + (z-z_0)^2}{4k(t-t_0)} \right] + \exp \left[-\frac{(x-x_0)^2 + (y-y_0)^2 + (z+z_0)^2}{4k(t-t_0)} \right] \right\}, \quad (5.13)$$

where $k = K_0/c\rho$ and is called thermal diffusivity. With the assumption that the temperature rise prior to onset of laser irradiation is zero, the temperature rise expressed in terms of the Green's function is

$$\zeta(x, y, z, t) = \int_0^t dt_0 \int_{-\infty}^{\infty} dx_0 \int_{-\infty}^{\infty} dy_0 \int_0^L dz_0 G(\vec{x}, t; \vec{x}_0, t_0) q(\vec{x}_0, t_0), \quad (5.14)$$

where $L = \infty$ for the case of Condition (5.9), $L = h$ for the case of Condition (5.10) and

$$q(\vec{x}_0, t_0) = q_{\max} \exp(-\alpha z) \exp\left(-\frac{r^2}{w^2}\right), \text{ and } q_{\max} = \frac{\alpha I_{\max} (1-R)}{c\rho}, \quad (5.15)$$

with r in Equation (5.4) for Q given by

$$r^2 = (x_0 - x_c)^2 + (y_0 - y_c)^2, \quad (5.16)$$

where x_c and y_c are the location coordinates of the center of the laser beam, which are functions of time when the laser beam moves. Analytical expressions can be obtained for the x_0 and y_0 direction integrals of Equation (5.14). And the equation is then converted to

$$\zeta(x, y, z, t) = \frac{\alpha}{c\rho} \frac{P}{\pi w^2} \left(\frac{1}{4\pi k} \right)^{3/2} \int_0^t \left(\frac{1}{t-t_0} \right)^{3/2} F_x F_y (F_{z+} + F_{z-}) dt_0, \quad (5.17)$$

where

$$F_x = \frac{\sqrt{\pi}}{\sqrt{\frac{1}{w^2} + \frac{1}{4k(t-t_0)}}} \exp \left\{ -\frac{x_c^2}{w^2} - \frac{x^2}{4k(t-t_0)} + \frac{\left[\frac{x_c}{w} + \frac{x}{4k(t-t_0)} \right]^2}{\frac{1}{w^2} + \frac{1}{4k(t-t_0)}} \right\}, \quad (5.18)$$

$$F_y = \frac{\sqrt{\pi}}{\sqrt{\frac{1}{w^2} + \frac{1}{4k(t-t_0)}}} \exp \left\{ -\frac{y_c^2}{w^2} - \frac{y^2}{4k(t-t_0)} + \frac{\left[\frac{y_c}{w} + \frac{y}{4k(t-t_0)} \right]^2}{\frac{1}{w^2} + \frac{1}{4k(t-t_0)}} \right\}, \quad (5.19)$$

$$F_{z+} = \int_0^L \exp(-\alpha z_0) \exp \left[-\frac{(z-z_0)^2}{4k(t-t_0)} \right] dz_0, \quad (5.20)$$

and

$$F_{z-} = \int_0^L \exp(-\alpha z_0) \exp \left[-\frac{(z+z_0)^2}{4k(t-t_0)} \right] dz_0, \quad (5.21)$$

5.3 Calculation of laser-induced temperature rise

It is worth pointing out that Equation (5.17) can be used to calculate temperature rise in a solid associated with irradiation of a circular cw laser without restricting the way in which the laser scans the surface of the solid. In this section, the solid is assumed to be GaAs and the motion of the Ar⁺ laser in our experiment is specified mathematically. Results from this section will be used in the next chapter for investigation on the mechanisms responsible for observed Ar⁺-laser-induced growth enhancements.

Table 5.1 lists the values of physical properties of GaAs needed for calculation of laser-induced temperature rise. In this section, the values of the properties used in the calculation are those of GaAs at 350 °C (that is, the substrate temperature is assumed to be at 350 °C). Approximately 53% of the laser power output impinges on the substrate surface in our experimental setup (Fig. 5.1) due to the imperfect reflectivity of the reflection mirrors and lens transmittance [5.2]. Throughout this section, the value of P used in Equation (5.17) is equal to the laser power multiplied by 0.53. Integration

subroutines of the IMSL library developed by Visual Numerics, Inc. are employed to numerically obtain temperature rise. The IMSL subroutine QDAGS which integrates functions of endpoint singularities is called to perform the integration in Equation (5.17), while IMSL subroutines QDAGI and QDAG, both of which use globally adaptive schemes, are called to efficiently calculate the integrals in Equations (5.20) and (5.21) for the cases of $L = \infty$ and $L=h$, respectively. A straightforward dummy-variable transformation $u = \alpha z_0$ is applied to Equations (5.20) and (5.21) for numerical integration purpose to remove the numerical singularity associated with very large values of GaAs absorption coefficient ($\sim 4 \times 10^4 \text{ cm}^{-1}$) at the wavelength of the laser of Fig. 5.1. According to the technical manual for the galvanometers of Fig. 5.1 [5.9], the laser beam is assumed to undergo saw-tooth oscillations and the motion of its center is specified as the following:

$$x_c = -\frac{l_x}{2} + \frac{(t_0 - nt_x)}{t_x} l_x, \text{ for } nt_x \leq t_0 < (n+1)t_x, \text{ and} \quad (5.22)$$

$$y_c = -\frac{l_y}{2} + \frac{(t_0 - mt_y)}{t_y} l_y, \text{ for } mt_y \leq t_0 < (m+1)t_y, \quad (5.23)$$

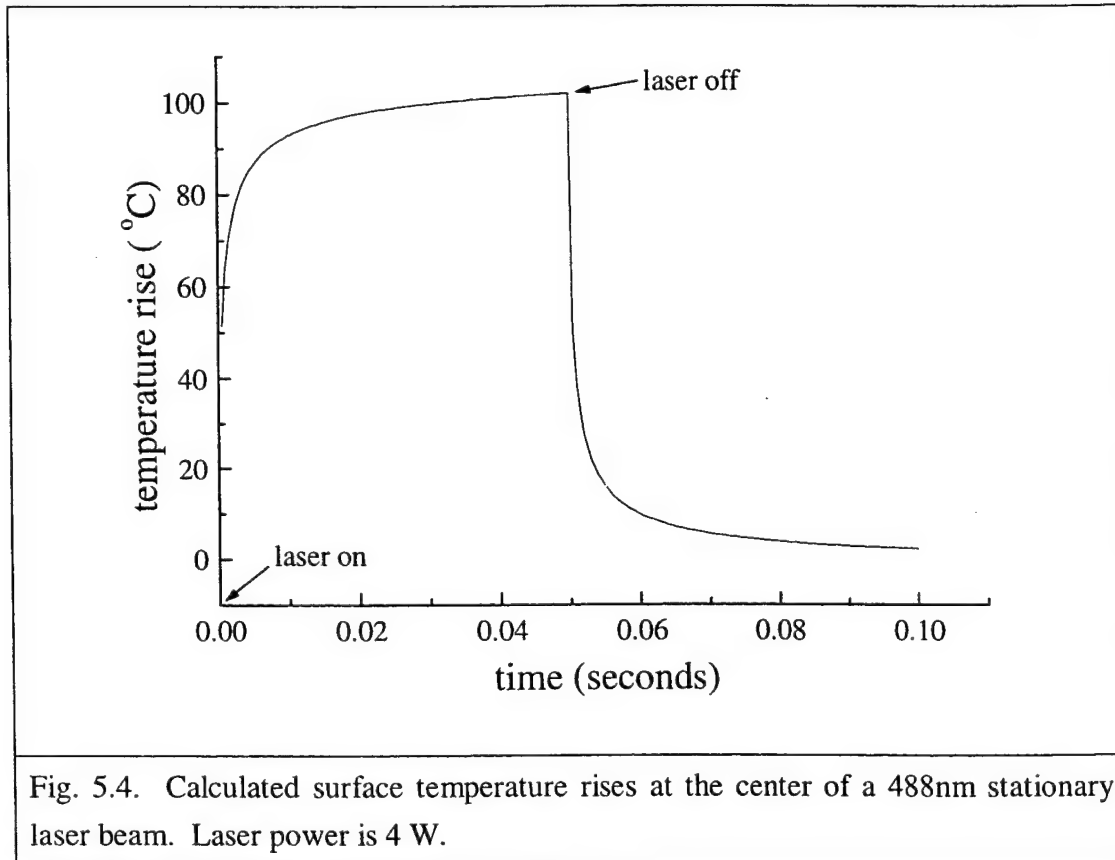
where n and m are $0, 1, 2, 3, \dots$, l_x and l_y are the dimensions of the scanned area on the substrate surface and t_x and t_y are the inverses of scanning frequencies of the two galvanometers of Fig. 5.1.

Table 5.1: Constants used in calculations of laser-induced temperature rise in GaAs

constant	units	s.i.-GaAs	reference
ρ	g cm^{-3}	5.317	[5.7]
c	$\text{J g}^{-1} \text{K}^{-1}$	$0.302 + 8.1 \times 10^{-5} \times T$	[5.7]
K_0	$\text{W K}^{-1} \text{cm}^{-1}$	$549.356 \times T^{-1.25}$	[5.8]
E_g	eV	$1.424 - 5.405 \times 10^{-4} \times (T^2 / (204 + T) - 300^2 / 504)$	[5.8]
α	cm^{-1}	$3.5 \times 10^4 \times (E_p - E_g)^{0.5}$	[5.8]
R		0.515	[5.2],[5.7]
(Note that E_p is the energy of incident photons)			

To test the analytical expressions derived in the last section for laser-induced temperature rise, the case of a stationary Ar^+ -laser beam is investigated first. Fig. (5.4) shows the computed temperature rise at the center of the laser beam when the laser power is 4 W. The substrate is assumed to be of an infinite thickness (L of Equations (5.20) and (5.21) = ∞ in the computation). The laser beam is turned on at time zero and off at 0.05 seconds into irradiation. We can see that the substrate temperature rises and falls in a time frame of 10^{-3} seconds after the laser beam is switched on and off. With a stationary laser, the surface temperature rise at the center of the laser beam is a function of w , k , q_{\max} , α and t , i.e.,

$$\zeta = f(w, k, q_{\max}, \alpha, t). \quad (5.24)$$



A dimensional analysis leads to

$$\frac{\zeta(0,0,0,t)}{q_{\max} t} = g\left(\frac{w^2}{kt}, \alpha w\right) \quad (5.25)$$

where g is an unspecified function. The absorption coefficient $\alpha = 39535 \text{ cm}^{-1}$ at 350°C and $w = 0.015 \text{ cm}$, so the αw variable of Equation (5.25) can be effectively treated as infinite. The value of w^2/kt governs the laser-induced temperature rise and fall and w^2/k is the time scale for the temperature variation associated with laser irradiation being on or off. At 350°C , k is approximated $0.2 \text{ cm}^2/\text{s}$. Therefore, w^2/k is approximately 10^{-3} seconds, which is a value consistent with the numerical computation as shown in Fig. (5.4). It is evident, then, that the fact that the substrate temperature rises and falls quickly is due to the small size of the focused laser beam on the substrate. We also see that to numerically investigate the heating effect of the scanning laser on surface reaction dynamics, the time step has to be much less than 10^{-3} seconds.

Fig. 5.4 also shows that when a GaAs substrate is under a stationary Ar^+ -laser of 4 W power, the steady-state surface temperature rise at the center of the laser beam is approximately 102°C . Using $K_0 = 0.18$ at 350°C , Expression (5.12) reveals that the temperature rise should approach 109°C as the absorption coefficient approaches infinite. We thus see that calculation based on the formula of the last section is in line with the analytical Expression (5.12) reported in the literature and that the absorption coefficient of GaAs, owing to its being of a direct bandgap, is indeed very large.

Fig. 5.5 displays the computed surface temperature rise for the case of a scanning Ar^+ -laser beam of 4 W power. The substrate is assumed to be of an infinite thickness (L of Equations (5.20) and (5.21) $= \infty$ in the computation). The scanned area is a $1 \text{ mm} \times 1 \text{ mm}$ square and the scanning frequencies are 40 and 50 Hz along the two dimensions of the square. Data points displayed are the temperature rise at the center of the scanned area at instants of a 0.6 second interval. We can see that the temperature rise stabilizes in a time frame of seconds for the sampling time interval. Fig. 5.6 plots the computed surface rises under the same experimental conditions as those of Fig. 5.5 but with computation at instants of a 0.0005 second interval from 59 seconds to 59.2 seconds into the laser irradiation. The time interval is one half of the time scale of the temperature rise induced by a stationary laser beam for our experiment setup. The figure reveals temperature spikes as large as 90°C associated with passing by of the laser beam. The average temperature rise over the 0.2 second is 31.6°C , and in 54% of the time the

temperature rise is between 20 °C and 30 °C. The results are consistent with our interferometry measurement [5.2] which found a laser-induced substrate temperature rise of 25 °C with the irradiation conditions of Figs. 5.5 and 5.6.

To test the sensitivity of the laser-induced temperature rise to scanning frequencies, a calculation is done for the case of experimental conditions of Fig. 5.5 but with the scanning frequencies being 20 and 30 Hz. Computation is done at instants of a 0.0005 second interval from 59 seconds to 59.2 seconds into the laser irradiation. Results are shown in Fig. 5.7. The temperature spikes are around 70 °C in this case. The average temperature rise over the 0.2 second is 31.3 °C, and in 57% of the time the temperature rise is between 20 °C and 30 °C. We thus see that the temperature rise averaged over time is not sensitive to the settings of the scanning frequencies.

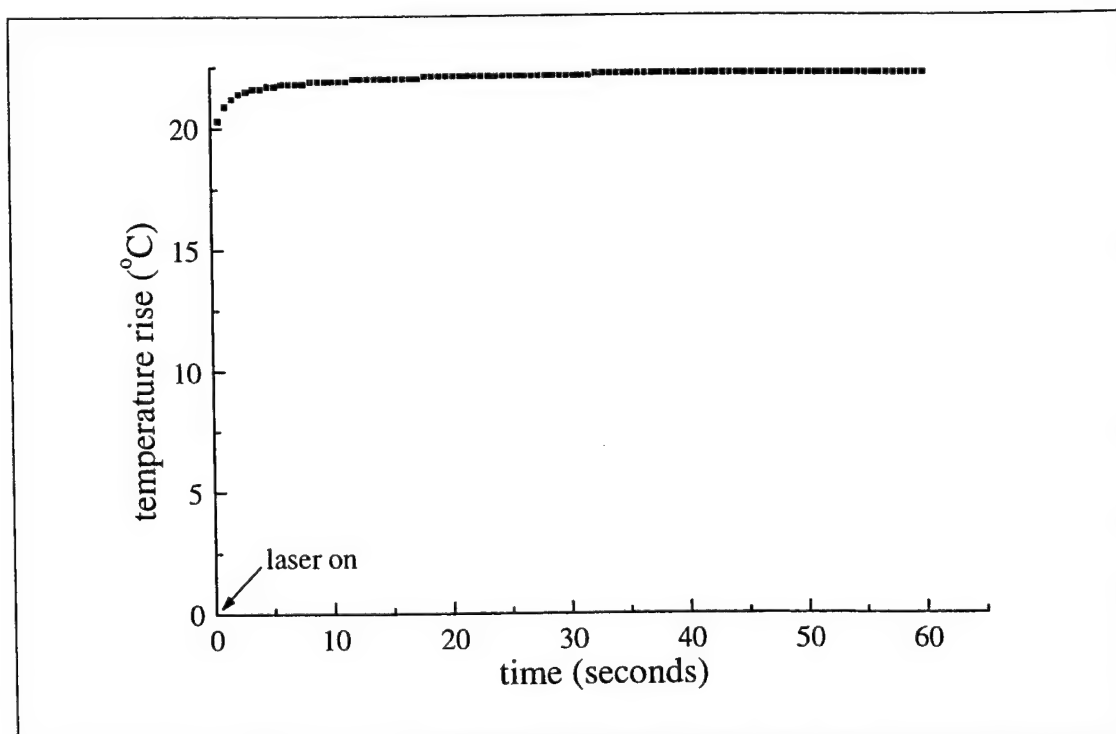


Fig. 5.5. Calculated surface temperature rises at center the area scanned by a 488 nm laser beam. The substrate is assumed to be of an infinite thickness. Data points are the temperature rises at instants of 0.6 second interval. Laser power is 4 W. The scanned area is an 1 mm x 1 mm square and the scanning frequencies are 40 and 50 Hz along the two dimensions of the square.

Fig 5.8 is for assessing the effects of the setting of L in Equations (5.20) and (5.21) on computed temperature rises. The data points are obtained with the same assumptions for computation as employed for producing Figs. 5.5 and Fig. 5.6 except that the thickness of the substrate is assumed to be 0.65 mm in this figure, which is the typical thickness of 3" GaAs wafers. Results of Fig. 5.8 are essentially identical to those of Fig. 5.6. We can see that because of complete absorption of Ar^+ -laser irradiation light within thin layers beneath surfaces of GaAs substrates, the substrates can be effectively assumed to be of an infinite thickness for computing laser-induced surface temperature rise.

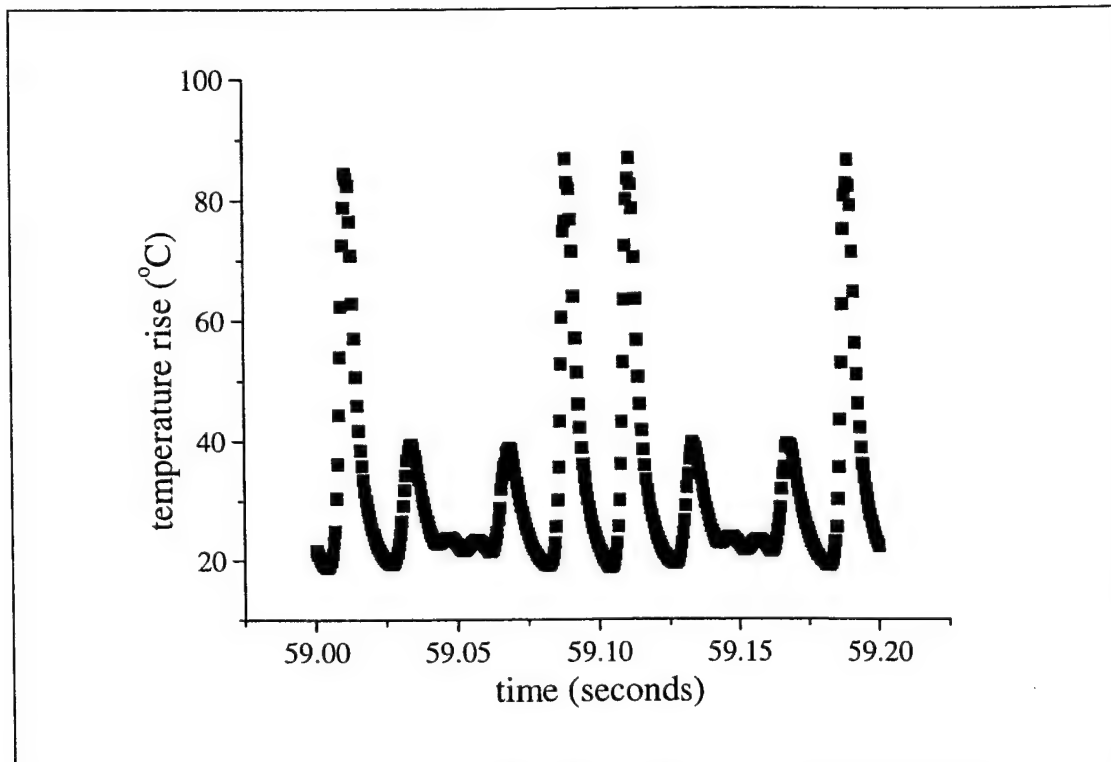


Fig. 5.6. Calculated surface temperature rises at center of the area scanned by a 488 nm laser beam. The substrate is assumed to be of an infinite thickness. Data points are the temperature rises at instants of 0.0005 second interval. Laser power is 4 W. The scanned area is an 1 mm x 1 mm square and the scanning frequencies are 40 and 50 Hz along the two dimensions of the square.

The final note of this section goes to the discussion on how to avoid occurrence of spikes of temperature rise induced by scanning laser beams. Assuming that a laser beam has the same probability to be anywhere within its scanning area, the fraction of time for which a point within the scanned area on the substrate surface receives laser irradiation is $\pi W^2/4A$, where W is the diameter of the laser beam on the substrate surface (0.4 mm in our experiment) and A the scanned area. Let the time for the laser beam to complete one scan be T_p . Then, the condition for suppression of temperature spikes is $\pi T_p W^2/4A \ll w^2/k$. For a 1 mm x 1 mm scanned area, the condition gives $T_p \ll 0.025$ second. So the frequencies of scanning lasers have to be hundreds of Hz in order that spikes of temperature rises are insignificant.

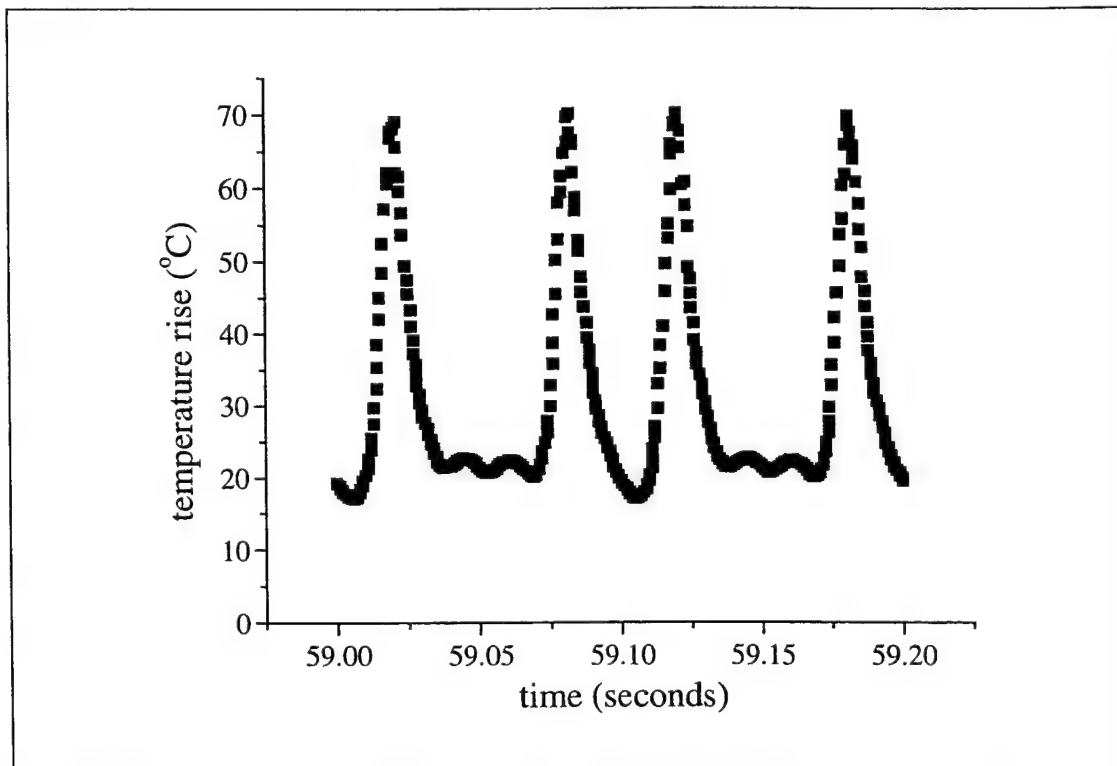


Fig. 5.7. Calculated surface temperature rises at center the area scanned by a 488 nm laser beam. The substrate is assumed to be of an infinite thickness. Data points are the temperature rises at instants of 0.0005 second interval. Laser power is 4 W. The scanned area is an 1 mm x 1 mm square and the scanning frequencies are 20 and 30 Hz along the two dimensions of the square.

5.4 Summary

The governing equation and boundary conditions for the heat-diffusion problem associated with laser irradiation of semiconductors have been examined. Expressions have been derived which, along with a numerical procedure developed here, enable us to compute laser-induced temperature rise efficiently. Calculations have been carried out to obtain surface temperature change on GaAs substrates that resulted from the scanning Ar^+ laser of our experiment setup. It has been found that the time scale for laser-induced temperature change is 10^{-3} seconds. Sensitivity tests have been done to see the effects of scanning frequencies and setting of location of the substrate thermal contact on the computed temperature rise. The model developed in this chapter for calculation of laser-induced temperature rise is deemed efficient and robust and can be used to couple with surface reaction models to assess the effects of laser heating on CBE growth and doping.

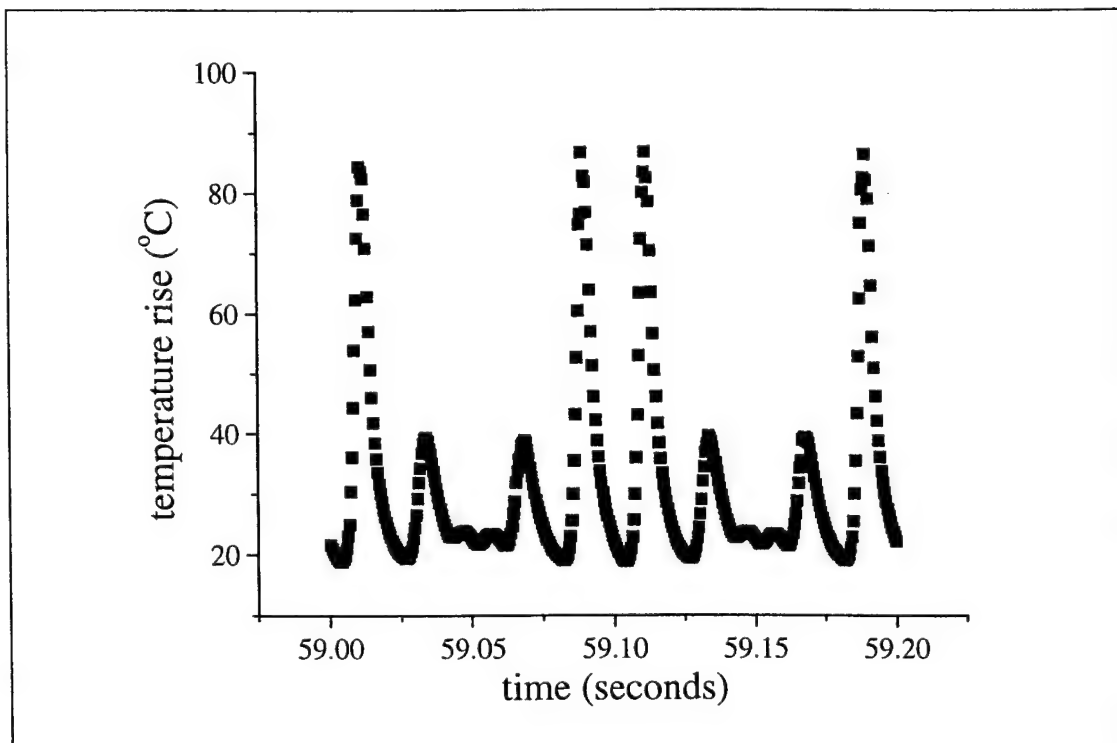


Fig. 5.8. Calculated surface temperature rises at center the area scanned by a 488 nm laser beam. The substrate is assumed to be 0.65 mm in thickness. Data points are the temperature rises at instants of 0.0005 second interval. Laser power is 4 W. The scanned area is an 1 mm x 1 mm square and the scanning frequencies are 40 and 50 Hz along the two dimensions of the square.

References

- [5.1] C. M. Wolfe, N. Holonyak, Jr. and G. E. Stillman, *Physical Properties of Semiconductors*, Prentice-Hall, Inc., Englewood Cliffs, New Jersey, Appendix A (1989).
- [5.2] H. K. Dong, *Ph. D Thesis*, University of California, San Diego (1995).
- [5.3] R. Haberman, *Elementary Applied Partial Differential Equations*, 2nd edition, Prentice-Hall, Inc., Englewood Cliffs, New Jersey, Chapter 1 and Chapter 10 (1987).
- [5.4] M. Lax, *J. Appl. Phys.* **48**, 3919 (1977).
- [5.5] H. E. Cline and T. R. Anthony, *J. Appl. Phys.* **48**, 3895 (1977).
- [5.6] Y. I. Nissim, A. Lietoila, R. B. Gold and J. F. Gibbons, *J. Appl. Phys.* **51**, 274 (1980).
- [5.7] J. A. McCaulley, V. R. McCrary and V. M. Donnelly, *J. Phys. Chem.* **93**, 1148-1158 (1989).
- [5.8] D. W. Winston, *User's Manual for SimWindows16 and SimWindows32*, Optoelectronics Computing Systems Center, University of Colorado, Boulder, Colorado (1996).
- [5.9] *IMSL Math/Library Online User's Guide*, Visual Numerics, Inc., Houston, Texas (1998).
- [5.10] *User Manual for CX 660 Scanner Control Amplifier*, General Scanning, Inc., Watertown, MA (1991).

CHAPTER 6

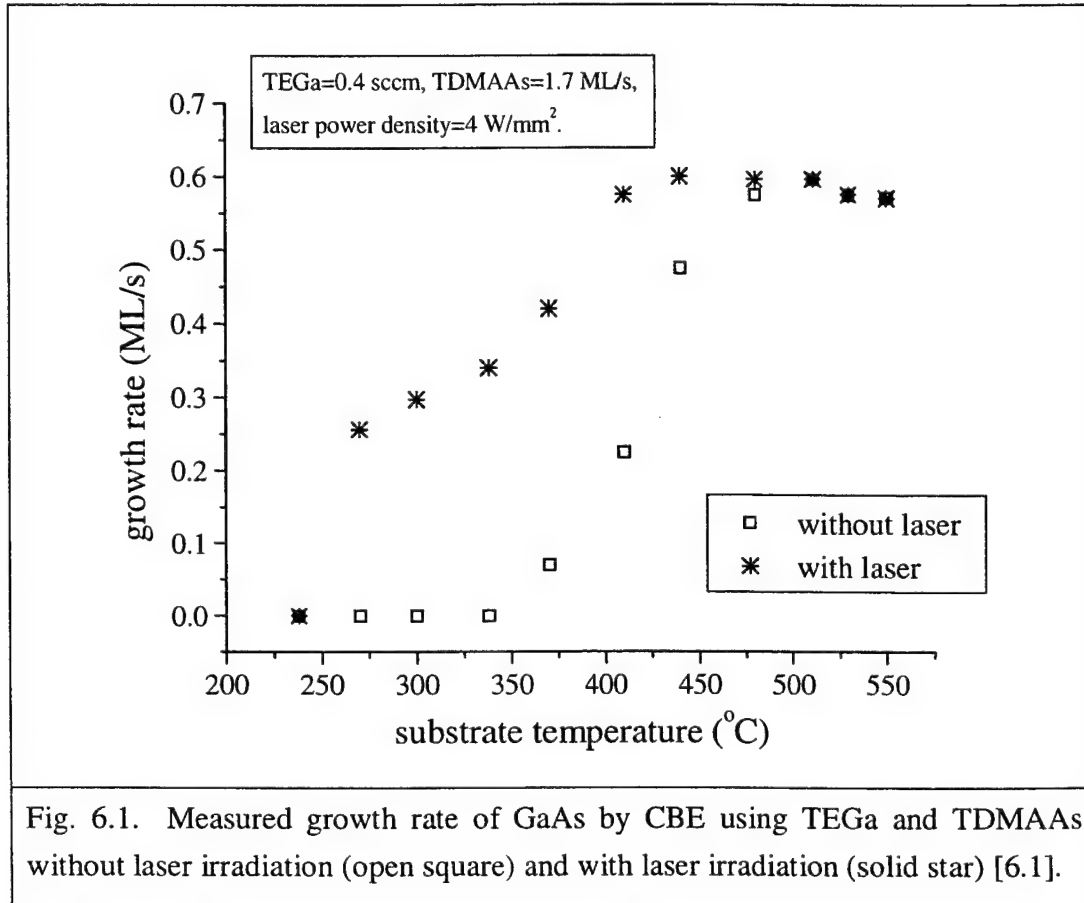
INVESTIGATIONS ON THE MECHANISMS RESPONSIBLE FOR Ar⁺-LASER INDUCED GAAS GROWTH ENHANCEMENTS

6.1 Introduction

Fig. 6.1 shows GaAs CBE growth-rate data collected using the Fig. 5.1 experimental setup [6.1] on GaAs substrates. The precursors used in the data collection were TEGa and TDMAAs. The TEGa and TDMAAs flow rates were 1.16ML/s and 1.7 ML/s, respectively. For the collection of laser-assisted growth rates, the output power of the Ar⁺ laser of Fig. 5.1 was set at 4 W and the laser beam scanned over an 1 mm x 1 mm substrate surface area for each data point. The scanning frequencies of the two galvanometers of Fig. 5.1 were 40 Hz and 50 Hz. The growth-rate data of Fig. 6.1 without laser irradiation were derived from RHEED intensity oscillations, while those with laser irradiation from post-growth surface profile measurement using a Dektak stylus profiler. We can see that while the normal growth ceased at around 340 °C, there was growth observed even at 238 °C substrate temperature with laser irradiation. An interferometry measurement [6.2] showed that the laser-induced substrate temperature rise with the laser irradiation conditions of Fig. 6.1 and the experimental setup of Fig. 5.1 was about 25 °C. It is clear that the observed growth-rate enhancements that resulted from laser irradiation cannot be explained with consideration of the temperature rise alone. Furthermore, no dependence of the growth-enhancement on the substrate type (n, p or semi-insulating) was found [6.2]. Investigations on the mechanisms responsible for the observed Ar⁺-laser induced growth enhancements are reported in this chapter.

As discussed in the introduction section of Chapter 5, an adsorbed molecule on a substrate in thermal equilibrium with the substrate surface can acquire thermal energy through its interactions with the substrate lattice. The probability that the molecule acquires enough thermal energy to activate its decomposition processes depends on the substrate temperature. The higher the substrate temperature, the more likely its decomposition can be activated. We shall, therefore, first investigate effects of the Ar⁺-

laser-induced temperature rise (that is, laser-induced pyrolytic effects) on the growth rate using the models for surface physics and chemistry developed in previous chapters.



Since decomposition of metalorganic species on a clean substrate surface can involve dangling bonds of the surface, it is usually true that the activation energy of a decomposition reaction on a clean substrate surface is different from that in the gas-phase. This is because dangling bonds of the surface can interact with electrons of an adsorbed molecule and facilitate its bond-breaking processes. It is therefore evident that surface decomposition-reaction rates are dependent on the concentration of holes (dangling bonds) of the surface. Excess carriers within a semiconductor which resulted from laser irradiation of the semiconductor can be transported to the surface and, thus, may alter the surface hole concentration. In this chapter, the surface concentrations of

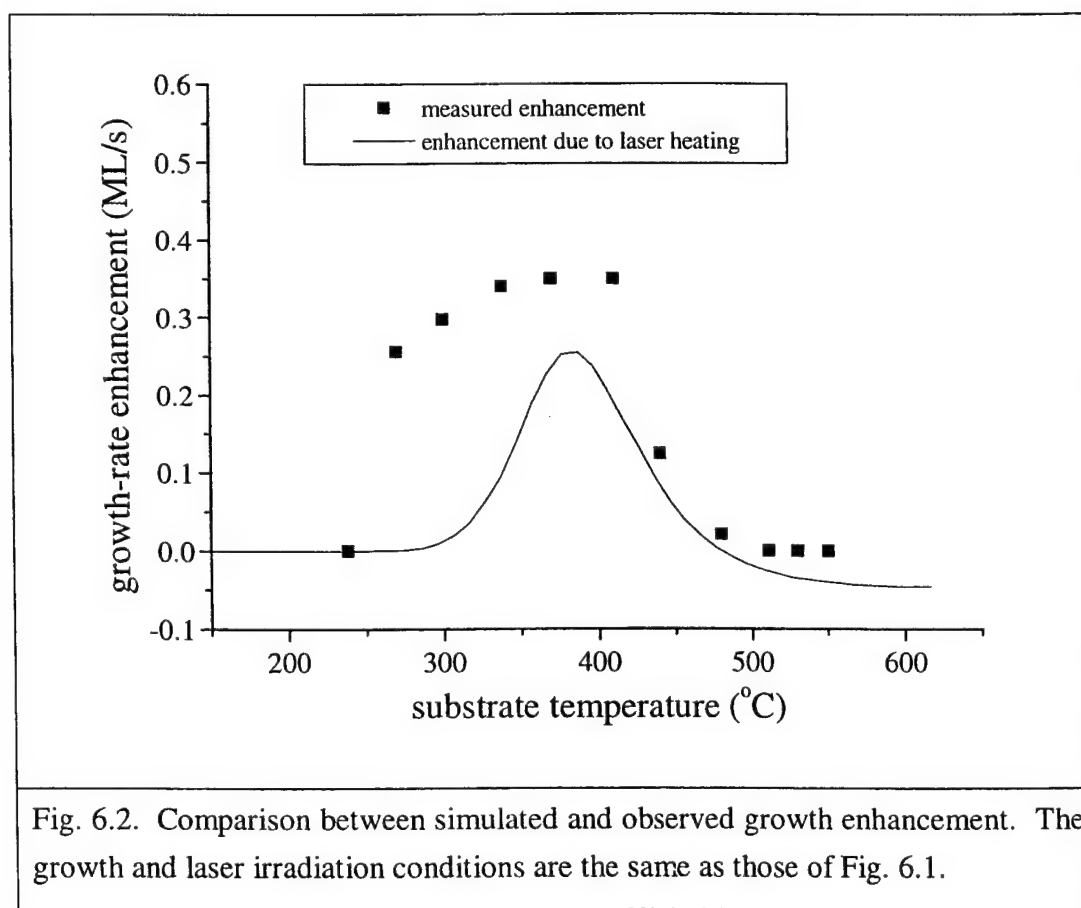
excess carriers are evaluated to assess changes in the tendency of metalorganic species undergoing catalytic reactions.

An adsorbed molecule can also acquire activation energies for its decomposition through absorption of photons with presence of laser irradiation. Laser-induced photodecomposition of metalorganic species (that is, laser-induced photolytic effects) will also be investigated in this chapter. Concentrations of precursors in physisorption and chemisorption states will be calculated. Likely photochemical pathways will be postulated.

6.2 Simulation of Ar⁺-laser-induced pyrolytic effects

Calculations of laser-induced temperature rises in Chapter 5 reveal that with an Ar⁺ laser scanning in the way, as specified for obtaining laser-assisted growth data of Fig. 6.1, there exist momentary spikes of surface temperature rise as large as 90 °C. Since the reaction model presented in Chapter 4 solves time-dependent differential equations of the surface reaction system for growth with TEGa and TDMAAs, it can be used to simulate GaAs growth of transient surface temperatures. Fig. 6.2 shows growth enhancements at the center of the scanned area from simulations with the reaction model of Chapter 4 and the temperature-rise model of Chapter 5 coupled together under the growth and laser irradiation conditions of Fig. 6.1. Also plotted in Fig. 6.2 are measured growth-enhancement data of Fig. 6.1 which are the differences between growth rates from laser-assisted growth and those from normal growth. The TEGa flux input used in the simulations is 1.16 ML/s corresponding to 0.4 sccm flow, since it is determined in Chapter 4 that 0.5 sccm of TEGa gives 1.45 ML/s absolute incident flux. The growth enhancement in Fig. 6.2 is shown as a function of the substrate temperature for normal growth. In Chapter 5, we concluded that to numerically investigate the heating effect of the scanning Ar⁺-laser of our experimental setup on surface reaction dynamics, the time step would have to be much less than 10⁻³ seconds. The simulated growth enhancement in Fig. 6.2 is an average over a period of 0.4 seconds with the laser at a new location of the scanned area every 10⁻⁴ second starting with 0.5x10⁻⁴ seconds into the irradiation. The

temperature rise at the center of the laser scanned area is computed every 10^{-4} second. The substrate temperature for normal growth is used to calculate the physical properties of GaAs needed for the temperature-rise model. Once the surface temperature rise at the center of the scanned area is computed, the surface reaction dynamic system of Chapter 4 is then allowed to proceed for 10^{-4} seconds at the temperature equal to the summation of the temperature rise and the substrate temperature for normal growth. The steady-state surface coverage from simulation of normal growth at a temperature 20 °C higher than the substrate temperature is used as the initial condition for the simulation of laser-assisted growth. We can see from Fig. 6.2 that consideration of laser-induced pyrolytic effects alone can not explain well the observed growth enhancement. In particular, the observed growth enhancements at the low temperature end of the observed growth-enhancement temperature window are not reproduced at all.

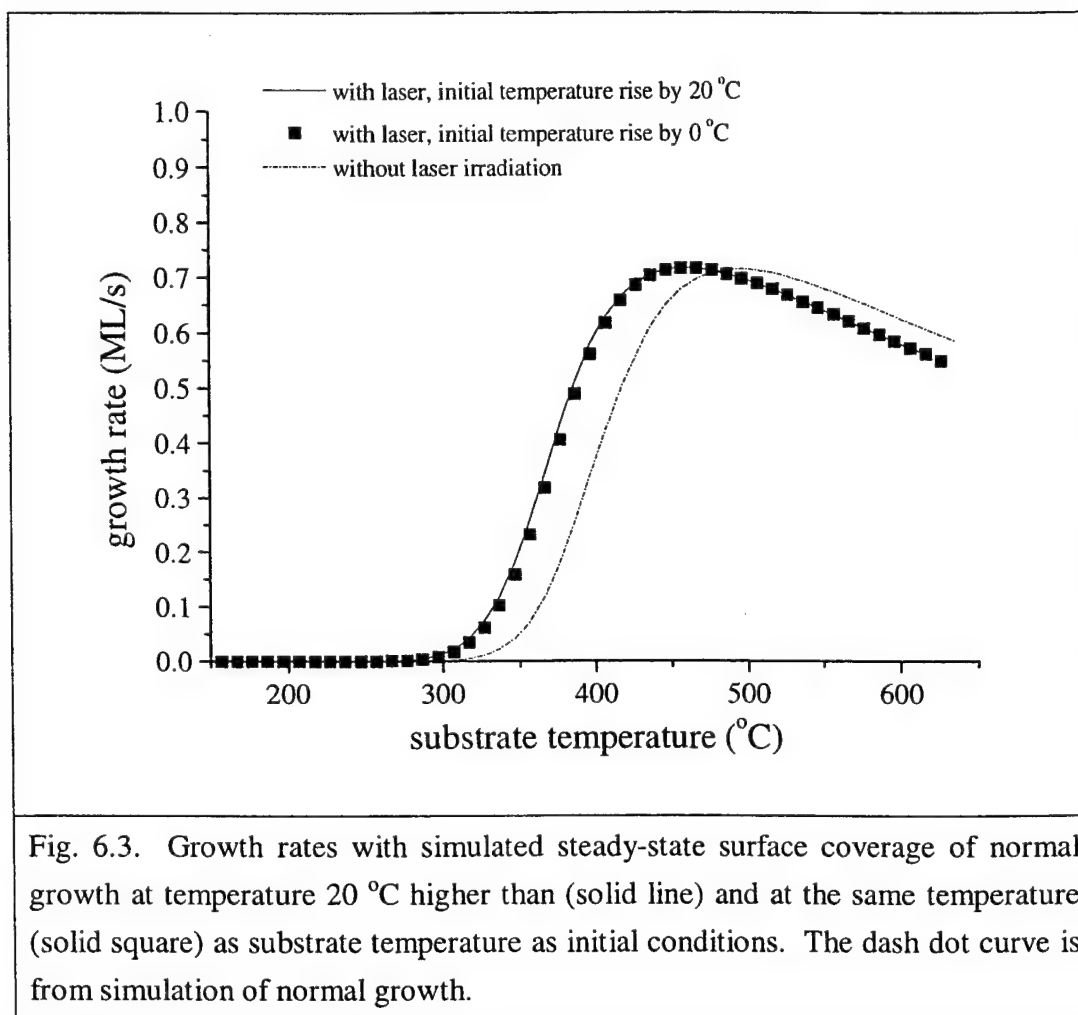


In the simulations of laser-assisted growth of Fig. 6.2, the initial condition used is the steady-state coverage of surface species from simulation of normal growth at a temperature 20 °C higher than the substrate temperature. This simulation practice is based on the consideration that 0.4 second of laser irradiation may not be sufficiently long for taking into account the average temperature rise due to laser irradiation. Only 0.4-second simulation of laser-assisted growth is performed because the simulation time step for laser-assisted growth has to be very small (10^{-4} seconds). To test the sensitivity of simulation results to the initial condition setting, simulation runs are carried out with steady-state surface coverage from normal growth at the substrate temperatures being used as initial conditions. Fig. 6.3 plots results from these simulation runs together with simulated growth rates of Fig. 6.2 and normal growth rates. We can see that the sensitivity of simulation of laser-assisted growth to the initial condition is very small because of the fact that upon being subject to laser irradiation, the surface temperature rises quickly. We can also see that the curves from laser-assisted growth can be approximately reproduced by moving the curve from normal growth toward the low-temperature direction by about 30 °C, which is the average temperature rise as revealed in the analyses of Chapter 5. Effects of momentary temperature spikes, therefore, have negligible effects on the growth enhancement. This can be understood by considering the reaction time scale of the surface reaction system discussed in Chapter 4 (Fig. 4.7). The time scale is longer than 15 seconds at temperatures lower than 300 °C and is, thus, much larger than the duration of momentary temperature rise. The surface reaction system simply does not respond to very short pulses of temperature rise.

6.3 Evaluation of laser-enhanced catalytic effects

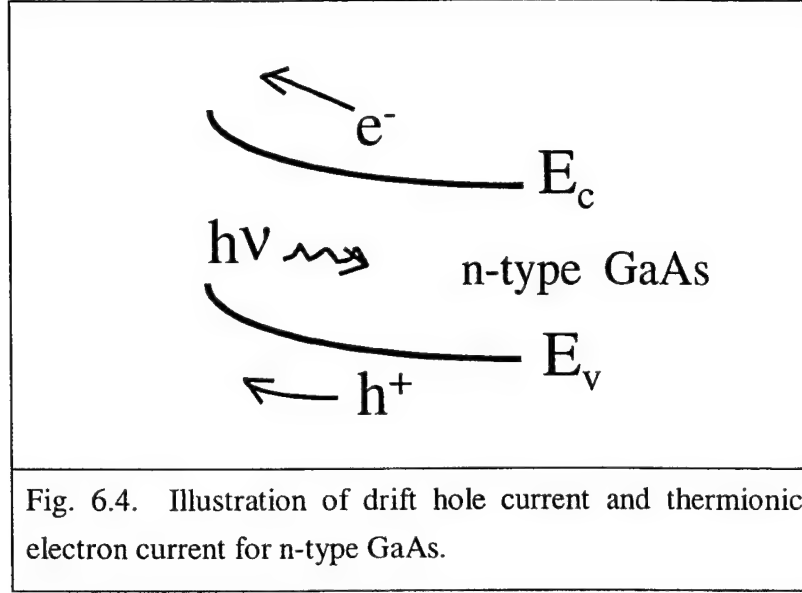
Since surface decomposition of chemical species in epitaxial processes involves surface dangling bonds, it is necessary for us to consider effects of carriers generated as byproducts of Ar^+ -laser irradiation of a GaAs substrate on the dangling-bond concentration of the GaAs surface. Carriers can move to the surface as drift, diffusion

and thermionic currents. While photogenerated minority carriers move to the GaAs surface mainly through drift motion (hole movement in the case of an n-type GaAs as illustrated in Fig. 6.4), thermionic emission of majority carriers (electrons in Fig. 6.4) from the bulk to the surface is also enhanced with concurrent presence of a photo-voltage resulted from the irradiation.



Since chemisorption of metalorganic species on a semiconductor surface is through formation of covalent bonds with the surface, it is intuitively correct for us to assume that chemisorbed species do not inject carriers into the semiconductor and thus, the total current at the surface is zero. Assuming that all photogenerated carriers

dissipate through recombination at the surface, the steady-state maximum excess-carrier concentrations at the surface, $\delta n(0)$ and $\delta p(0)$, can be estimated using



$$S_n \delta n(0) = S_p \delta p(0) = (1-R)I_{\max}, \quad (6.1)$$

where S_n and S_p are surface recombination velocities of electrons and holes, respectively [6.3], and R the reflectivity of the GaAs surface at 488 nm wavelength and I_{\max} the maximum incident flux of 488-nm photons. For an Ar^+ -laser beam of Gaussian intensity distribution, 400 μm in diameter and 4 W total power, the maximum incident flux is $1.4 \times 10^{22} \text{ cm}^{-2} \text{ s}^{-1}$. Approximately 53% of photons output by the laser impinge on the substrate surface in our experimental setup due to the imperfect reflectivity of the reflection mirrors and lens transmittance [6.2]. Hence, $I_{\max} = 7.4 \times 10^{21} \text{ cm}^{-2} \text{ s}^{-1}$. The typical value of S_n and S_p for GaAs is $\sim 10^6 \text{ cm/s}$ [6.4]. $R = 0.515$ [6.2]. Therefore, $\delta n(0)$ and $\delta p(0) \sim 5.9 \times 10^{15} \text{ cm}^{-3}$. By multiplying the concentration by $a/4$, where a is the lattice constant of GaAs ($a = 0.565325 \text{ nm}$), the maximum excess carrier concentration on the surface atomic plane is then $\sim 8.3 \times 10^7 \text{ cm}^{-2}$, which is much less than $6.3 \times 10^{14} \text{ cm}^{-2}$, the GaAs(100) surface dangling-bond concentration. Thus, Ar^+ -laser enhanced catalytic

effects on reaction dynamics of GaAs growth should be negligible under the experimental conditions used in this study.

6.4 Investigation on Ar⁺-laser-induced photolytic effects

In this section, laser-induced photolytic effects will be considered. Since photo-decomposition rates must be dependent on the concentrations of species involved, concentrations of precursors having access to photons provided in laser-assisted growth will be calculated as a function of the substrate temperature based on principles of chemical physics. Attempts will be made to correlate temperature dependency of the calculated concentration with the observed growth-enhancement temperature window of Fig. 6.1. When precursors impinge on a surface, both chemisorption and physisorption can occur [6.5]. Physisorption in the first adsorption layer is due to physical forces between molecules and surface atoms. Physisorption of a molecule in the second or higher layer results from interactions between the molecule and those molecules in the underneath layer. The forces between a singly adsorbed molecule and a molecule of the gas striking on top of it are small compared with the forces emanating from a condensed layer where all the molecules assist each other in attracting the one on top [6.6]. The formation of the first layer of sufficiently high surface density is, therefore, an essential condition for multi-layer adsorption. Chemisorption, on the other hand, occurs in the first adsorption layer only and is associated with chemical-bond formations between molecules and the surface. Because chemisorbed molecules on a surface are much strongly attached to the surface than physisorbed molecules, at elevated temperatures the first layer mainly consists of chemisorbed molecules as depicted in Fig. 6.5.

Estimation of concentrations of physisorbed molecules in the second layer is carried out by assuming that the first layer is almost complete and that the evaporation rate of a precursor of unity coverage in the second layer is equal to that of its bulk liquid. The Langmuir adsorption kinetics (Equation (2.1)) is used to formulate adsorption rates.

When the second layer is in a steady state, The law of mass conservation leads to, for the group-III species,

$$\alpha_{III} F_{III} (1 - \theta_{III} - \theta_V) = \alpha_{III} \frac{1}{4} V_{III}(T_s) \frac{P_{III} N_A}{RT_s} \theta_{III}, \quad (6.2)$$

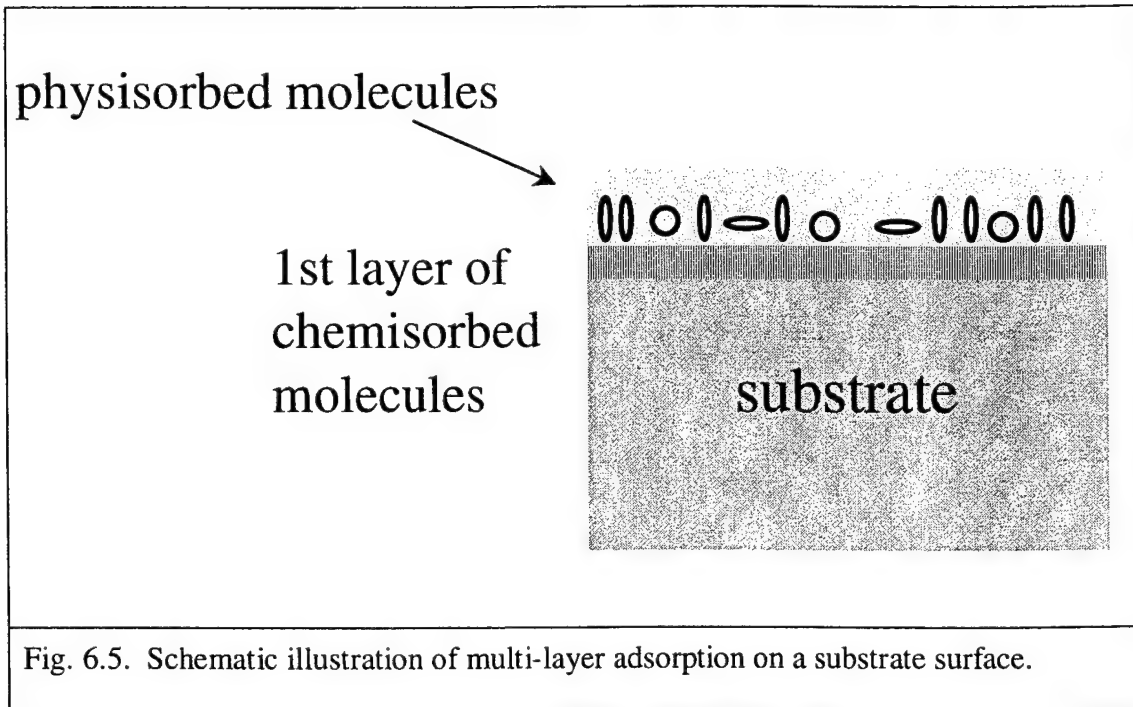


Fig. 6.5. Schematic illustration of multi-layer adsorption on a substrate surface.

and for the group-V species,

$$\alpha_V F_V (1 - \theta_{III} - \theta_V) = \alpha_V \frac{1}{4} V_V(T_s) \frac{P_V N_A}{RT_s} \theta_V \quad (6.3)$$

where α_{III} , F_{III} , θ_{III} , $V_{III}(T_s)$, P_{III} and α_V , F_V , θ_V , $V_V(T_s)$, P_V are condensation coefficients, absolute incident fluxes from the gas phase, coverage in the second layer, mean molecular speeds at the substrate temperature, equilibrium vapor pressures of group-III and group-V species, respectively, R the gas constant, N_A the Avogadro number and T_s

the substrate temperature. The mean speed of gas-phase molecules of molecular weight M at temperature T_s is given by

$$V(T_s) = \sqrt{\frac{RT_s}{2\pi M}} \quad (6.4)$$

Solving Equations (6.2) and (6.3) for θ_{III} and θ_V and using Equation (6.4), we can obtain

$$\theta_{III} = \frac{1}{1 + \frac{F_V}{F_{III}} \frac{P_{III}}{P_V} \sqrt{\frac{M_V}{M_{III}}} + \frac{P_{III} N_A}{F_{III} \sqrt{2RT_s \pi M_{III}}}} \quad (6.5)$$

and

$$\theta_V = \frac{1}{1 + \frac{F_{III}}{F_V} \frac{P_V}{P_{III}} \sqrt{\frac{M_{III}}{M_V}} + \frac{P_V N_A}{F_V \sqrt{2RT_s \pi M_V}}} \quad (6.6)$$

where M_{III} and M_V are molecular weights of group-III and group-V species, respectively. Table 6.1 lists incident fluxes and physical properties of TEGa and TDMAAs used in calculating their coverages under the growth conditions of Fig. 6.1.

Fig. 6.6 shows calculated coverage of TEGa and TDMAAs physisorbed in the second layer. We can see that the TEGa coverage is very small. In fact, if we require $I\sigma[\text{TEGa(ads)}] \sim 0.3$, where 0.3 is the observed growth enhancement in ML/s at 300 °C, $[\text{TEGa(ads)}]$ the surface coverage of TEGa in the second layer, σ the absorption cross section of TEGa and I the photon flux averaged over the scanned area, we can estimate the absorption cross section required for reproducing the growth enhancement. With $[\text{TEGa(ads)}] \sim 1 \times 10^{-10}$ ML and $I = 5.5 \times 10^{20} \text{ s}^{-1} \text{ cm}^{-2}$, the absorption cross section required is $\sigma \sim 5.5 \times 10^{-12} \text{ cm}^2$. On the other hand, McCrary and Donnelly [6.9] reported TEGa UV peak absorption cross sections of $9 \times 10^{-18} \text{ cm}^2$ and much smaller visible-wavelength

absorption cross sections. The required absorption cross sections for photo-decomposition of TEGa in the second layer to account for laser-induced growth enhancements are orders of magnitude larger than physically possible values. In addition, we see from Fig. 6.6 that variation of the TEGa coverage with substrate temperature exhibits no correlation with the variation of the observed growth enhancement of Fig. 6.2 with temperature. Therefore, it is very unlikely that photo-decomposition processes in the second adsorption layer contribute the observed laser-induced growth enhancement.

Table 6.1. Constants used in calculations of TEGa and TDMAs coverage in the second adsorption layer

constant	unit	TEGa	TDMAs
M	g/mole	156.91	206.92
F	ML/s	1.16	1.7
$\text{Log}_{10}(\text{P})$	Torr	$9.165-2530/T$	$8.31226-2399.6/T$

The references for $\text{Log}_{10}(\text{P})$ of TEGa and TDMAs are [6.7] and [6.8], respectively.

The growth model of Chapter 4 is for simulating surface adsorption and chemical reactions in the first layer of adsorbed molecules on GaAs(100) surfaces. Surface coverage in the first layer is the output of the model. We learn from Fig. 4.6 that in the first layer, the coverage of chemisorbed diethylgallium (DEGa) is much larger than that of physisorbed TEGa. This is consistent with our discussion above that at elevated temperatures the first adsorption layer consists mainly of chemisorbed molecules. With the presence of a scanning laser during growth, the surface coverage of DEGa varies with time because of surface-temperature fluctuations induced by the laser. With outputs from simulations of laser-assisted growth, the DEGa coverage during laser-assisted growth is

computed as a temporal average and an irradiation-density weighted temporal average. Specifically, for the temporal average of DEGa coverage,

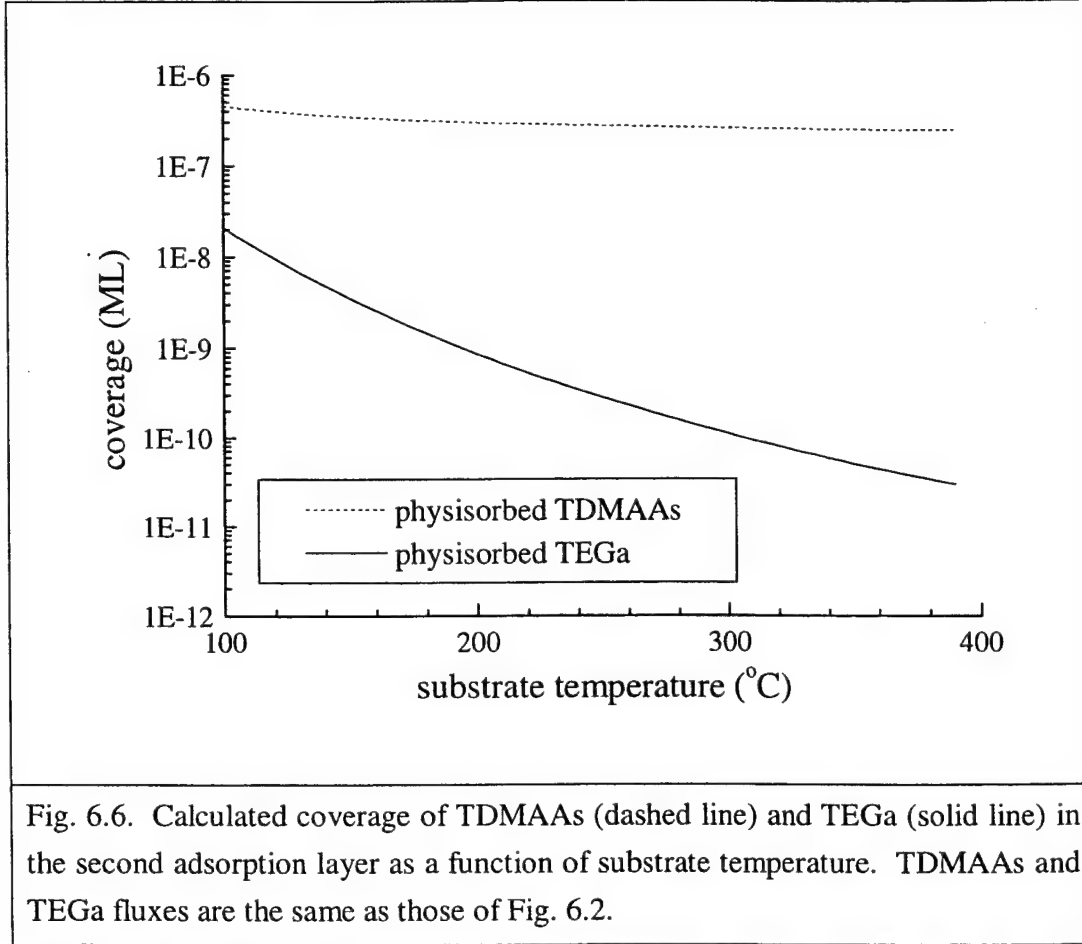


Fig. 6.6. Calculated coverage of TDMAAs (dashed line) and TEGa (solid line) in the second adsorption layer as a function of substrate temperature. TDMAAs and TEGa fluxes are the same as those of Fig. 6.2.

$$[\text{DEGa}] = \frac{\int_0^{\Delta T} \theta_{\text{DEGa}}(t) dt}{\Delta T}, \quad (6.7)$$

and for the irradiation-intensity weighted temporal average of DEGa coverage,

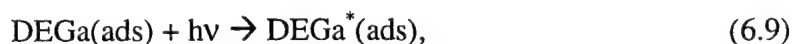
$$[\text{DEGa}] = \frac{(1-R) \int_0^{\Delta T} \theta_{\text{DEGa}}(t) I(t) dt}{\Delta T}, \quad (6.8)$$

where ΔT is the period for averaging, R the reflectivity of the GaAs surface with respect to 488-nm-wavelength light, θ_{DEGa} the simulated transient surface coverage of DEGa and I the transient laser-irradiation intensity in W/mm^2 at the center of the scanned area. Formula presented in Chapter 5 are used to simulate the irradiation density of the scanning laser in our experimental setup. A $(1-R)$ factor is included in Equation (6.8) because with the experimental conditions of Fig. 6.2, the average laser power over the scanned area happens to be approximately equal to $1/(1-R) \text{ W}/\text{mm}^2$. The procedures for simulation of laser-assisted growth are the same as those for producing Fig. 6.2. The left-hand sides of Equations (6.7) and (6.8) are calculated with $\Delta T = 0.4$ seconds, $dt = 10^{-4}$ seconds and $I(t)$ and $\theta_{\text{DEGa}}(t)$ being the simulated results at the end of each time step.

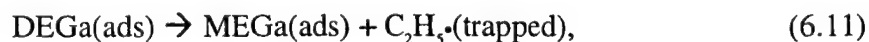
Fig. 6.7 plots the DEGa coverage computed using Equations (6.7) and (6.8). By comparing Fig. 6.7 with Fig. 6.2, we can see that the variation of DEGa surface coverage with substrate temperature correlates well with growth enhancements at the low temperature end of the growth enhancement temperature window. Especially, we notice that the temperature of the DEGa coverage peak coincides with the temperature ($\sim 300^\circ\text{C}$) at which the largest difference exists between the observed growth enhancement and the simulated growth enhancement with consideration of laser-induced pyrolytic effects alone. The observations strongly suggest that Ar^+ -laser induced growth enhancements are due to photodecomposition of chemisorbed TEGa decomposition products along with enhanced decomposition of surface metalorganic species associated with laser-induced temperature rises. The UV absorption spectrum [6.9] of gas-phase TEGa peaks at 213 nm, far away from the wavelength of the laser we used, but there have been reports in the literature on measurable absorption of adsorbed metalorganic films at visible wavelengths. Sugiura et al. [6.10] performed an experiment in which a 500-mW Ar^+ laser beam (400- μm diameter, 488 nm or 514.5 nm wavelength) was used to irradiate a quartz ampoule filled with TEGa molecules at a pressure of 10 Torr. White spots were observed on the inner wall of the ampoule at the points where the laser beam passed through the transparent ampoule. Their finding is consistent with the conclusion one tends to draw based on Figs. 6.2 and 6.7 that adsorbed TEGa or its decomposition products can undergo photodecomposition when being subject to Ar^+ -laser irradiation.

The DEGa surface coverage calculated using Equation (6.7) is approximately the same as that calculated using Equation (6.8). This is because, as discussed in Section 6.2, surface reactions of the precursors used here hardly respond to surface temperature fluctuations of very short periods because the reactions proceed relatively much more slowly at low growth temperatures.

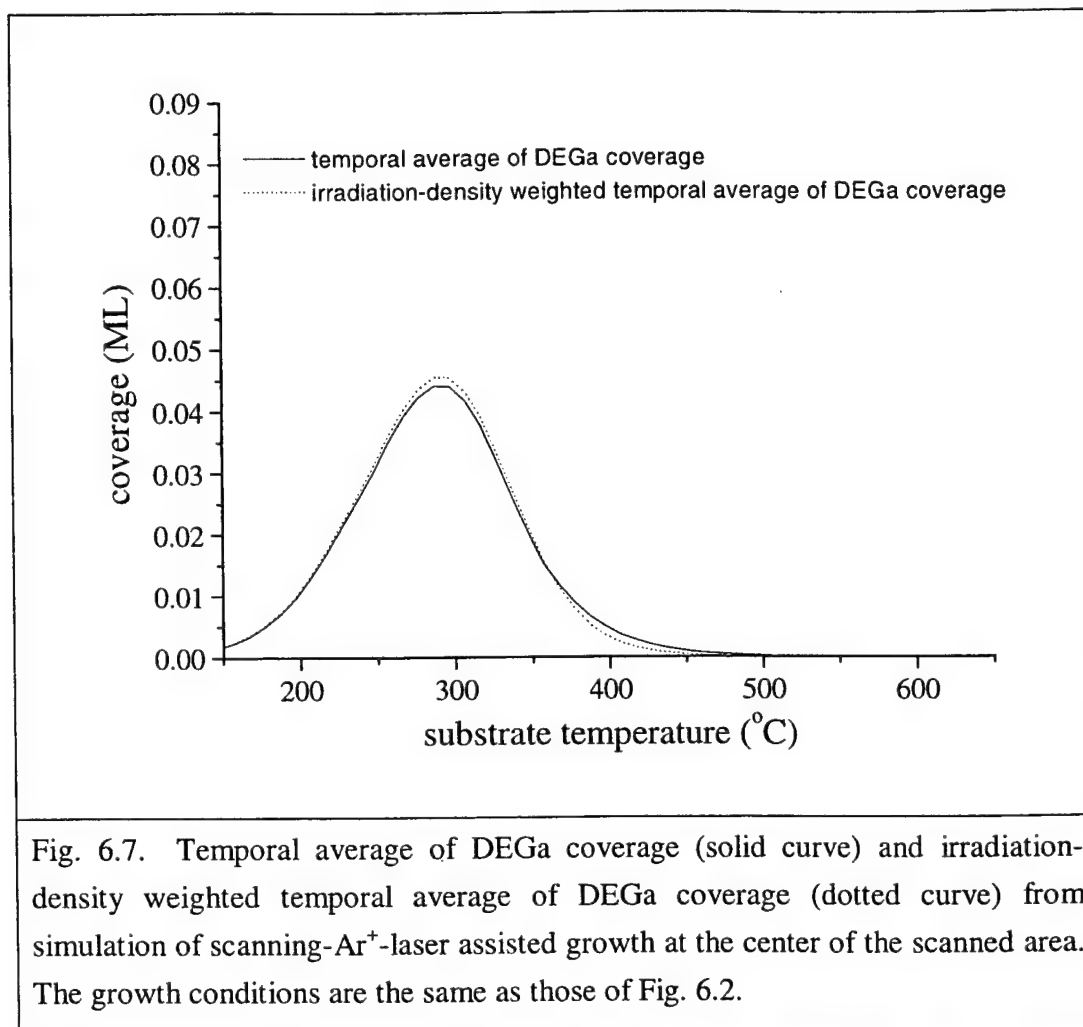
The mean Ga-C₂H₅ bond dissociation energy is 217-222 kJ/mole [6.11], while the energy of 488-nm photons is 245.5 kJ/mole. Therefore, photodecomposition reactions are, in principal, energetically accessible. The initial event in any photochemical process is the absorption of a photon by an atom, molecule, or complex ion, resulting in an electronically excited state [6.12]. If DEGa* represents a DEGa molecule in an excited state, the process can be written as the reaction,



where following the notation of the previous chapter, (ads) stands for being in the adsorption state. Based on findings from a systematic experimental study performed by Zhang and Stuke [6.13] on photochemistry of gaseous and surface adsorbed metalorganics, it is postulated here that DEGa*(ads) can undergo decomposition through both direct-bond-fission and β -hydrogen-elimination pathways:



where MEGa refers to a monoethylgallium radical, (g) the gas-phase state and (trapped) the state of being trapped on the surface. No surface-site involvement is assumed for Reactions (6.10) and (6.11) because at low substrate temperatures, the total steady-state coverage is almost unity (Fig. 4.6). The fate of the trapped ethyl radical from Reaction (6.11) may be complicated. It can react with adsorbed species on the surface, leave the surface or become adsorbed on the surface. The Ga-containing products from Reactions (6.10) and (6.11) can decompose further through the same reaction pathways and yield Ga atoms for growth.



It is a common assumption that adsorbed-phase absorption of light can be attributed to the same electronic processes as those in the gas phase. To estimate the absorption cross section required to reproduce the observed growth enhancement, a similar calculation to that performed for TEGa physisorbed in the second layer can be done, that is, by imposing $I\sigma[\text{DEGa(ads)}] \sim 0.3$ with the assumption that the decomposition quantum yield of $\text{DEGa}^*(\text{ads})$ is unity. With $[\text{DEGa(ads)}] \sim 0.045 \text{ ML}$ and $I = 5.5 \times 10^{20} \text{ s}^{-1} \text{ cm}^{-2}$, $\sigma \sim 1.2 \times 10^{-20} \text{ cm}^2$. Such a small visible-wavelength absorption cross-section value is consistent with the TEGa gas-phase absorption spectra reported by McCrary and Donnelly [6.9].

For discussion of the processes controlling the growth-enhancement temperature window, Fig. 6.8 displays temporal averages (Equation (6.7)) of surface coverages of DEGa and group-V related species from simulations of laser-assisted growth for producing data of Fig. 6.7. We first note that the maximum surface coverage is one and that group-V related species dominate at low substrate temperatures. We also see in Fig. 6.8 that the rise of DEGa coverage at temperatures lower than 300 °C corresponds to the fall in the coverage of group-V related species. This means that group-V related species inhibit building-up of Ga-containing species on the surface by blocking surface sites available for adsorption and dissociative chemisorption of TEGa.

6.5 Summary

The pyrolytic effect of Ar⁺-laser irradiation on CBE of GaAs with TEGa and TDMAs as precursors has been evaluated quantitatively using the models developed in previous chapters. Numerical simulations taking the pyrolytic effect into account alone can not reproduce the observed growth-rate enhancements. Procedures have been established for examining catalytic and photolytic effects of laser irradiation on epitaxial growth. Calculation of photo-induced surface excess carrier concentrations corresponding to our experimental conditions reveals that the catalytic effect should be negligible. Amount of precursors in the first and second adsorption layers has been looked into quantitatively. It is concluded that photodecomposition of chemisorbed TEGa decomposition products, along with laser-induced temperature rise, is responsible for observed Ar⁺-laser induced growth enhancements. Likely, photodecomposition reactions have also been postulated. Group-V species have been found to control the growth-enhancement temperature window because of their site-blocking effects.

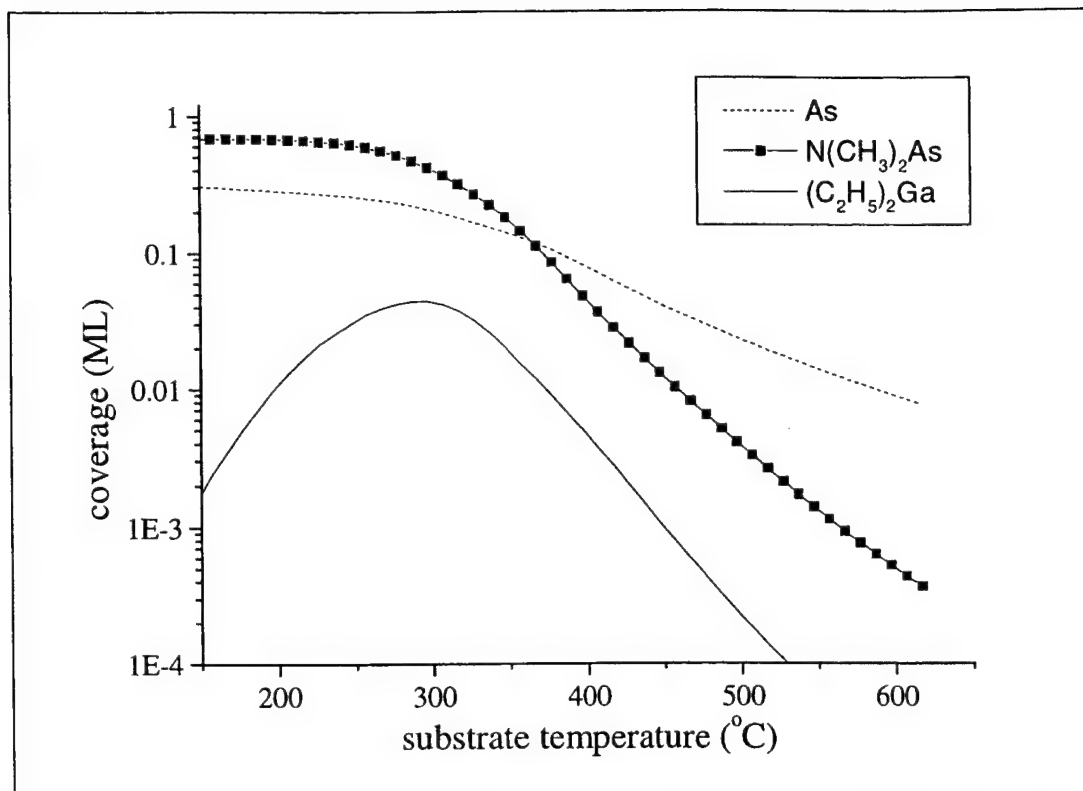


Fig. 6.8. Temporal averages of surface coverages of arsenic (dotted line), mono(dimethylamino)arsenic (solid line+square) and diethylgallium (solid line) as a function of substrate temperature from simulation of laser-assisted growth. TDMAAs and TEGa fluxes are the same as those of Fig. 6.2.

References

- [6.1] H. K. Dong, N. Y. Li and C. W. Tu, in *Proc. 21st Int. Symp. Comp. Semicond.*, 69 (1995).
- [6.2] H. K. Dong, *Ph. D Thesis*, University of California, San Diego (1995).
- [6.3] C. M. Wolfe, N. Holonyak, Jr. and G. E. Stillman, *Physical Properties of Semiconductors*, Prentice-Hall, Inc., Englewood Cliffs, New Jersey, Section 8.3.3 (1989).
- [6.4] Z. P. Yu, and R. W. Dutton, *A Generalized Electronic Material Device Analysis Program*, Stanford University, Stanford, California, page 62 (1985).
- [6.5] R. P. H. Gasser, *An introduction to chemisorption and catalysis by metals*, Clarendon Press, Oxford, Chapter 1 (1985).
- [6.6] J.H. de Boer, *The Dynamical Character of Adsorption*, 2nd Edition, Oxford at the Clarendon Press, Chapter IX (1968).
- [6.7] *Catalog of Organometallics for the Electronics Industry*, Air Products and Chemicals, Inc., Allentown, PA (1996).
- [6.8] Private communication with Dr. Ravi Kanjolia of Epichem Inc., Allentown, PA (1999).
- [6.9] V. R. McCrary and V. M. Donnelly, *J. Cryst. Growth* **84**, 253-258 (1987).
- [6.10] H. Sugiura, T. Yamada and R. Iga, *Jpn. J. of Appl. Phys.* **29**(1), L1-L3 (1990).
- [6.11] M. C. Paputa and S. J. W. Price, *Can. J. Chem.* **57**, 3178 (1979).
- [6.12] O. Horvath and K. L. Stevenson, *ChargeTransfer Photochemistry of Coordination Compounds*, VCH, New York, Chapter 2 (1993).
- [6.13] Y. Zhang and M. Stuke, *J. Cryst. Growth* **93**, 143-150 (1988).

CHAPTER 7

MODELING STUDY OF SILICON INCORPORATION FROM SiBr_4 IN GaAs LAYERS GROWN BY CHEMICAL BEAM EPITAXY

7.1 Introduction

Silicon is the preferred n-type dopant for InP- and GaAs-based device structures due to its low thermal diffusivity and the absence of any surface segregation and memory effect during epitaxial growth. While the use of elemental Si in a standard effusion cell has proven effective for Si doping in gas source molecular beam epitaxy, this method is incompatible with chemical beam epitaxy (CBE) due to the formation of a passivating "crust" of C and SiC on the hot Si surface in the presence of metalorganic by-products [7.1]. The formation of this crust reduces the doping efficiency of the effusion cell. Extensive studies, therefore, have been carried out by epitaxy researchers on gaseous Si-containing precursors as doping alternatives [7.2-7.4]. It has been demonstrated that silicon tetrabromide (SiBr_4) can be used as a high-efficiency vapor source under CBE growth temperatures (400 - 600 °C) for the controlled incorporation of electrically active silicon into InP- and GaAs-based device structures [7.2-7.4]. In addition, the net electron concentration and mobility of the samples grown with SiBr_4 are comparable to those obtainable with elemental Si or Sn [7.2]. Since it is known that the efficiency of carbon incorporation with halomethanes correlates to bond strengths in halomethanes [7.5], the high doping efficiency of SiBr_4 has been attributed to the relatively weaker Br-SiBr₃ bond strength (87.9 kcal/mole) [7.4].

Growth and doping mechanism studies performed in a CBE environment have direct relevance to metalorganic vapor phase epitaxy (MOVPE), since MOVPE is materialized through gas-phase and surface decomposition of gaseous species. Silane (SiH_4) is an important n-type dopant precursor in MOVPE because of its purity and convenience and high growth temperatures used in MOVPE. In CBE, however, SiH_4 requires precracking to be utilized efficiently. In a study carried out by Bass [7.6] on silicon doping of GaAs by MOVPE, he found that the incorporation of silicon from silane

was not governed by the gallium vacancy concentration of the lattice, but by a surface kinetic process. Redwing et al.'s MOVPE studies [7.7] on silicon incorporation from silane revealed that Si doping was limited by surface heterogeneous chemistry regardless of whether arsine or tertiarybutylarsine (TBA) was used as the group-V precursor, since they found that the doping level was independent of the gas residence time of their reactor.

In this chapter, we derive an analytical expression for calculating the Si concentration from SiBr_4 doping under CBE growth conditions. The process of analyses and derivation process enables us to discuss whether the high doping efficiency of SiBr_4 may also be owing to its large molecular weight (348). The expression derived is applied to the case of CBE of GaAs with triethylgallium (TEGa) and tris(dimethylamino) arsine (TDMAs) because the numerical model developed in Chapter 4 [7.8] for the growth process can provide the surface coverage and growth rate needed in the doping calculation. Theoretical predictions of doping concentrations are compared with experimental values. Very good agreement seen in the comparison provides support for the analyses and derivation. Incorporation of the analytical expression into the growth model results in a predictive tool which improves our efficiency in the process of trial growth for obtaining a desired doping concentration and growth rate. On the basis of analyses in this study, discussions are also extended to factors which may cause variation of the Si incorporation rate from SiH_4 in MOVPE with the substrate temperature and the type of group-V precursor used.

7.2 Experimental methods

All of the SiBr_4 -doped GaAs epitaxial layers for comparison with the theoretical prediction were grown in a Perkin Elemer 425 MBE system, equipped with gas lines for metalorganic species and a 1600 l/s turbomolecular pump. High-purity (99.999%) SiBr_4 without any carrier gas was delivered into the growth chamber through an ultra-high vacuum leak valve. The vapor pressure immediately upstream of the leak valve was

sensed by a Baratron pressure sensor. The sensor signal was fed back to a mass flow controller (MFC) downstream of the SiBr_4 bubbler. The vapor pressure at the leak valve could be, therefore, maintained constant (0.1 Torr in this study). TEGa was injected into the chamber directly using an MFC downstream of the TEGa bubbler. TDMAAs was carried by purified H_2 gas into the chamber, while the flow rate of H_2 gas into the TDMAAs bubbler was adjusted with an MFC upstream of the TDMAAs bubbler.

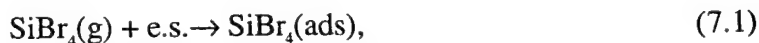
All epitaxial layers were grown on semi-insulating epi-ready GaAs(100) substrates which were In soldered to 3-inch-diameter silicon wafers. Substrate temperatures were measured using an infrared optical pyrometer which was calibrated by observing the appearance of 4x reflection high-energy-electron diffraction (RHEED) surface reconstruction patterns of a substrate upon thermal desorption of surface oxides at 580 °C. Net electron concentrations were determined using the van der Pauw-Hall technique on cleaved 5x5 mm² samples with In contacts. Samples whose electrical data exhibited the amphoteric behavior of Si at high doping levels were not used for comparison between theory and measurement. Since the absolute TDMAAs flux incident on the substrate is governed by the nonlinear fluid dynamics of H_2 gas and TDMAAs fluid in the bubbler, we determined the TDMAAs absolute incident flux in terms of monolayers per second (ML/s) through group-V induced RHEED intensity oscillations at a substrate temperature in between 420 °C and 470 °C (Chapter 4). The V/III incorporation ratio varied from 1.4 to 2.0, and 1.6 was a value determined to be optimal for growth [7.4].

In our system, the rate of SiBr_4 effusion through the SiBr_4 leak valve can be assumed to be $0.25\bar{v}cA$, where \bar{v} is the mean speed of SiBr_4 molecules at room temperature and c the SiBr_4 concentration on the upstream side of the leak valve and A the area of the leak valve. Based on this assumption, the effusion rate should be linearly proportional to the product of the upstream pressure and the leak valve setting. The linearity of doping concentration with the leak valve setting at a fixed upstream pressure in our system was demonstrated by Li et al. [7.9] for the case of Cl_2H_2 as a p-type dopant. Since the TDMAAs and SiBr_4 injectors are of the same geometrical configuration inside the growth chamber in our system, we can utilize information on the TDMAAs absolute

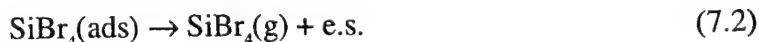
incident flux to estimate the SiBr_4 absolute incident flux (ML/s) on the substrate. Inside an ultra-high vacuum, molecules hit a pump inlet in a line-of-sight fashion. Assuming that all molecules hit the turbo molecular pump of our system are trapped irreversibly, we can equate the injection rate (molecules per seconds) of a species to $0.25SA_0P_{ss}\bar{v}/RT$, where P_{ss} is the steady state chamber pressure established with a continuous injection of the species, S the effective inlet area of the pump, A_0 the Avogadro constant, R the gas constant and T the temperature. With the TDMAAs flux being 0.28 ML/s as determined by the method outlined above, $P_{ss} = 1.5 \times 10^{-5}$ Torr at room temperature. While with the SiBr_4 upstream pressure and leak valve set at 0.1 Torr and 80 respectively, $P_{ss} = 1 \times 10^{-6}$ Torr at room temperature. Taking into account the difference in molecular weights of SiBr_4 and TDMAAs, we find that the SiBr_4 absolute incident flux is 0.014 ML/s with the SiBr_4 injection settings. The P_{ss} values given here are readouts from a cold-cathode pressure gauge. The assumption implied in the calculation is that with TDMAAs and SiBr_4 concentrations inside the chamber being the same, the pressure gauge would also give the same readout.

7.3 Analyses of Si incorporation from SiBr_4

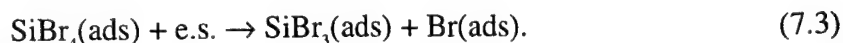
SiBr_4 is assumed to adsorb as an intact precursor,



where e.s. is an empty surface site where adsorption and reactions can occur. The precursor $\text{SiBr}_4(\text{ads})$ can reversibly desorb,



The first decomposition step toward Si incorporation is further assumed to be



The sequence of reactions leading to decomposition assumed here for SiBr_4 is similar to those proposed for decomposition on semiconductor surfaces of other CBE species such as TEGa [7.10], TDMAAs [7.11] and halomethanes [7.5]. The necessity of including adsorbed intact precursors is due to the fact that surface residence time of large molecules is significant (see discussion later). Bass [7.6] observed in an MOVPE reactor that allowing silane to flow briefly before growth of GaAs resulted in a carrier concentration spike at the substrate-epitaxial layer interface even if the substrate was annealed for an extensive period of time at the growth temperature before growth was started. Shogen et al. [7.12] found that the Ga-Si binding energy was 2 eV per bond, or 193 kJ/mole. We therefore assume that thermal desorption of chemisorbed SiBr_3 radicals from the surface is relatively slow at CBE growth temperatures. Further efficient decomposition of $\text{SiBr}_3(\text{ads})$ may be either through Br transfer to the surface like Reaction (7.3) or through SiBr_3 reactions with As or H radicals on the surface. It is also possible that a chemisorbed SiBr_3 may recombine with a chemisorbed Br atom and leave the surface through Reaction (7.2). We can assume, however, with consideration of the abundance of adsorbed As atoms and empty surface sites at growth temperatures, that the recombination rate is relatively slow. With all the arguments presented, the silicon incorporation rate can be approximated as the rate of Reaction (7.3). Therefore the doping concentration n can be calculated using $n = R_3/R_g$, where R_g is the epitaxial growth rate and R_3 the rate of Reaction (7.3).

When $n = 10^{18} \text{ cm}^{-3}$ and $R_g = 1 \text{ ML/s}$, $R_3 = 2.8 \times 10^{10} \text{ cm}^{-2} \text{ s}^{-1}$, while the SiBr_4 incident flux equivalent to 0.014 ML/s is $\sim 9.1 \times 10^{12} \text{ cm}^{-2} \text{ s}^{-1}$. Therefore at typical CBE growth conditions and doping levels, the rate of Reaction (7.3) should be relatively slow in comparison to the incident flux, and the $\text{SiBr}_4(\text{ads})$ concentration is essentially not affected by Reaction (7.3). At steady state, the $\text{SiBr}_4(\text{ads})$ concentration can thus be determined from a balance between rates of Reactions (7.1) and (7.2). We describe the initial adsorption of SiBr_4 (Reaction (7.1)) using the Langmuir kinetics, i.e., $R_1 = FN_s(1-\theta)$, where F is the absolute incident flux, θ the total surface coverage by adsorbed molecules and N_s the atom area density on a (100) plane of Ga or As atoms. Denoting the $\text{SiBr}_4(\text{ads})$ concentration as σ , we can formulate the rate of Reaction (7.2) as $R_2 = \sigma v_0 \exp(-Q/RT)$, where v_0 is the oscillation frequency of SiBr_4 in the adsorbed state,

referring especially to vibrations perpendicular to the surface, and Q the adsorption heat [7.13]. The steady-state σ during growth can then be expressed as

$$\sigma = FN_s(1-\theta)\tau_0\exp(Q/RT) \quad (7.4)$$

where $\tau_0 = 1/\nu_0$. The concentration of empty surface sites is $N_s(1-\theta)$. With E_a being the activation energy of Reaction (7.3), $R_g = A_3\sigma N_s(1-\theta)\exp(-E_a/RT)$, where A_3 is the pre-exponential factor of the Arrhenius expression. The expression for the doping concentration is

$$n = A_3FN_s^2(1-\theta)^2\tau_0\exp[-(E_a-Q)/RT]/R_g. \quad (7.5)$$

Let V_l be the mean surface translational speed of adsorbed SiBr_4 molecules and ν be the stretching frequency of the Si-Br bond in a SiBr_4 molecule. The number of stretching vibrations Br atoms make while the molecule they belong to passes by an empty surface site is proportional to $\nu a/V_l$, where a is the lattice constant of GaAs. The number of empty sites encountered by a mobile $\text{SiBr}_4(\text{ads})$ is proportional to the area swept by the molecule, which is $2(b_2/\pi)^{1/2}V_l$ per unit time, where b_2 is the area constant per molecule of the two dimensional van der Waals equation [7.13]. A_3 is therefore proportional to $2\nu a(b_2/\pi)^{1/2}$. If R_g of Equation (7.5) is expressed in terms of ML/s, then A_3 of Equation (7.5) satisfies

$$A_3 \sim 4\nu(b_2/\pi)^{1/2} \quad (7.6)$$

Equation (7.5) is applied to CBE of GaAs with SiBr_4 , TEGa , and TDMAAs as the dopant, group-III and group-V precursors respectively. A numerical model for GaAs CBE with TEGa and TDMAAs is developed in Chapter 4. It is demonstrated there that properly combining reaction mechanisms derived from surface-science desorption studies enabled one to predict well the growth rate without adjustable parameters. θ and R_g directly output by the growth model are used here to derive (E_a-Q) and A_3 of Equation (7.5) through fitting and, then, to calculate doping concentrations for growth under conditions

other than those for the fitting. Comparison is then made between predicted and measured doping concentrations.

7.4 Results and discussion

Fig. 7.1 is a plot of variation of $R_g n / (1-\theta)^2$ with the inverse of the growth temperature. The doping concentration n in the calculation are measured values from growth runs with 0.4 sccm TEGa, 1 ML/s TDMAAs, 0.1 Torr SiBr₄ upstream-pressure and 80 SiBr₄ leak-valve setting. The straight line through the data points yields $E_a - Q = 18.6$ kcal/mole and $n = 1.363 \times 10^{23} (1-\theta)^2 \exp[-(E_a - Q)/RT] / R_g$ cm⁻³. At 0.1 Torr SiBr₄ upstream pressure and an LV leak valve setting, the above expression for n needs to be multiplied by LV/80 to obtain the doping concentration.

The critical molar volume of SiBr₄ is 382 cm³/mole [7.14] using which we can obtain the b_2 value [7.13] of SiBr₄. $b_2 = 3.4 \times 10^{-15}$ cm². For GaAs, $N_s = 6.4 \times 10^{14}$ cm⁻². With Expressions (7.5) and (7.6), we therefore find that $v\tau_0 \sim 177$. The stretching frequency of gas-phase SiBr₄ is $\sim 10^{13}$ s⁻¹ [7.15]. Thus $\tau_0 \sim 1.8 \times 10^{-11}$ s. The estimation of τ_0 is very likely on the higher-value side because on a surface vibrational freedom of a molecule is restricted [7.13] and the stretching frequency of adsorbed SiBr₄ is most likely larger than 10^{13} s⁻¹. Robertson et al. [7.10] derived the desorption rate of adsorbed TEGa from which we can find that τ_0 for TEGa is 1.7×10^{-12} s. These τ_0 values are larger than 10^{-13} s which is often picked as a first-guess τ_0 value in surface science studies. An adsorbed molecule may be thought of as a mass attached to a surface by a spring [7.16]. The fact that τ_0 's for SiBr₄ and TEGa are relatively larger may be understood with consideration of their large molecular weights. Therefore, the high doping efficiency of SiBr₄ may also be owing to its very large molecular weight. The binding energy of physisorbed SiBr₄ should be on the order of 10 kcal/mole typical for physisorption of large molecules. A value in low tens of kcal/mole can be deduced for E_a . This value should be compared to the gas-phase value of 87.9 kcal/mole for the activation energy of

removing one Br ligand from SiBr_4 . The lower value for the surface Reaction (7.3) indicates a large stabilization of the transition state by surface bonding.

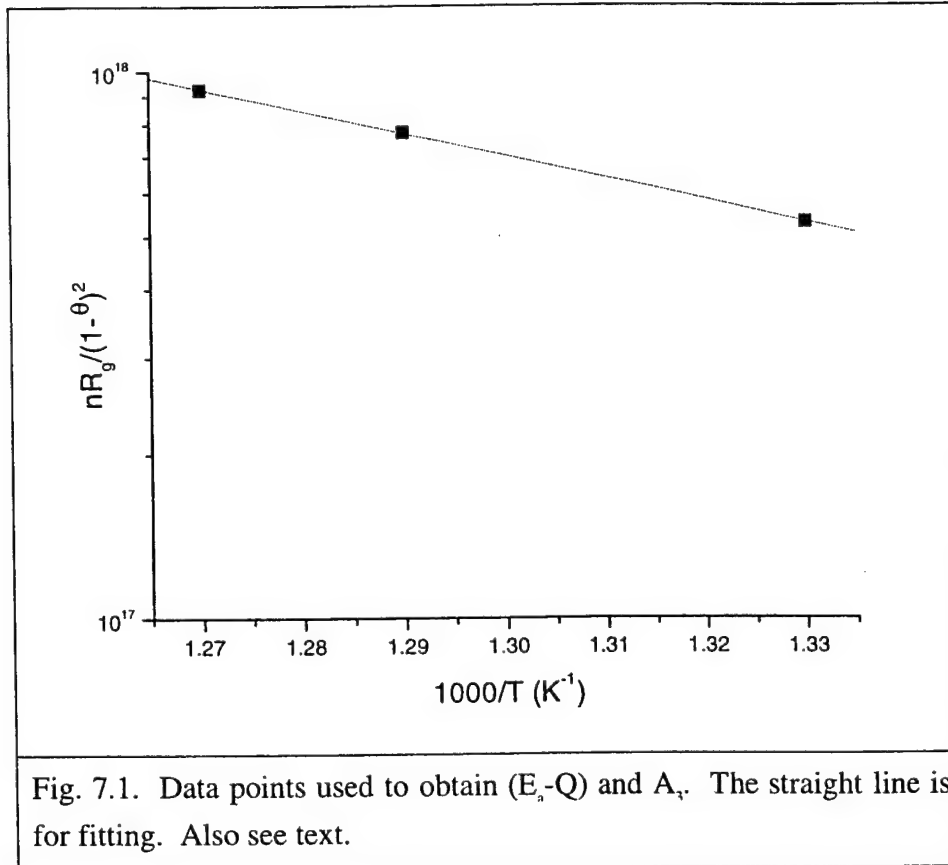


Fig. 7.2 shows comparison between the predicted dopant concentration and the measured net carrier concentration at various growth conditions. The SiBr_4 upstream pressure and leak valve setting were 0.1 Torr and 80, respectively. We can see that the agreement is very good. Combination of the doping Equation (7.5) with the growth numerical model enables us to achieve a desired doping level efficiently.

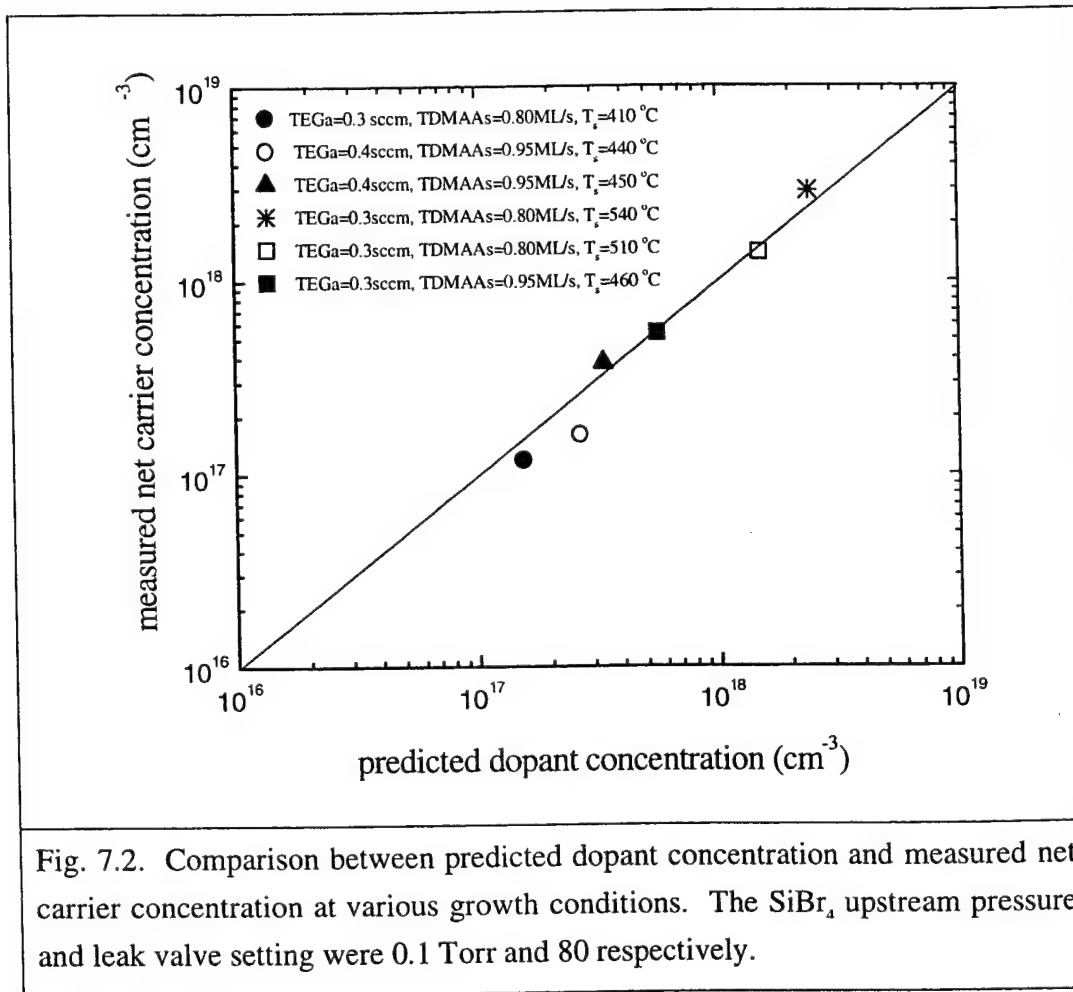
Using $R_s = nR_g$ and $n = 1.363 \times 10^{23} (1-\theta)^2 \exp[-(E_a-Q)/RT]/R_g$, we can find that when the substrate temperature is less than 846 °C, R_s is less than one tenth of the incident flux. This means that at typical CBE growth temperatures, Equation (7.4) is a good approximation for adsorbed SiBr_4 concentration. With consideration of the bonding

strength of H-SiH_3 (91.8kcal/mole [7.14]) and the relatively light molecular weight of SiH_4 , we may expect that Equation (7.4) should also be a good approximation for SiH_4 surface adsorption at typical MOVPE growth temperatures. Regarding the issue of desorption of Si-containing radicals, the agreement between Equation (7.5) and measurement data shown in Fig. 7.2 indicates that at typical CBE growth temperatures, the steady-state desorption rate of adsorbed SiBr_3 is indeed much smaller than R_3 as we assumed in Section 7.3. The MOVPE growth temperature can be much higher than those used in CBE, and SiH_4 can therefore be used directly as a dopant precursor [7.7]. It may be necessary for us to take into account desorption of SiH_3 from the growth surface in MOVPE. Then the Si incorporation should depend on the competition between decomposition and desorption of adsorbed SiH_3 radicals just like the cases of carbon incorporation from methane and halomethanes in MOVPE grown GaAs [7.5]. If the decomposition of adsorbed SiH_3 is much slower than the desorption of adsorbed SiH_3 , the steady-state decomposition rate of adsorbed SiH_3 is then similar to that of adsorbed SiBr_3 discussed above and an apparent activation energy for doping may be extracted. Redwing et al. [7.7], in their study of Si incorporation from SiH_4 into MOVPE GaAs, found that the use of TBA resulted in a greater (by a factor of 10) SiH_4 doping efficiency and weaker dependence on growth temperature than is typically observed with AsH_3 . TBA decomposition occurs at lower temperature than arsine does. If availability of adsorbed arsenic atoms is crucial to further decomposition of intermediate decomposition products of SiH_4 , their observation may be explained in terms of magnitudes of decomposition and desorption rates of surface Si-containing radicals. However, the effect of surface site blocking by arsine-related and TBA-related species on SiH_4 adsorption has to be assessed first before a definite conclusion can be drawn.

7.5. Summary

We have analyzed the behavior of surface decomposition of SiBr_4 as a dopant in GaAs CBE based on 1) the doping efficiency, 2) estimation of the SiBr_4 absolute incident flux, 3) experimentally observed long desorption time of Si-containing species from GaAs surfaces, and 4) our understanding of surface decomposition of metalorganic species. An analytical expression is derived for calculating the doping concentration.

Utilizing a numerical model developed for CBE of GaAs with TEGa and TDMAAs, we have tested our analytical work and obtained very good agreement between predicted and measured doping concentrations. Our analyses also lead us 1) to conclude that the upper limit to the activation energy of dissociative chemisorption of SiBr_4 is in low tens of kcal/mole, and 2) to postulate that the fact that a SiBr_4 molecule is of a very large molecular weight may result in relatively low tendency for it to leave the growth surface and, thus, may be one of the reasons for SiBr_4 possessing a high doping efficiency.



References

- [7.1] P.J. Skevington, D.A. Andrews, and G.J. Davies, *J. Cryst. Growth* **105**, 371 (1990).
- [7.2] S.L. Jackson, M.T. Fresina, J.E. Baker, and G.E. Stillman, *Appl. Phys. Lett.* **64**, 2867 (1994).
- [7.3] S. Izumi, N. Hayafuji, K. Ito, K. Sato, and M. Otsubo, *Appl. Phys. Lett.* **68**, 3102 (1996).
- [7.4] N.Y. Li, *Ph. D thesis*, University of California, San Diego, California (1997).
- [7.5] N.I. Buchan, T.F. Kuech, G. Scilla and F. Cardone, *J. Cryst. Growth* **110**, 405 (1991).
- [7.6] S. J. Bass, *J. Cryst. Growth* **47**, 613 (1979).
- [7.7] J.M. Redwing, H. Simka, K.F. Jensen and T.F. Kuech, *J. Cryst. Growth* **145**, 397 (1994).
- [7.8] B.Q. Shi and C.W. Tu, submitted to *J. Cryst. Growth* (1998).
- [7.9] N.Y. Li, H.K. Dong, C.W. Tu and M. Geva, *J. Cryst. Growth* **150**, 246(1994) .
- [7.10] A. Robertson, Jr., T.H. Chiu, W.T. Tsang and J.E. Cunningham, *J. Appl. Phys.* **64**, 877 (1988).
- [7.11] B.Q. Shi and C.W. Tu, *J. Electr. Mat.* **28**, 43-49 (1999).
- [7.12] S. Shogen, M. Ohashi, Y. Matsumi, M. Kawasaki, *Appl. Surf. Sci.* **80**, 439 (1994).
- [7.13] J.H. de Boer, *The Dynamical Character of Adsorption*, Oxford at the Clarendon Press (1968).
- [7.14] D.R. Lide, *CRC Handbook of Chemistry and Physics*, 78th edition, CRC Press, Boca Raton, New York (1997).
- [7.15] T. Shimanouchi, *Tables of Molecular Vibrational Frequencies, Consolidated Volume I*, NSRDS-NBS 39, National Bureau of Standards (1972).
- [7.16] R.P.H. Gasser, *An Introduction to Chemisorption and Catalysis by Metals*, Clarendon Press, Oxford, Chapter 2 (1985).

CHAPTER 8

EXPERIMENTAL and NUMERICAL STUDIES OF Ar⁺-LASER ASSISTED Si DOPING OF GaAs WITH SiBr₄ BY CHEMICAL BEAM EPITAXY

8.1 Introduction

Laser-assisted epitaxy with metalorganic species as precursors is intended for achieving lateral variations of doping, thickness and composition in an epitaxial layer without using complicated prepatterning and regrowth procedures. Silicon is the preferred n-type dopant for InP- and GaAs-based device structures due to its low thermal diffusivity and the absence of any surface segregation and memory effect during epitaxial growth. Making use of the fact that tetramethylsilane is effectively decomposed by a 193-nm ArF excimer laser, Ban et al. [8.1] reported growth of GaAs p-n junctions and doping superlattices in a metalorganic chemical vapor deposition (MOCVD) reactor simply by switching on and off the laser irradiation. Sugioka et al. [8.2] performed a study of Si incorporation from an ambient of silane (SiH₄) gas into GaAs using a 248-nm KrF excimer laser. They demonstrated that the rapid melting and cooling process of GaAs surfaces associated with short (23 ns) pulses of the excimer laser resulted in high carrier concentrations in shallow (~ 170 nm) surface layers. It is known that an argon ion laser, compared to an excimer laser, is easier to operate and does not cause the problem of plastic deformation of the crystal lattice associated with large thermal stresses. Roberts et al. [8.3] used a scanning multiple-wavelength (488-514 nm) Ar⁺ laser beam to stimulate growth of GaAs doped by silane at a substrate temperature of 400 °C in an atmospheric pressure MOCVD reactor. With the laser power density maintained between 900 and 1000 W/cm², the electron carrier concentration obtained was around 10¹⁸ cm⁻³ when the silane mole fraction was equal to the trimethylgallium mole fraction.

Use of laser beams as the stimulation energy source in MOCVD reactors encounters complications due to Rayleigh scattering [8.4] of the beams by gas molecules and dispersion of possible gas-phase photo-generated intermediate products. We report here doping results from Ar⁺-laser-assisted chemical beam epitaxy (CBE), which is a

growth technique utilizing ultra-high vacuum systems. Triethylgallium (TEGa), tris(dimethylamino) arsenic (TDMAs) and silicon tetrabromide (SiBr_4) were used as group-III, group-V and dopant precursors, respectively. SiBr_4 was chosen in our study because it had been demonstrated to be a high-efficiency vapor source for the controlled incorporation of electrically active silicon into InP- and GaAs-based device structures [8.5-8.7]. In addition, the net electron concentration and mobility of the samples grown with SiBr_4 are comparable to those obtainable in molecular beam epitaxy (MBE) with elemental Si or Sn [8.5]. In our study, a seventy-fold increase in the n-type doping concentration was obtained with Ar^+ laser irradiation. To quantitatively evaluate the issue of whether pyrolytic or photolytic processes are mainly responsible for the observed doping enhancement, the numerical model for simulating growth and dopant chemical processes of GaAs CBE with the three precursors was utilized (Chapters 4 and 7,[8.8]-[8.9]). The numerical model, based on results from surface-science studies, enables us to predict well the growth rate and doping concentration without adjustable parameters. Based on the modeling study, a photolytic process is thought to be mainly responsible for the observed doping increase. To test the hypothesis that photo-decomposition of physisorbed SiBr_4 is the process, we derived an expression for first-order photo-decomposition kinetics of physisorbed SiBr_4 . We then estimated the value of the absorption cross section and the heat of adsorption of SiBr_4 to reproduce the measured carrier concentrations of the films grown with laser irradiation.

8.2 Experimental methods

The CBE system used in this study is a modified Perkin-Elmer 425 MBE system, equipped with gas lines for metalorganic species and a 1600 l/s turbomolecular pump. The argon ion laser employed in this study emitted multiline visible light (454.5 nm - 514.5 nm) with a major power peak at 488 nm. High-purity (99.999%) SiBr_4 without any carrier gas was delivered into the growth chamber through an ultra-high vacuum leak valve. The vapor pressure immediately upstream of the leak valve was sensed by a Baratron pressure sensor. TEGa was injected into the chamber directly using a mass flow controller (MFC) downstream of the TEGa bubbler. TDMAs was carried by purified

H₂ gas into the chamber, while the flow rate of H₂ gas into the TDMAAs bubbler was adjusted with an MFC upstream of the TDMAAs bubbler. Substrate temperatures were measured using an infrared optical pyrometer which was calibrated by observing the appearance of 4x reflection high-energy-electron diffraction (RHEED) surface reconstruction patterns of a substrate upon thermal desorption of surface oxides at 580 °C. The laser optical path consisted of two reflection mirrors, one focus lens and one Pyrex[®] glass viewport of the MBE system. Rotations of the two mirrors allow scanning the laser beam over the substrate surface. Detailed description of the CBE system and Ar⁺ laser optical setup has been given in Chapters 5 and 7.

The laser irradiated area in this study was a 1.5 mm x 1.5 mm square. The laser output power was set at different values with the power density varying from 50 W/cm² to 300 W/cm². The frequencies of the rotating mirrors were 7.5 Hz and 40 Hz. The SiBr₄ leak-valve and Baratron pressure were 80 and 0.1 Torr, respectively. The TEGa MFC setting was 0.3 sccm, while that of H₂ gas into the TDMAAs bubble 3 sccm. Since the absolute TDMAAs flux incident on the substrate is governed by the nonlinear fluid dynamics of H₂ gas and TDMAAs fluid in the bubbler, we determined the TDMAAs absolute incident flux in terms of monolayers per second (ML/s) through group-V induced RHEED intensity oscillations at a substrate temperature in between 420 °C and 470 °C. With 3 sccm H₂ flow, the absolute TDMAAs flux was determined to be 0.95 ML/s. The investigated substrate-temperature ranged from 390 °C to 500 °C. With the precursors' flow conditions given, the V/III incorporation ratio was larger than 1.6 and the growth chamber pressure was around 8 x 10⁻⁶ Torr. The laser-irradiated film grown at 500 °C is 0.4 μm in thickness, while the films at other growth temperatures are thicker than 0.6 μm.

All epitaxial layers were grown on semi-insulating epi-ready GaAs(100) substrates which were In soldered to 3-inch-diameter silicon wafers. The mobility and the electron concentrations were determined using the van der Pauw-Hall technique. The growth rate over the nonirradiated area was derived from group-III induced RHEED intensity oscillations. A microstylus profilometer (DEKTAK) was used to probe any growth enhancement over the laser-irradiated area. The film thickness used in Hall

measurement calculations for the laser-irradiated area was a summation of the thickness from nonstimulated growth and the thickness enhancement due to laser stimulation.

8.3 Results and discussion

Fig. 8.1 shows measured carrier concentrations in films from growth runs without and with laser irradiation of 300 W/cm^2 power density. An increase in the concentration by 70 times was obtained at 392°C . The dash curve in the figure is the prediction using the numerical model of Chapter 7 for GaAs CBE with TEGa, TDMAAs and SiBr_4 as precursors. The growth component of the model was established by properly combining reaction mechanisms derived from surface-science desorption studies of TEGa and TDMAAs (Chapter 4), while the doping component resulted from analyses in Chapter 7 of the behavior of surface decomposition of SiBr_4 as a dopant in GaAs CBE based on 1) the doping efficiency, 2) estimation of the SiBr_4 absolute incident flux, 3) experimentally observed long desorption time of Si-containing species from GaAs surfaces, and 4) our understanding of surface decomposition of metalorganic species. We see that the model can indeed reproduce well the experimental results. The solid-line curve is output by a modified version of the model with photolysis of SiBr_4 incorporated, which we will elaborate shortly. Fig. 8.2 plots Hall mobility data of samples shown in Fig. 8.1. The curve is from Hilsum's simple interpolation formulae [8.11] for 300 K n-GaAs. It is evident that the mobility in films grown with laser irradiation is comparable to that without laser. Laser stimulation at low growth temperatures resulted in samples of not only much higher carrier concentrations ($> 10^{18} \text{ cm}^{-3}$), but also good electronic characteristics. For the nonirradiated samples, the electron concentration decreased as the growth temperature was lowered. Thus, the background carbon concentration, which arises typically during CBE growth, became relatively significant at low growth temperatures. The drop in mobility of the samples as compared to the Hilsum's curve may be attributed to carbon compensation of free electrons from silicon donors.

The localized temperature rise due to Ar^+ laser irradiation can be measured using an infrared laser interferometry [8.12]. The temperature rise with irradiation of 300

W/cm² power density should be around 20 °C in our experiment. To see whether laser thermal heating alone can account for the observed change in doping concentration, the ratio of the free electron concentration with laser to that without laser is computed and plotted in Fig. 8.3. Also shown in Fig. 8.3 are the predicted ratios using the growth and doping model with consideration of thermal heating due to laser. The laser-induced temperature rises assumed in the simulation are indicated in the figure. We can see that at high temperatures the enhancement ratio approaches the theoretical prediction, while at temperatures lower than 420 °C the ratio is well beyond the prediction, indicating that a photo-decomposition mechanism of SiBr₄ became dominant as the substrate temperature was lowered. Our analyses (Chapter 7 or [8.8]) of Si incorporation from SiBr₄ through thermal decomposition showed that the first step leading to incorporation is the dissociative chemisorption of physisorbed SiBr₄. One of the curves in Fig. 8.4 depicts the simulated variation of the rate of the chemisorption as a function of the substrate temperature. We can see that dramatic doping enhancements occur when the chemisorption rate becomes much smaller than that at 500 °C due to insufficient thermal energies at low temperatures to overcome the dissociation activation energy barrier.

Since surface decomposition of chemical species in epitaxial processes involve surface dangling bonds, it is necessary for us to consider effects of carriers generated as byproducts of Ar⁺-laser irradiation of GaAs on the dangling-bond concentration of the GaAs surface. Arguments of Chapter 6 for quantitative evaluation of laser-enhanced catalytic effects are directly applicable here. With laser power output at 6.75 W, the I_{\max} in Equation (6.1) is $1.3 \times 10^{22} \text{ cm}^{-2} \text{ s}^{-1}$ in our experimental setup. Therefore, the steady-state maximum excess-carrier concentrations at the surface ($\delta n(0)$ and $\delta p(0)$) are approximately $1 \times 10^{16} \text{ cm}^{-3}$. By multiplying the concentration by $a/4$, where a is the lattice constant of GaAs, the maximum excess carrier concentration on the surface atomic plane is then $\sim 1.4 \times 10^8 \text{ cm}^{-2}$, which is much less than $6.3 \times 10^{14} \text{ cm}^{-2}$, the GaAs(100) surface dangling-bond concentration. Thus, it is very likely that the Ar⁺-laser irradiation used in this study did not impose enhanced catalytic effects on surface decomposition of metalorganic species.

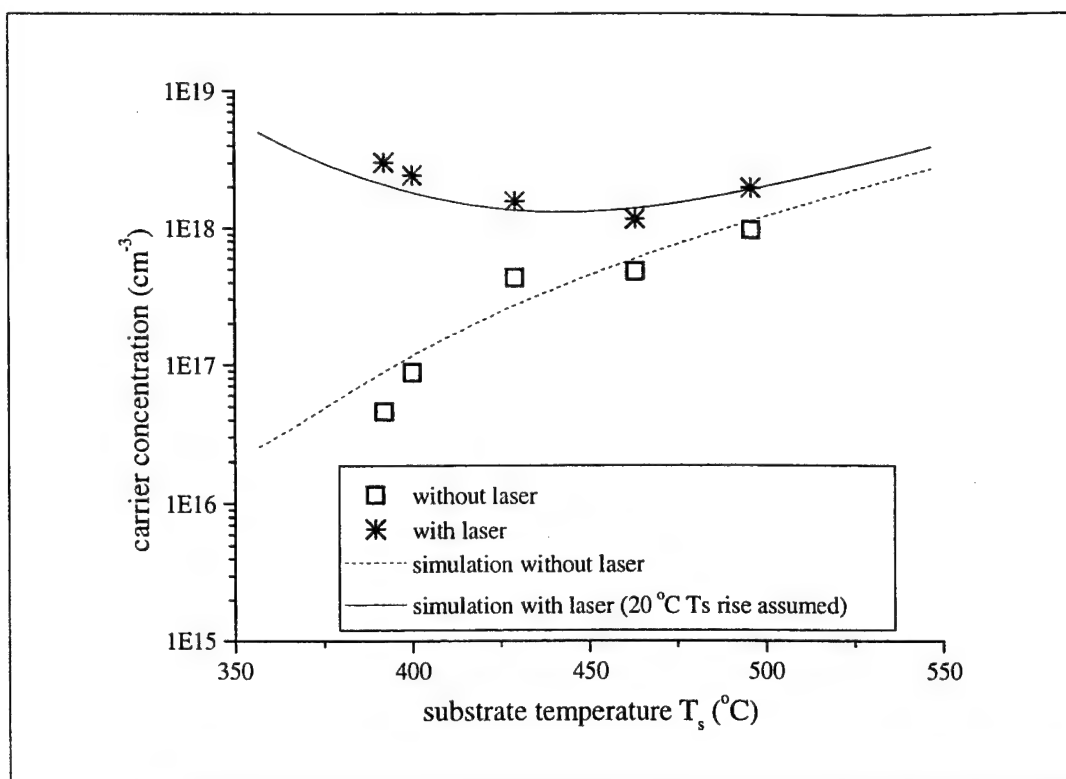
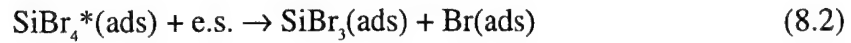
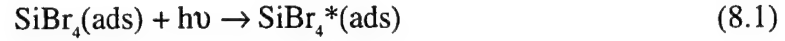


Fig. 8.1. Measured carrier concentrations at different substrate temperatures with and without laser irradiation. Solid and dashed lines are concentrations predicted by numerical models with and without laser-induced effects included, respectively. The temperature rise due to 300 W/cm² laser irradiation is assumed to be 20 °C.

The above discussion leads us to believe that the observed dramatic increase in Si incorporation with impinging photons is due to enhanced decomposition of physisorbed SiBr₄ through photochemical processes. It is a common assumption that adsorbed-phase absorption of light can be attributed to the same electronic processes as those in the gas phase. The UV absorbance spectra of silicon tetrabromide reported by Clark et al. [8.13] exhibits a featureless long-wavelength tail extending smoothly into the visible region. We estimate here the magnitude of SiBr₄ absorption cross section required to reproduce the experimental results. The simulated total coverage in monolayer (ML) of the first layer adsorbed on the surface is shown in Fig. 8.4. We see that at temperatures higher than 390 °C, more than half of the surface sites are empty. The binding van der Waals force of a molecule on the surface of a solid is, in general, greater than the binding van

der Waals force when it is adsorbed on top of adsorbed layers of nonunity coverage [8.14]. We therefore consider only those SiBr_4 molecules directly bound to the GaAs surface. The photo-induced SiBr_4 decomposition is assumed to go through the following sequence:



where (ads) denotes an adsorbed species and $h\nu$ a photon; and SiBr_4^* is a SiBr_4 molecule in an excited state and e.s. an empty surface site where adsorption and reactions can occur. Dissociative chemisorption (Reaction (8.2)), instead of photo-induced direct cleavage of the Br-SiBr_3 bond, is considered more likely, based on the energy of impinging photons. The Br-Si diatomic bond dissociation energy is 87.9 kcal/mole [8.15], while the energy of 488 nm photons is 58.6 kcal/mole. In Chapter 7 analyses of SiBr_4 doping of GaAs, it was found that the activation energy for SiBr_4 dissociative chemisorption is 18.6 kcal/mole plus the value of SiBr_4 heat of adsorption, which should be on the order of 10 kcal/mole. Therefore, physisorbed SiBr_4 molecules excited by an Ar^+ laser should possess enough energy to overcome the activation energy barrier of Reaction (8.2).

In Chapter 7, the SiBr_4 incident flux onto the substrate corresponding to the flow settings of this study was estimated to be 0.014 ML/s. It was also concluded there that at CBE growth temperatures, with 10^{18} cm^{-3} doping levels obtained, the SiBr_4 dissociative chemisorption rate is much less than the incident flux. Therefore, the steady-state concentration σ of physisorbed SiBr_4 can be determined by equating the evaporation rate to the incident flux. Employing the Langmuir's kinetics [8.14], we can have

$$\sigma = FN_s(1 - \theta)\tau_0 \exp\left(\frac{Q}{RT}\right), \quad (8.3)$$

where θ is the total surface coverage, F the incident flux, $N_s = 6.3 \times 10^{14} \text{ cm}^{-2}$, τ_0 the time of oscillation, and Q the heat of adsorption of physisorbed SiBr_4 . The rate of formation of $\text{SiBr}_4^*(\text{ads})$ is then equal to $k\sigma$, with k being the specific absorption rate. If we assume that the absorption cross section α is constant over the wavelength range of the Ar^+ laser used in this study, $k = J\alpha$, with J being the incident photon flux. As discussed in Chapter 7, the evaporation process of $\text{SiBr}_3(\text{ads})$, with its Si atom firmly bonded on the surface, should be slow at CBE growth temperatures. The dissociation energies of the remaining Si-Br bonds are most likely to be lower than that of the Br-SiBr₃ bond by analogy with the values of successive bond dissociation energies calculated by Walsh [8.16] for SiH_4 and SiF_4 . Therefore, we assume that every chemisorbed SiBr_3 eventually contributes one Si dopant atom for incorporation and the silicon incorporation rate can be equated to the rate of SiBr_4 dissociative chemisorption rate. Thus, with the reaction sequence outlined above, the photo-induced doping enhancement Δn is

$$\Delta n = J\alpha FN_s \frac{1-\theta}{R_g} \tau_0 \exp\left(\frac{Q}{RT}\right) \quad (8.4)$$

where R_g is the epitaxial growth rate. 300 W/cm^2 power density corresponds to 7.4×10^{20} 488nm-photons per $\text{cm}^2\text{-s}$. Approximately 53% of photons output by laser impinge on the substrate surface in our experimental setup due to the imperfect reflectivity of the reflection mirrors and lens transmittance [8.12]. Therefore, $J = 3.9 \times 10^{20} \text{ cm}^{-2} \text{ s}^{-1}$. θ and R_g are directly computed in our numerical model. τ_0 was estimated to be $1.8 \times 10^{-11} \text{ s}$ in Chapter 7. With F being 0.014, the only parameters unknown in Equation. (8.4) are α and Q .

The upper curve of Fig. 8.1 corresponds to the dopant concentration computed using Equation. (8.4) when $\alpha = 2 \times 10^{-19} \text{ cm}^2$ and $Q = 20 \text{ kcal/mole}$. A heat-of-adsorption value of 20 kcal/mole for SiBr_4 on a reactive growth surface appears reasonable. For triethylgallium molecules physisorbed on such a surface, heat-of-adsorption values of 12 to 13.6 kcal/mole were derived by two groups [8.17-8.18]. McCrary et al. [8.19] reported room-temperature UV peak absorption cross sections of $1.7 \times 10^{-17} \text{ cm}^2$ to $5.6 \times 10^{-17} \text{ cm}^2$ for

selected precursors used in the chemical vapor deposition of GaAs. We see that the cross section required for reproducing the observed doping enhancement can be only one one-hundredth of typical UV peak absorption-cross-section values. It is worth pointing out, though, that in the calculation of laser-enhanced doping concentrations, the quantum yield of Reaction (8.2) was assumed to be unity. $2 \times 10^{-19} \text{ cm}^2$ is therefore a value of the lower limit of the required absorption cross section. However, we also expect enhanced SiBr_4 absorption at visible wavelengths at growth temperatures since many more molecules occupy higher vibrational levels of the ground electronic state at elevated temperatures, as dictated by Boltzmann statistics.

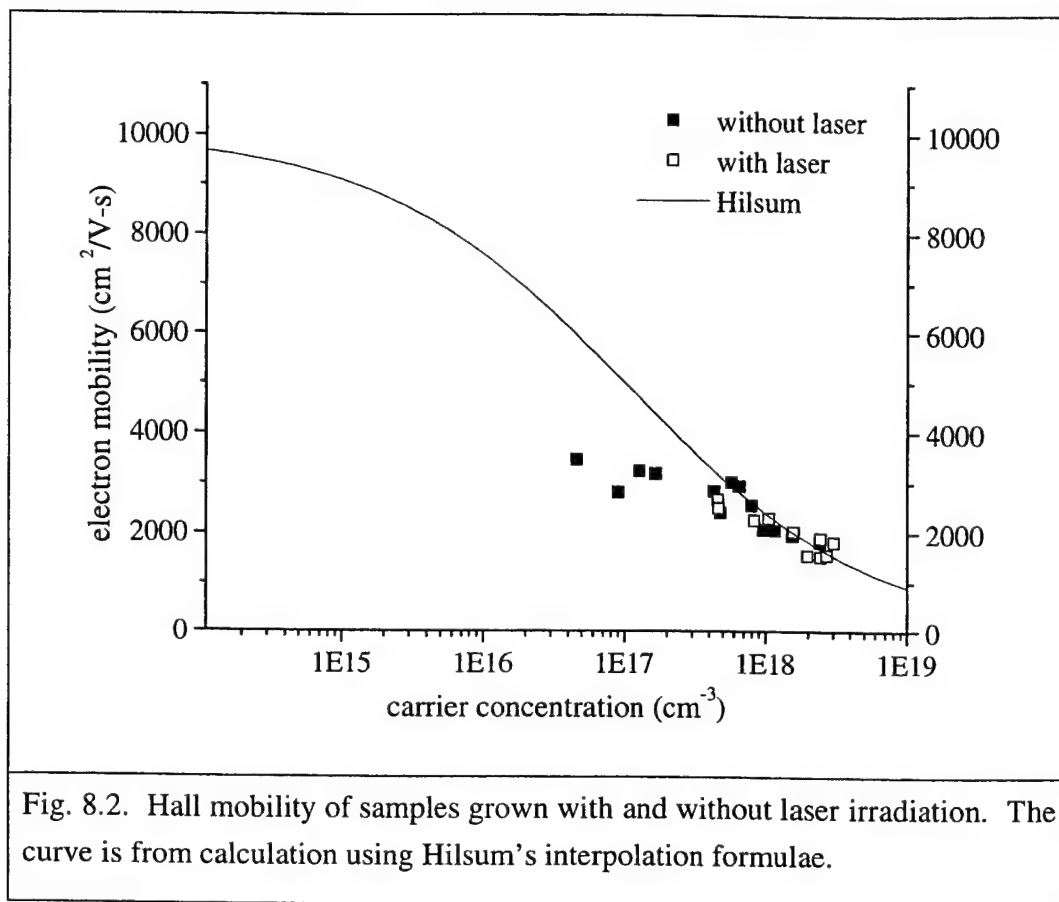
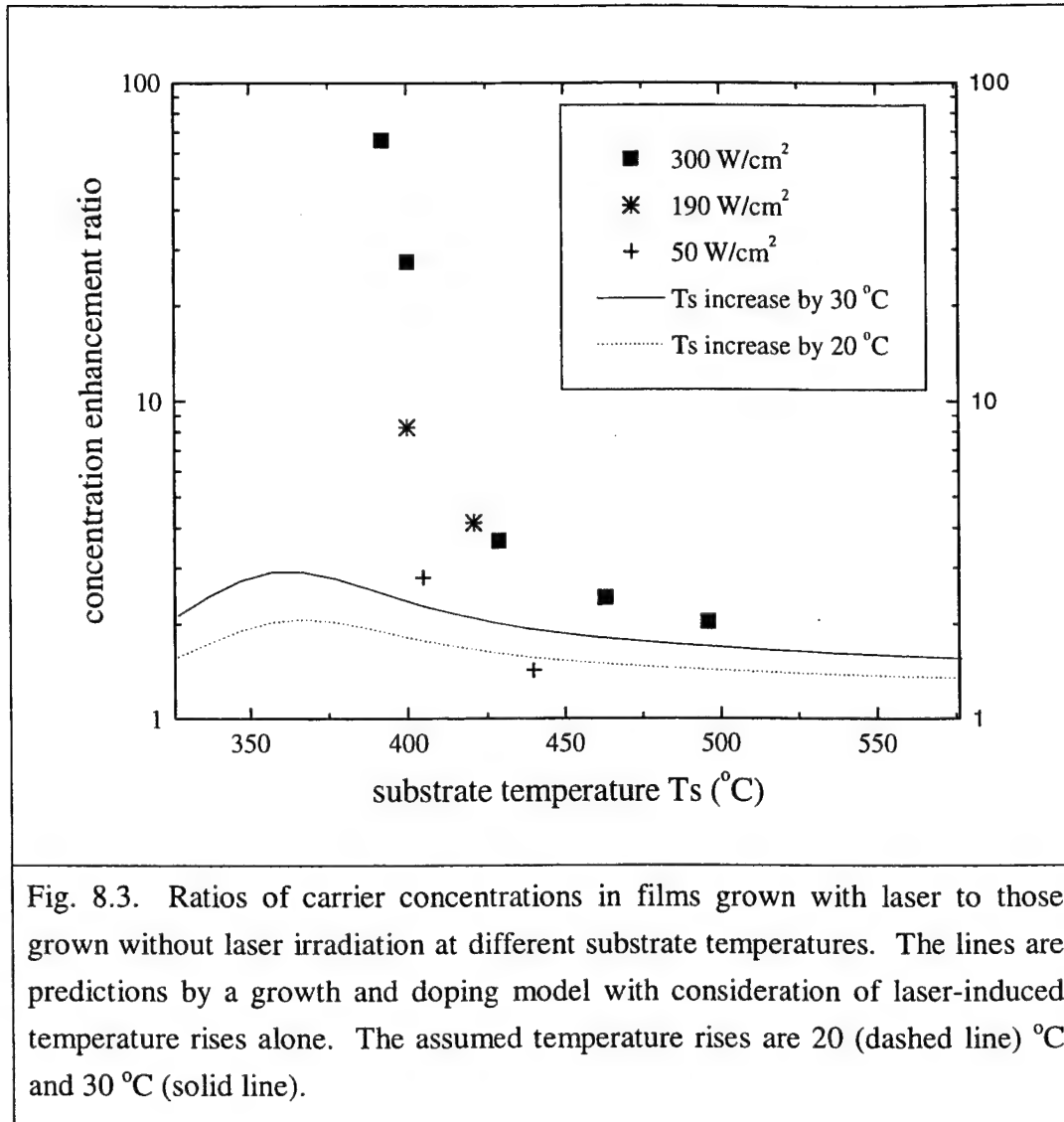


Fig. 8.2. Hall mobility of samples grown with and without laser irradiation. The curve is from calculation using Hilsum's interpolation formulae.

Fig. 8.5 shows the simulated variation of the surface coverage of physisorbed SiBr_4 on GaAs with the substrate temperature. In the simulation, values of α and Q are the same as those for Fig. 8.1. The photolysis rate at the maximum surface coverage is calculated to 8.7×10^{-6} ML/s, which is much less than the incident flux of SiBr_4 . Therefore the photochemical process has a negligible effect on the surface coverage of SiBr_4 . Our assumption above is valid that the surface coverage can be determined from a balance between the impingement and the evaporation process.



8.4 Summary

Photon-assisted CBE of n-GaAs with SiBr_4 as the dopant precursor has been performed. Dramatic increases in the carrier concentration are observed. With laser irradiation, the carrier concentration is larger than 10^{18} cm^{-3} throughout the temperature range investigated (390 °C to 500 °C). Hall measurement of the films grown with laser indicates good electronic characteristics over the entire temperature range. Simulation using a numerical model we developed for doping and growth of GaAs reveals that the observed carrier concentration enhancement cannot be accounted for by laser-induced

temperature rises alone. A photodecomposition reaction scheme is proposed for physisorbed SiBr_4 based on chemical-physics data reported in the literature. It is found that the absorption cross section required to reproduce the experimental results can be two-order magnitudes lower than the typical peak value of UV absorption spectra.

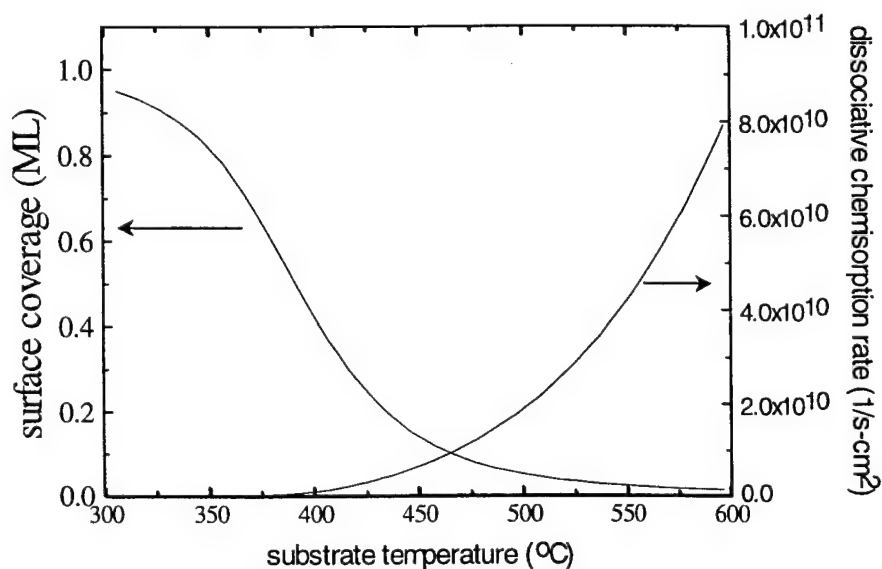


Fig. 8.4. Simulated variation of total surface coverage and dissociative chemisorption rate with substrate temperature.

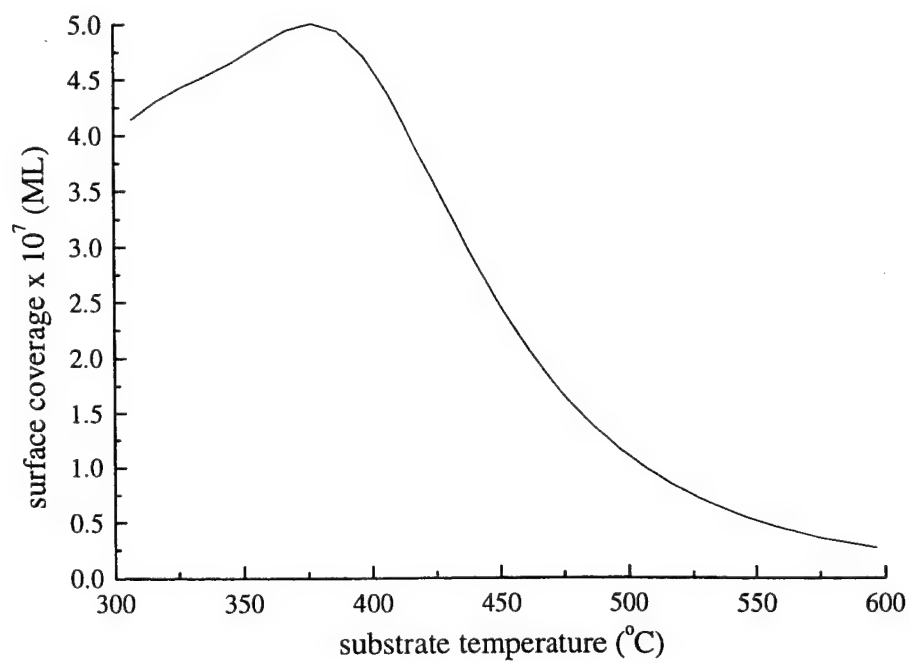


Fig. 8.5. Simulated surface coverage of physisorbed SiBr_4 as a function of substrate temperature.

References

- [8.1] Y. Ban, M. Ishizaki, T. Asaka, Y. Koyama and H. Kukimoto, *Jpn. J. of Appl. Phys.* **28**, L1995 (1989).
- [8.2] K. Sugioka and K. Toyoda, *Appl. Phys. Lett.* **61**, 2817 (1992).
- [8.3] J. C. Roberts, K. S. Boutros, S. M. Bedair and D. C. Look, *Appl. Phys. Lett.* **64**, 2397 (1994).
- [8.4] J. H. Seinfeld, *Atmospheric Chemistry and Physics of Air Pollution*, John Wiley & Sons, Inc., Section 7.5 (1986).
- [8.5] S.L. Jackson, M.T. Fresina, J.E. Baker, and G.E. Stillman, *Appl. Phys. Lett.* **64**, 2867 (1994).
- [8.6] S. Izumi, N. Hayafuji, K. Ito, K. Sato, and M. Otsubo, *Appl. Phys. Lett.* **68**, 3102 (1996).
- [8.7] N. Y. Li, *Ph. D thesis*, University of California, San Diego, California, U. S. A. (1997).
- [8.8] B. Q. Shi and C. W. Tu, *J. Cryst. Growth*, **195**, 740 (1998).
- [8.9] B. Q. Shi and C. W. Tu, submitted to *J. Cryst. Growth* (1998).
- [8.10] B. Q. Shi and C.W. Tu, in *Light Emitting Devices for Optoelectronic Applications and the Twenty-Eighth State-of-the-Art Program on Compound Semiconductors*, edited by H. Q. Hou, R. E. Sah, S. J. Pearton, F. Ren and K. Wada, the Electrochemical Society, Inc., New Jersey, 366-376 (1998).
- [8.11] C. Hilsum, *Electron. Lett.*, **10**, 259-260 (1974).
- [8.12] H. K. Dong, *Ph. D thesis*, University of California, San Diego, California, U. S. A., Chapter 2 (1995).
- [8.13] J. B. Clark and B. R. Russell, *J. Electron Spectroscopy and Related Phenomena* **11**, 371-382 (1977).
- [8.14] J. H. de Boer, J.H. de Boer, *The Dynamical Character of Adsorption*, Oxford at the Clarendon Press, Chapter IV (1968).
- [8.15] D.R. Lide, *CRC Handbook of Chemistry and Physics*, 78th edition, CRC Press, Boca Raton, New York, 9-52 (1997).
- [8.16] R. Walsh, *Acc. Chem. Res.* **14**, 246-252 (1981).
- [8.17] J. S. Foord, C. L. French, C. L. Levoguer and G. J. Davies, *Phil. Trans. R. Soc. Lond. A* **344**, 507-520 (1993).
- [8.18] V. M. Donnelly and A. Robertson, Jr., *Surface Science* **293**, 93-106 (1993).
- [8.19] V. R. McCrary and V. M. Donnelly, *J. Cryst. Growth* **84**, 253-258 (1987).

CHAPTER 9

LASER-ASSISTED CBE GROWTH OF PHOSPHIDES

9.1 Introduction

As stated in Chapter 1, there exist needs to perform additional studies on Ar^+ -laser assisted CBE of phosphides to realize full potentials of growth techniques involving laser irradiation. In this Chapter, results from Ar^+ -assisted CBE of InP and GaInP will be presented.

9.2 Chemical beam epitaxy of InP with Ar^+ laser irradiation

There have been relatively fewer reports on laser-assisted CBE of InP in the literature. Iga et al. [9.1] measured the thickness of InP films grown by CBE with trimethylindium (TMIn) or triethylindium (TEIn), cracked phosphine and a CW argon ion laser. The substrate temperature was varied in the range of 350-525 °C. Using TEIn they found that the growth rates of both the laser-irradiated area and non-irradiated areas were almost constant and the same. They attributed this observation to full thermal decomposition of TEIn at temperatures higher than 325 °C in accordance to Kawaguchi et al.'s work [9.2]. With TMIn they found occurrence of growth rate enhancement by laser irradiation in the substrate temperature range of 350-480 °C. In this study, laser-assisted CBE of InP was performed with TMIn and thermally cracked tertiarybutylphosphine (TBP). The substrate temperature varied from 170 °C to 440 °C. Although both thermally cracked TBP and PH_3 provide P_2 to the growth surface, TBP is less toxic and is accepted as a safer alternative to phosphine.

Descriptions of the CBE system and laser optics setup have been given in Chapters 5 and 7. Semi-insulating InP (001) wafers were used in all experiments of this study. The 2x1 to 2x4 RHEED pattern transition was assumed at 470 °C. The difference (~ 5 °C) between 470 °C and the reading of the substrate thermal couple (TC) at the transition was added to other TC readings to derive the substrate temperatures reported

here. TMIn and TBP were directly injected into the growth chamber without any carrier gas. The TBP cracker operated at around 1000 °C. The flow rates were controlled by vapor-source mass flow controllers (MFC). The MFC settings for TMIn and TBP were 0.35 sccm and 5 sccm, respectively, in this study. The laser-irradiated area in this study was either a 1x1.2 mm² or a 1x1.4 mm² rectangle, while the laser power was correspondingly set at either 5.3 W or 6.2 W. The power density was therefore maintained at 4.4 W/mm². The frequencies of the rotating mirrors R1 and R2 in Fig. 5.1 were set at 15 Hz and 30 Hz, respectively.

In CBE, reflection high-energy electron diffraction (RHEED) can be utilized for monitoring *in situ* surface reconstruction patterns and deriving growth rates by intensity oscillations. The maximum output power of the multiline Ar⁺ laser in Fig. 5.1 is about 7 watts, so the laser irradiation has to be limited within a small area (~ 1 mm²) in order for the irradiation power density to be sufficiently large for significant laser-induced effects to be observable. Nagata et al. [9.3] used small enough GaAs substrates (1x1 mm²) to ensure significant overlapping of the electron and the laser beams to observe the effect of laser on RHEED oscillations. A procedure, as illustrated in the following, has also been established in this study for intersecting the electron beam on the substrate surface with the laser beam. This procedure enables one to conveniently monitor growth over laser-irradiated areas with substrates of typical sizes (> 100 mm²) for growth whenever such monitoring is desired. The laser and the electron beams were made overlapping each other on the InP sample by utilizing the observation that the RHEED intensity of the (00) rod on the (1 $\bar{1}$ 0) recording plane decreases as the InP surface reconstruction pattern changes from 2x1 to 2x4 at a temperature around 470 °C. The decrease in the (00) rod intensity results from more uniform distribution of electrons among diffraction streaks. Since the footprint of the RHEED e-beam on the substrate is a strip of approximately 1 mm x 20 mm, elongated along the direction toward the RHEED viewport, the laser beam could be moved onto the e-beam-irradiated area by changing the galvanometer offset voltage for the R2 reflection mirror. Fig. 9.1 shows the variation of RHEED intensity on the (00) rod while the position of the laser beam was fine tuned to center at the e-beam. Fig. 9.2a is a reconstruction pattern on the (1 $\bar{1}$ 0) recording plane prior to the 2x1 to 2x4 transition without laser light. The reconstruction pattern in Fig. 9.2b resulted from the

Fig. 9.2a pattern having undergone the transition with laser irradiation centering at the e-beam footprint.

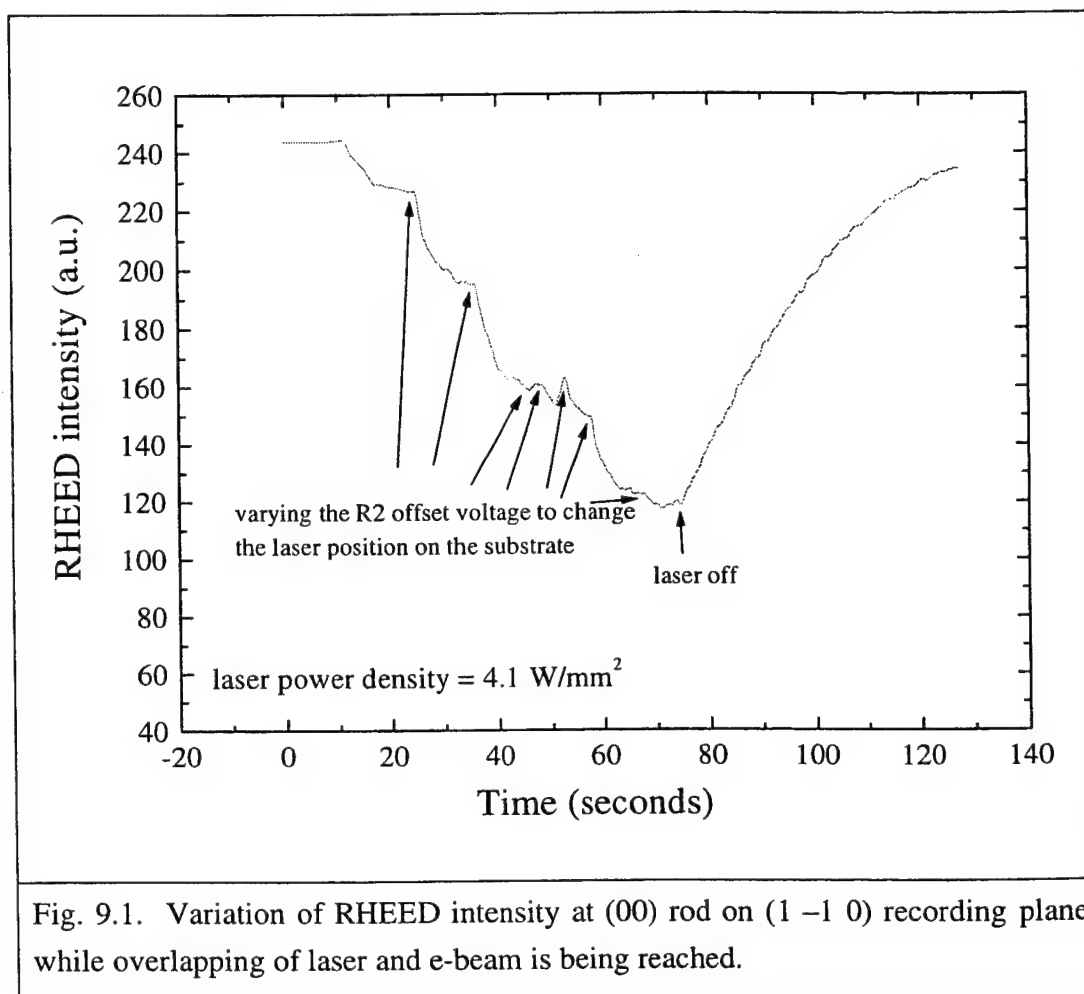


Fig. 9.1. Variation of RHEED intensity at (00) rod on (1 -1 0) recording plane while overlapping of laser and e-beam is being reached.

Fig. 9.3 shows the growth RHEED oscillation curves at 368 °C substrate temperature. The RHEED intensity on the RHEED viewport of phosphorous with laser irradiation was induced by electrons diffracted from the laser irradiated area and non-irradiated area in the e-beam strip on the substrate. Comparing the two curves in Fig. 9.3, we can see that the intensity variation was not very different from each other. Growth enhancement was therefore, as revealed by surface profile measurement, mainly confined within the irradiated area which was small compared to the e-beam strip. But it is also

clear in Fig. 9.3 that growth enhancement caused the oscillation curve of laser-assisted growth to perturb away from that of normal growth.

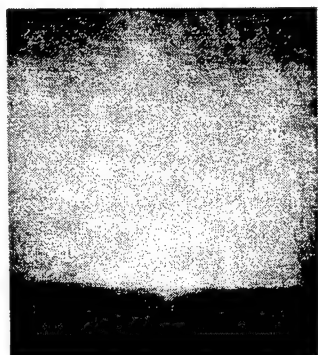


Fig. 9.2a

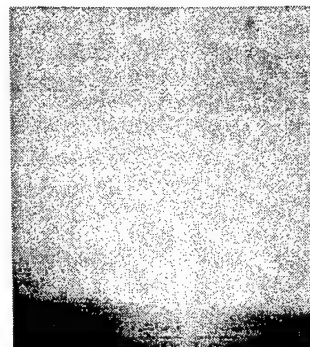


Fig. 9.2b

Fig. 9.2. Surface reconstruction patterns on (1 -1 0) recording plane without laser (a) and with laser (b).

Fig. 9.4 displays the RHEED intensity curve at the (00) rod of the surface reconstruction on the (1 1 0) recording plane during a growth run carried out at 270 °C. Cracked-TBP injection was on all the time. The laser was turned on after 25 seconds of TMIn injection. At this temperature, normal growth ceased and the RHEED intensity decreased with TMIn injection due to adsorbed-TMIn scattering of diffracted electrons from the surface. With laser on, the RHEED intensity initially increased sharply because of both scattered laser light and onset of growth as evidenced by post-growth DEKTAK measurement. The subsequent gradual increase in the RHEED intensity during laser irradiation was most likely mainly associated with decomposition of TMIn and, thus, removal of physisorbed TMIn from the surface. We have confirmed through experiment that with only cracked TBP, a gradual rise in substrate temperature by 30 °C would not cause such an extent of increase in the intensity. At such a low growth temperature,

growth was unlikely through two-dimensional islands formation even with laser. No RHEED oscillation therefore appeared. The decrease right after laser was turned off corresponded to withdrawal of contribution of scattered laser light. With TMIn injection still on, the intensity decreased gradually much like it did before the laser irradiation.

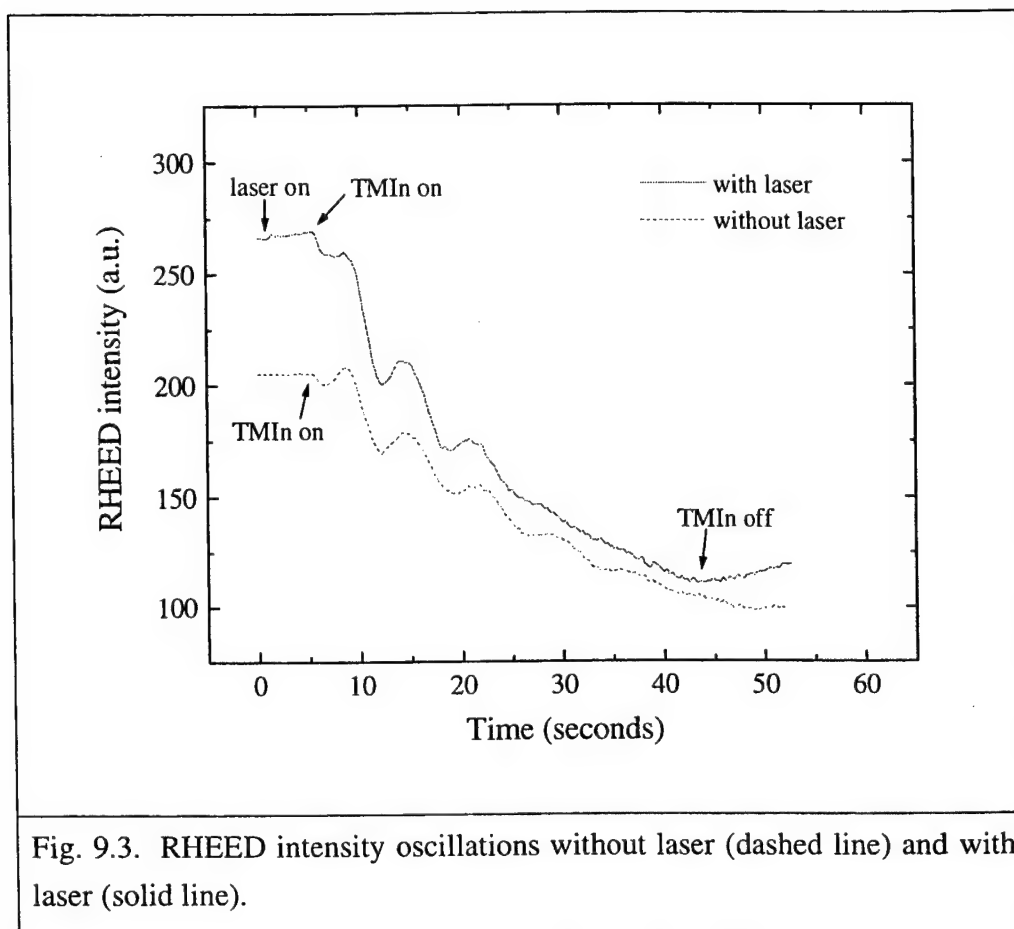


Fig. 9.5 displays the variation of the growth rate over nonirradiated and irradiated areas with the substrate temperature. The growth rate over nonirradiated areas was derived from RHEED intensity oscillations, while the growth rate enhancement over laser-irradiated areas was calculated using surface profile data from DEKTAK measurement of the samples grown. Runs at temperatures lower than 250 °C were carried out after we fixed a problem with the argon ion laser and replaced the entrance glass viewport for the laser light. Even though the laser power was set such that the incoming

power density was calculated to be the same as before, the actual incident power density on the substrate surface was different, because the condition of As and P coating of the viewport was changed. In fact, the growth enhancement at 270 °C was found to be 0.48 ML/s with the new glass viewport as compared to 0.25 ML/s obtained with the old viewport. Therefore we estimate that the three newly collected data are likely to be a factor of 1.9 higher than would have been obtained if we had not changed the laser optics. The triangle-cross data points in Fig. 9.5 are the data from correction of the measured data by this factor. We thus also see that the growth enhancement is sensitive to the incident power density on the substrate. The reproducibility of laser-assisted epitaxy depends, to a large extent, on surface conditions of the viewport and reflection mirrors.

When TMI_n and P₂ from cracked TBP impinge on an InP substrate, both chemisorption and physisorption of these species can occur [9.4]. The growth-rate curve of CBE of InP without laser (square points) in Fig. 9.5 can be interpreted in terms of the chemistry of the chemisorbed layer analogous to that of the chemisorbed layer on a GaAs surface resulted from As₂ and TEGa injection [9.5]. Chemisorption of a TMI_n molecule is most likely through its dissociation into adsorbed CH₃ and (CH₃)₂In radicals [9.6]. The chemisorbed layer may mainly consist of adsorbed P, CH₃ and (CH₃)₂In. Further decomposition of a dimethylindium molecule requires an additional free site at typical growth temperatures. At low temperatures, normal growth ceases because either the temperature is not high enough for activation of dimethylindium decomposition, or all surface sites are occupied. The sharp increase in the growth rate at temperature around 380 °C most likely corresponds to activation of CH₃ desorption which effectively frees sites for continuous TMI_n dissociative chemisorption and surface dimethylindium decomposition. The gradual decrease of the growth rate at temperatures higher than 400 °C is likely due to an onset of desorption of (CH₃)₂In. At even higher temperatures (> 440 °C), both (CH₃)₂In decomposition and desorption may be fully activated thermally and the growth rate may be less varying with the substrate temperature. Evaporation of In atoms from the growth surface is expected to become important at temperatures higher than 500 °C.

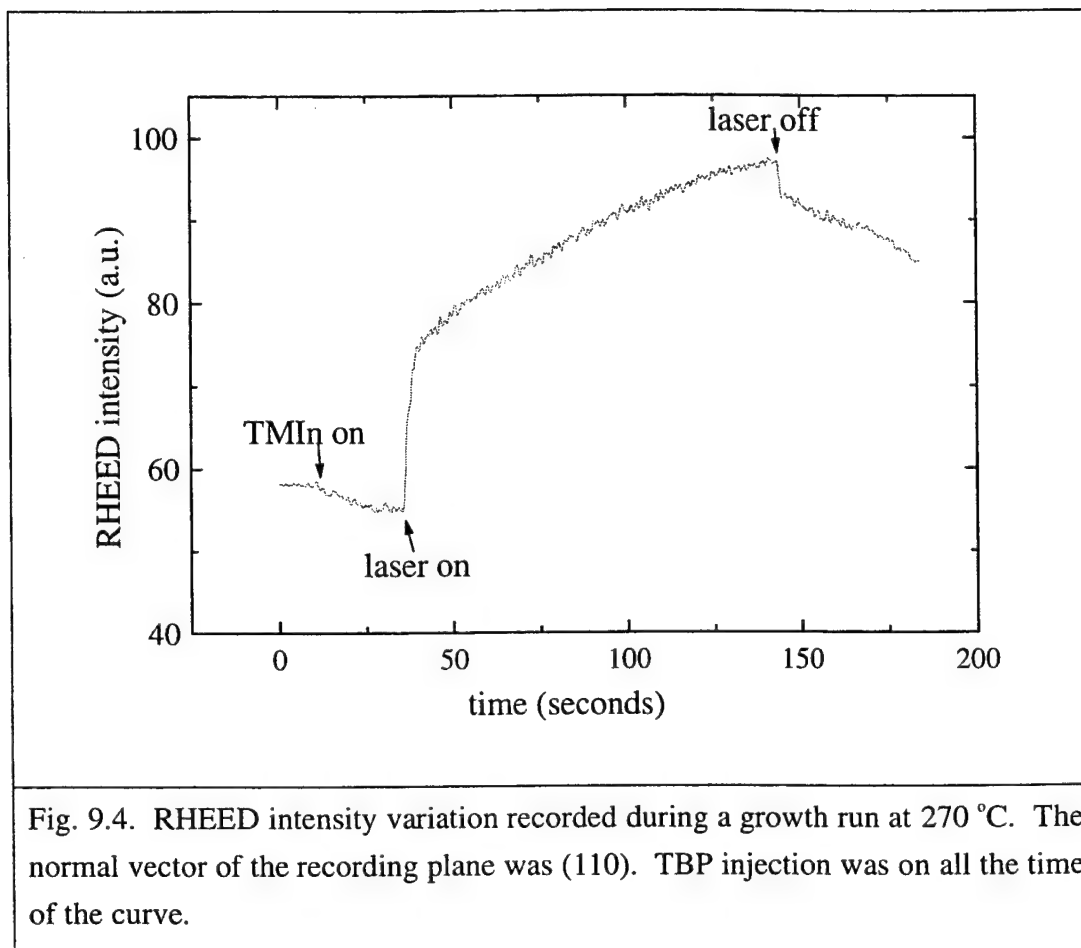


Fig. 9.4. RHEED intensity variation recorded during a growth run at 270 °C. The normal vector of the recording plane was (110). TBP injection was on all the time of the curve.

The localized temperature rise due to Ar^+ laser irradiation can be measured using an infrared laser interferometry [9.7]. The temperature rise with irradiation of 4.4 W/mm^2 power density should be around 25 °C in our experiment system. Using a theoretical formulae reported in the literature, Iga et al. [9.1] made an estimation that in their experiment of 4 W/mm^2 power density, the Ar^+ laser heated InP by about 10 °C. As we can see in Fig. 9.3, the observed changes in the growth rate resulted from laser irradiation can not be accounted for with consideration of the laser-induced thermal heating effect alone.

In Chapter 6, it was found that the Ar^+ laser-induced growth enhancement of GaAs at low temperatures is, to a large extent, due to photodecomposition of adsorbed Ga-containing metalorganic species. It is therefore postulated here that the same

photolytic mechanism operates in the case of the group-III species being TMIn. As far as we know, the work reported here is the first Ar⁺-laser-assisted CBE study which reports significant laser-induced growth at temperatures lower than 200 °C. In Chapter 6, it was also found that group-V related species control the growth-enhancement temperature window because of their site-blocking effects. In the case of tri(dimethylamino)arsenic (TDMAs) as the group-V precursor, recombination desorption of surface arsenic atoms from TDMAs decomposition is the process freeing up surface sites from group-V-related species' occupation. In the case of P₂ as the phosphorous precursor, recombination desorption of surface phosphorous atoms should be the process controlling the coverage of adsorbed phosphorous atoms. It is well known that phosphorous is more evaporative than arsenic. Therefore, for a group-V species which has a shorter surface residence time, the low end of the growth-enhancement temperature window moves to a lower temperature, consistent with the findings in Chapter 6. The gradual increase in the growth rate enhancement with temperature in region I of Fig. 9.3 may mainly correspond to further evaporation of adsorbed phosphorous. Growth enhancement in region II may be the sum of photo-decomposition and laser-induced thermal decomposition of TMIn-related species. Thermal decomposition becomes dominant in region III, and the effect of laser consequently decreases.

Fig. 9.6 shows room-temperature photoluminescence (PL) spectra of samples grown at different temperatures. The thickness of the laser-irradiated part of the 370 °C sample is 0.95 μm, while those of the 420 °C and 450 °C samples are 2.35 μm and 2.4 μm, respectively. The nonirradiated parts of the three samples are of 0.22 μm, 2.11 μm and 2.3 μm thickness respectively. For the 370 °C sample, the crystalline quality of the epitaxial over-layer grown at the low temperature is poor enough that we did not detect any PL signal from the epitaxial over-layer and the substrate. With effects of diffusion of photogenerated carriers taken into account, the PL probing depth into a good crystal is on the order of 1 μm. We can see that the laser-irradiated layers produced higher PL intensities than the non-irradiated areas when the substrate temperature was not too high. The improved optical quality of the InP films grown at 370 °C and 420 °C is most likely due to reductions in the concentration of defect-related non-radiative centers because the growth temperatures were closer to the optimal in laser-irradiated areas. It is unlikely

due to enhanced impurity incorporation since carbon atoms, which are shallow donors in InP, are ionized at room temperature. The surface morphology degraded significantly when the film growth temperature was higher than 460 °C due to loss of phosphorous. The PL intensity of the irradiated area was lower than that of the non-irradiated area when the substrate temperature was around 450 °C because the temperature of the irradiated region must have been higher than 460°C.

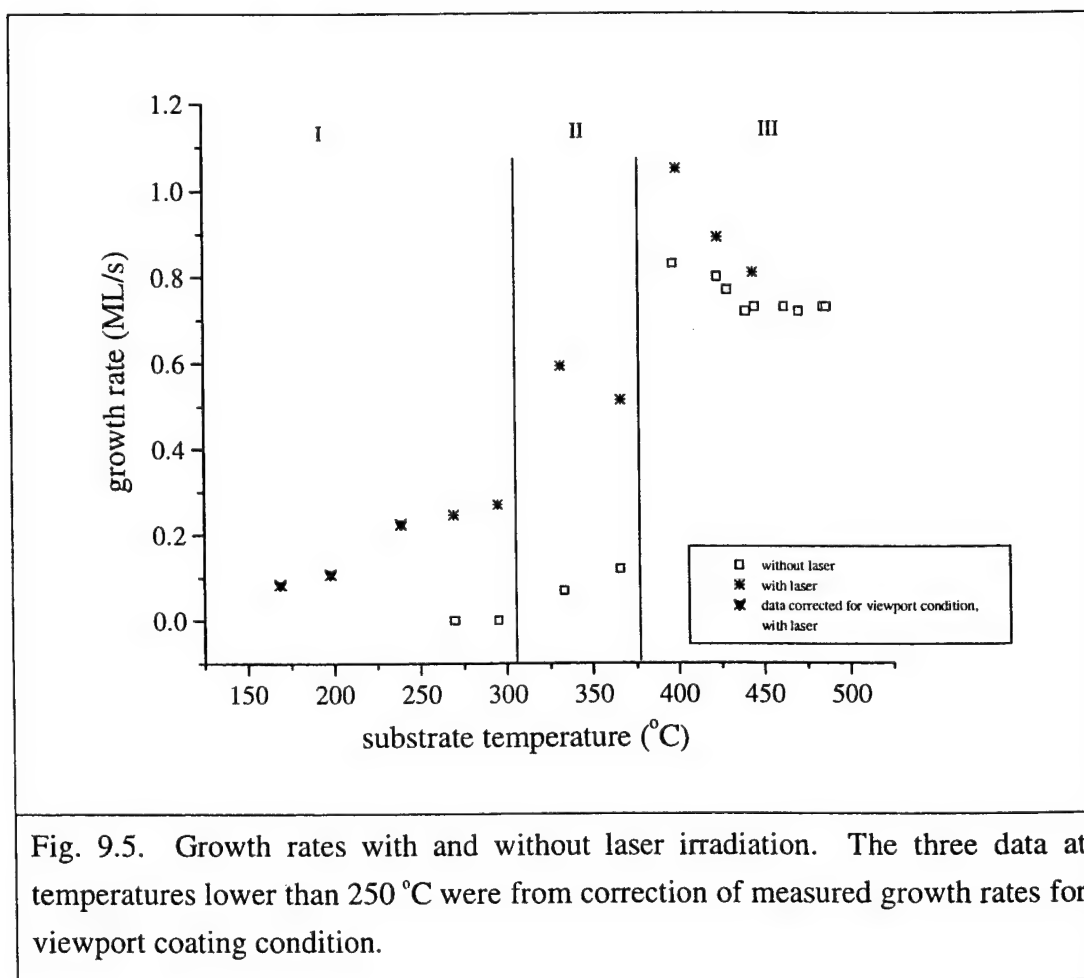
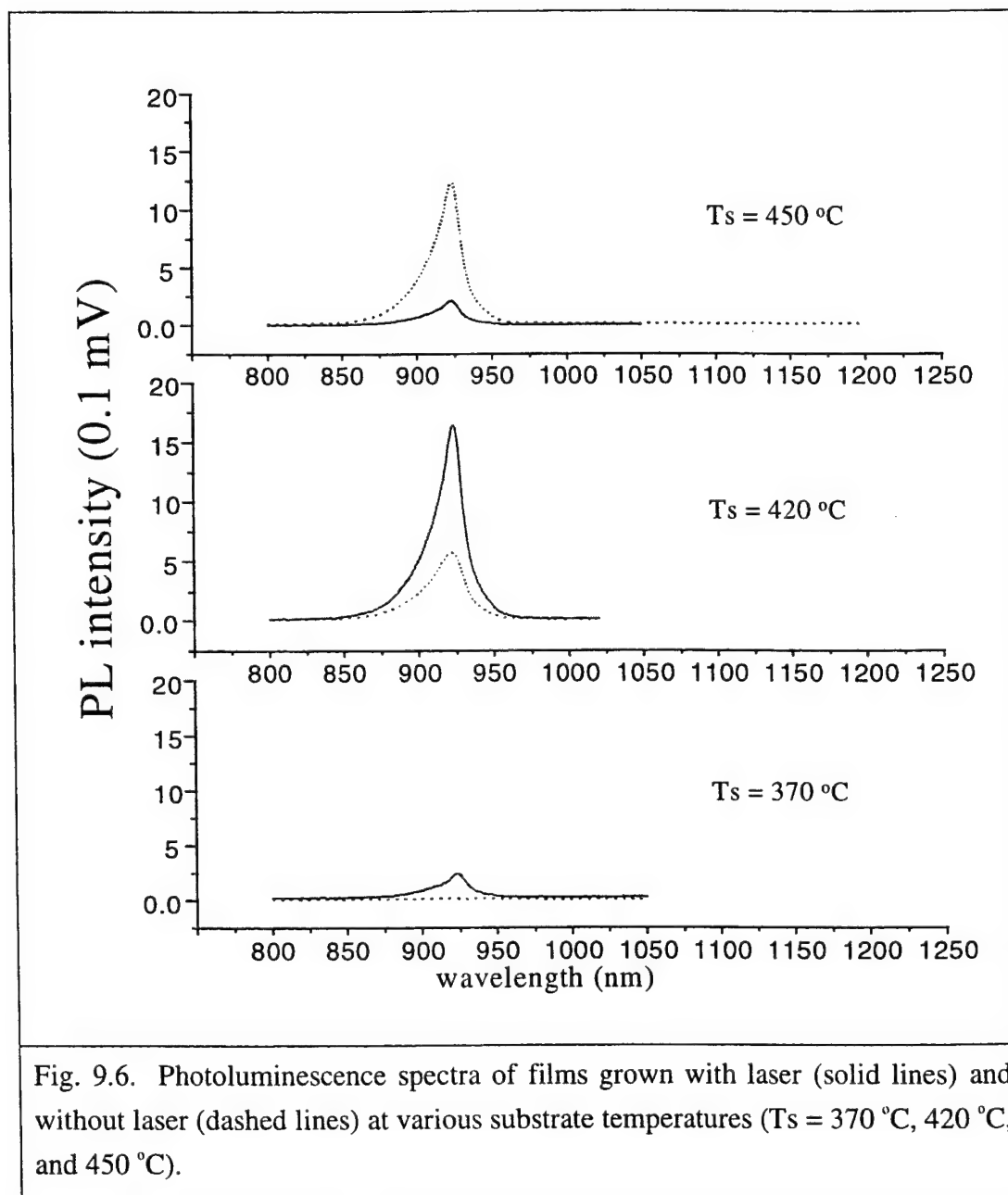


Fig. 9.7 shows typical X-ray rocking curves of the laser-irradiated and non-irradiated areas. Also shown is the X-ray rocking of an epi-ready InP substrate. The X-ray penetration depth is on the order of 10 μm . The peak signals indeed have a significant portion coming from the substrate. The diameter of the X-ray incident beam

for the measurement is approximately 1 mm, which is comparable to the sizes of laser-scanned areas. We do not see a broadening of the X-ray rocking curve of the laser-irradiated epitaxial layer in comparison to that of the non-irradiated, indicating that the crystalline qualities of these layers are comparable.



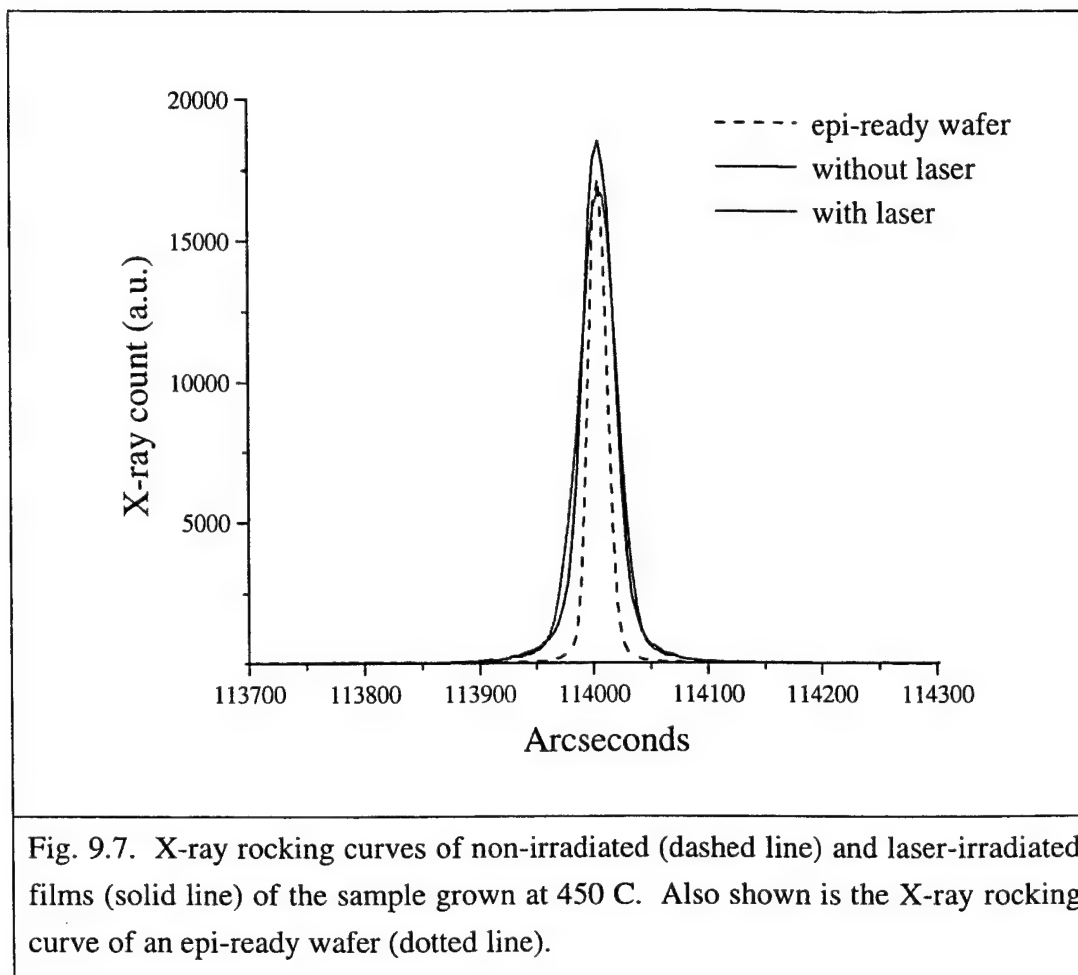


Fig. 9.7. X-ray rocking curves of non-irradiated (dashed line) and laser-irradiated films (solid line) of the sample grown at 450 C. Also shown is the X-ray rocking curve of an epi-ready wafer (dotted line).

9.3 Ar⁺-laser assisted CBE of GaInP

This section reports results from laser-assisted epitaxy of GaInP with TMIn, TEGa and TBP. The TEGa and TBP flow rates were maintained at 0.31 sccm and 5.8 sccm respectively, while the TMIn flow rate was adjusted when the substrate temperature was varied so that the ternary growth outside the laser-irradiated area was under the conditions for lattice match to the GaAs substrate. Substrate temperatures were measured using an infrared optical pyrometer which was calibrated by observing the appearance of 4x RHEED surface reconstruction patterns of a GaAs substrate upon thermal desorption of surface oxides at 580 °C. Double crystal rocking X-ray measurement was performed on the samples grown and their compositions were calculated based on the angular separation between the film and substrate X-ray peaks. Fig.9.8 shows typical X-ray

rocking curves of non-irradiated and irradiated films, respectively. In the calculation, the laser-irradiated films were assumed to be completely relaxed as evidenced by X-ray rocking curves and the Vegard's law was used to derive composition information. Films grown without laser irradiation were close to being lattice matched to substrates and therefore, were assumed to be coherently strained. An X-ray dynamic simulation program for coherently-strained films [9.8] was used to determine the compositions.

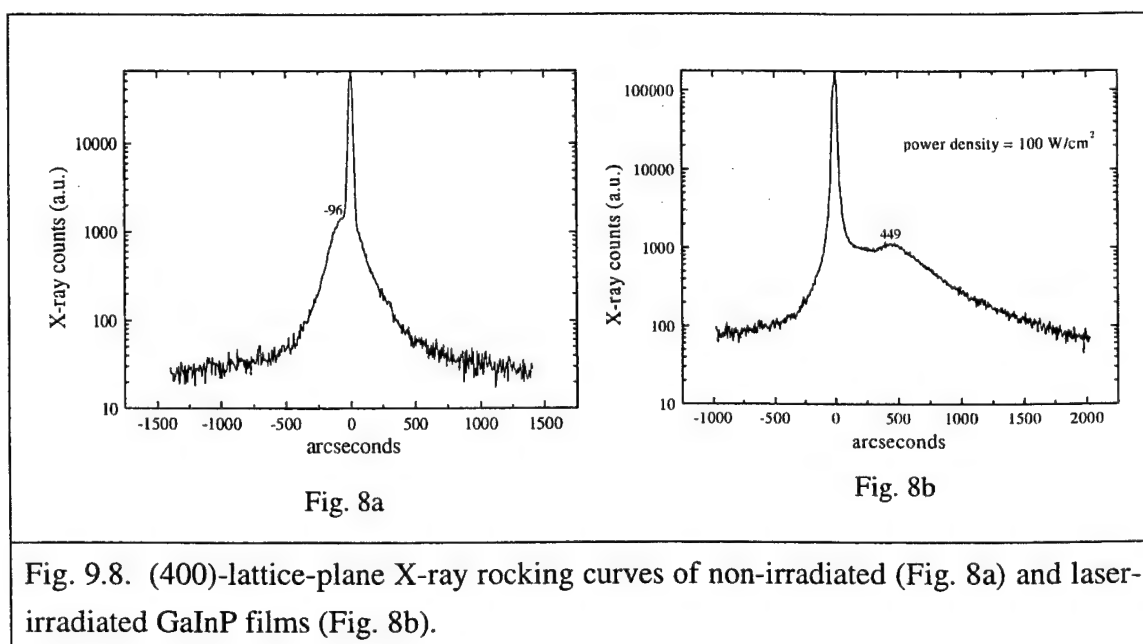


Fig. 9.9 shows the change in gallium composition resulted from 100 W/cm² laser irradiation. The change was larger at 400 °C. In Chapter 6 (Fig. 6.2), it is shown that the maximum photo-enhanced decomposition of TEGa occurs at around 400 °C, while Fig. 9.5 reveals that the photo-enhanced decomposition of TMIn is largest at around 335 °C. It is therefore not surprising to have a Ga-rich film of GaInP at 400 °C with laser irradiation. The change at 550 °C is larger than that at 500 °C, which may be attributed to laser-enhanced In evaporation at high temperatures.

The growth times for data of Fig. 9.9 were set such that GaInP films would be around 0.2 μm in thickness based on estimation of growth rates using RHEED-intensity

oscillations. In order to determine the thickness of the GaInP samples of Fig. 9.9 more accurately, the samples grown were patterned and etched in 100% HCl for 1 minute (HCl selectively etchs phosphides). Dektak stylus profile measurement was then performed on the processed films. Fig. 9.10 gives the growth rate information. The variation of the growth rate with the substrate temperature is of typical CBE characteristics, that is, low growth rates at low temperatures due to incomplete decomposition of precursors and decreasing growth rate with temperature at high growth temperatures because of increasing desorption of precursors and their decomposition products. Fig. 9.11 shows the ratio of the thickness enhancement resulted from laser irradiation to the thickness without laser irradiation. It appears that HCl cannot etch films from highly lattice-mismatched growth. We were not able to obtain the thickness of one of the two laser-irradiated films grown at 400 °C. For the other film, the surface morphology after etching was rough and the two 400 °C data points of Fig. 9.11 were calculated using the measured thickness at two randomly selected locations of the irradiated film. We were not able to obtain thickness data for the laser-irradiated film grown at 550 °C either. Nevertheless, we can see that thickness-enhancement ratios at other temperatures were small and comparable to the compositional changes in Fig. 9.9. This observation may be understood based on the assumption that the compositional change was mainly due to laser-enhanced TEGa decomposition. Because of small thickness-enhancement ratios, thick films ($\sim 5 \mu\text{m}$) would be desirable in order for us to determine the change in the growth rate accurately with the power density setting of this study. However, it is difficult to grow such thick GaInP because of the high growth pressure (and more precursor consumption) required for phosphide growth.

9.4 Summary

Ar⁺ laser assisted CBE of InP with trimethylindium and tertiarybutylphosphine has been carried out. A convenient procedure has also been established for intersecting the RHEED e-gun beam on the substrate surface with the laser beam. With this procedure, we were able to see the effects of laser irradiation on the surface reconstruction pattern. Temperature dependence of the normal growth rate has been

interpreted in terms of the chemistry in the chemisorbed layer of the chemical system being investigated. Specifically, the growth is determined by 1) TMIn decomposition through radicals formation, 2) number of free sites available in the presence of adsorbed phosphorous and methyl radicals, and 3) activation at various temperatures of desorption of chemisorbed radicals on the surface. Using a laser power density comparable to those used in studies reported in the literature by others, we have found reasonable growth enhancement at temperatures as low as 170 °C. Based on the findings from Chapter 6, the mechanisms responsible for observed growth modification by laser have been discussed in terms of laser-enhanced photolytic and pyrolytic decomposition of TMIn. The discussion involves the role of surface coverage of group-V species in controlling the amount of adsorbed group-III molecules at low growth temperatures. A physical picture which dictates the variation of growth enhancement with the substrate temperature has thus been presented. Photoluminescence measurement indicates that laser irradiation improves the optical quality of InP films when the growth temperature is not too high. X-ray characterization of both the laser and non-irradiated areas reveals a comparable structural perfection.

Laser-assisted GaInP growth resulted in Ga-rich films, which have been attributed to larger laser-enhanced decomposition of TEGa at low growth temperatures and higher desorption of In from growing surfaces associated with laser heating at high growth temperatures.

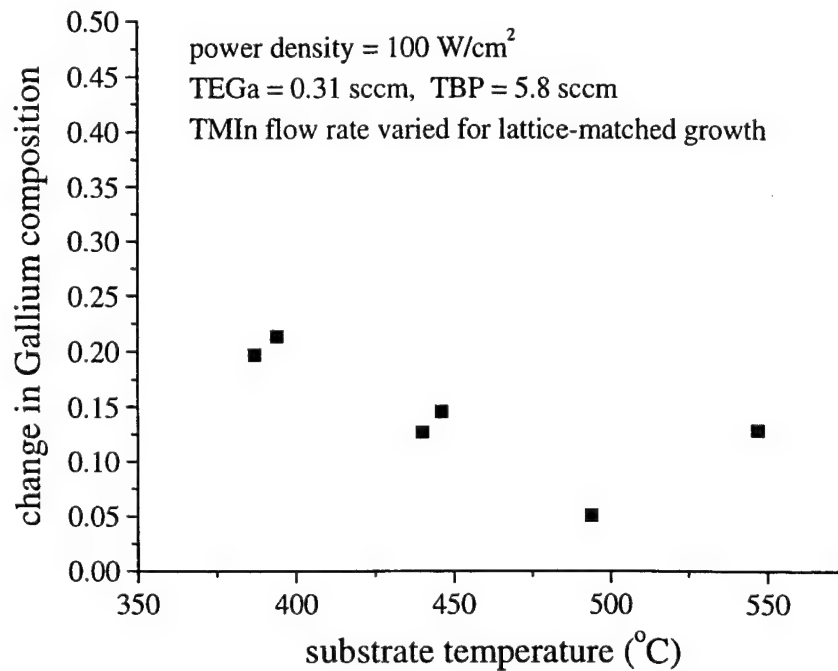


Fig. 9.9. Change in gallium composition of GaInP films resulted from laser irradiation at various substrate temperatures. The TMIn flow rate varies for different growth temperatures in order to obtain growth lattice matched to GaAs substrates outside of laser-irradiation areas..

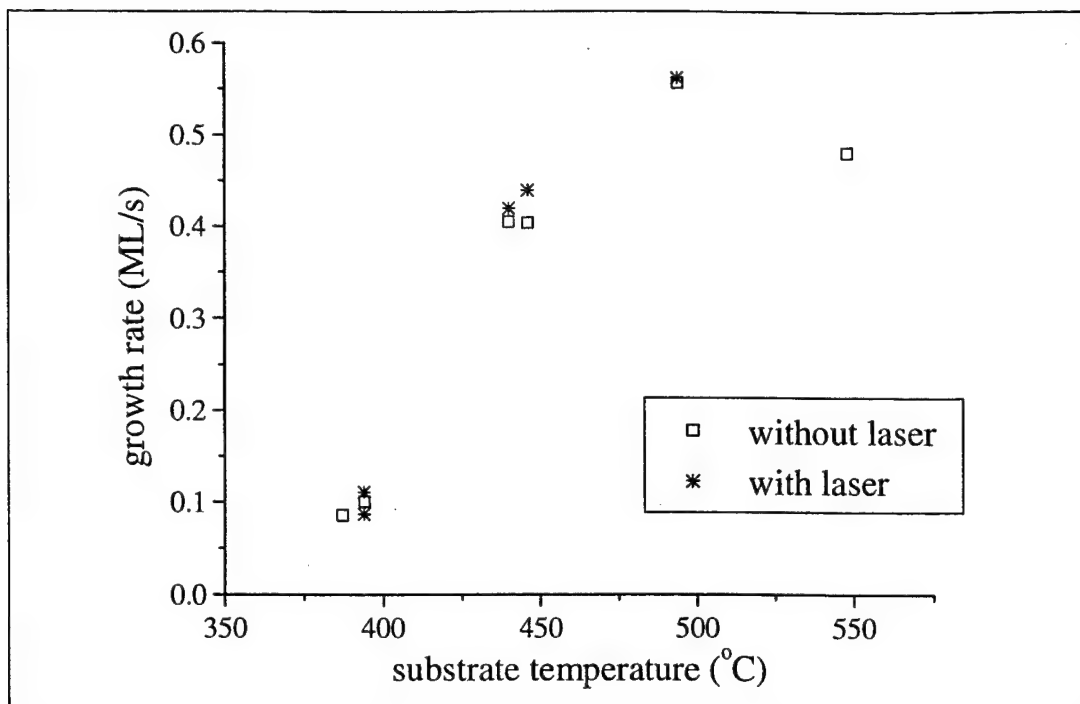


Fig. 9.10. Measured growth rate as a function of substrate temperature with laser (star) and without laser (open square) under growth conditions of Fig. 9.9.

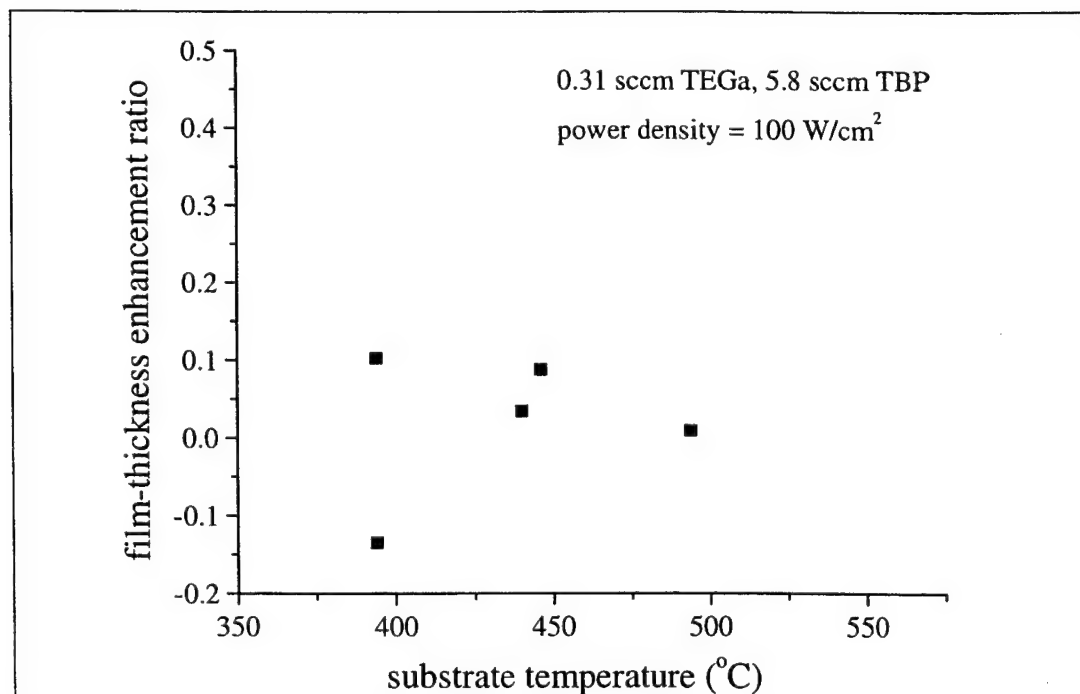


Fig. 9.11. Ratio of laser-induced thickness enhancement to thickness from normal growth. Growth conditions are the same as those of Fig. 9.9.

References

- [9.1] R. Iga, H. Sugiura and T. Yamada, *Jpn. J. Appl. Phys.* **29**, 475-478 (1990).
- [9.2] Y. Kawaguchi, H. Asahi and H. Nagai, *Inst. Phys. Conf. Ser. GaAs and Related Compounds* **79**, 79 (1985).
- [9.3] K. Nagata, Y. Iimura, Y. Aoyagi and S. Namba, *J. Crystal Growth* **95**, 142-144 (1989).
- [9.4] R. P. H. Gasser, *An introduction to chemisorption and catalysis by metals*, Clarendon Press, Oxford, Chapter 1 (1985).
- [9.5] A. Robertson Jr., T. H. Chiu, W. T. Tsang and J. E. Cunningham, *J. Appl. Phys.* **64**, 877-887 (1988).
- [9.6] B. W. Liang, *Ph. D thesis*, University of California, San Diego, California, Chapter 2 (1994).
- [9.7] H. K. Dong, *Ph. D thesis*, University of California, San Diego, California, Chapter 2 (1995).
- [9.8] H. Q. Hou, *Ph. D thesis*, University of California, San Diego, California, Chapter 3 (1993).

CHAPTER 10

ACCOMPLISHMENT SUMMARY AND RECOMMENDATIONS

10.1 Accomplishments

During the 3-year duration covered by this report, significant progresses were achieved on many aspects of laser-assisted CBE. In particular, a fundamental understanding of the mechanisms responsible for laser-induced growth and doping modifications was established. The major achievements are highlighted in the following:

- Developed a numerical model for simulating TEGa surface decomposition on GaAs (100). This model was one of key components of the growth model for quantitatively evaluating Ar⁺-laser induced pyrolytic effects and surface coverage of chemisorbed TEGa decomposition products which might undergo photo decomposition.
- Developed a numerical model for simulating TDMAAs surface decomposition on GaAs (100). This model was one of key components of the growth model for quantitatively examining group-V species' control of growth-enhancement temperature window.
- Developed a numerical growth model for simulating CBE of GaAs on GaAs (100) with TEGa and TDMAAs. This model was different from previous GaAs growth models in the literature in that it involved surface decomposition and interaction of two metalorganic species, each of which possesses complicated surface decomposition kinetics. Modeling practices of this model proved that properly combining decomposition reaction schemes of individual metalorganic species from surface-science studies enabled us to develop useful tools for understanding CBE growth phenomena including laser-induced growth modifications.
- Derived mathematical expressions and a numerical procedure for calculating laser-induced temperature rise efficiently. Such calculation yielded information on how to better simulate laser-induced pyrolytic effects. The numerical program for computing laser-induced temperature rise was deemed efficient and could be used to optimize

conditions for processing semiconductors with lasers and to couple with surface reaction models to assess the effects of laser heating on CBE growth and doping.

- Investigated the mechanisms responsible for laser-induced growth enhancement of GaAs using numerical models developed in this report. Photodecomposition of chemisorbed TEGa decomposition products, along with laser-induced temperature rise, was found to be responsible for observed Ar^+ -laser induced growth enhancements. Group-V species were found to control the growth-enhancement temperature window because of their site-blocking effects.
- Analyzed the behavior of surface decomposition of SiBr_4 for doping of GaAs by CBE and derived an analytical expression to be coupled with growth models for calculating the doping concentration. Such analyses enabled us to understand the limiting reaction steps leading to Si incorporation into the lattice and therefore, shed light on the mechanisms responsible for laser-induced doping enhancements.
- Performed laser-assisted doping experiment with SiBr_4 as the dopant precursor. Doping increases by as much as 70 times were observed. Simulation using numerical models developed for doping and growth of GaAs revealed that the observed carrier concentration enhancement could not be accounted for by laser-induced temperature rise alone. A photodecomposition reaction scheme was proposed for physisorbed SiBr_4 based on chemical-physics data reported in the literature.
- Performed an experimental study on laser-assisted CBE of InP with TMIIn and TBP. Results from this study supported the findings on the mechanisms responsible for laser-induced growth enhancements.
- Developed a procedure for intersecting the RHEED electron beam with a laser beam on InP substrate surfaces which enabled us to monitor, *in situ*, laser-assisted growth.
- Performed an experimental study on laser-assisted CBE of GaInP with TEGa, TMIIn and TBP. Results from this study revealed that laser-induced GaInP growth enhancements were consistent with those observed in laser-assisted CBE of GaAs and InP.

10.2 Recommendations

10.2.1 Ar⁺-Laser Assisted Epitaxial Growth of Multiple-Wavelength VCSELs

Due to their inherent single Fabry-Perot (FP) mode operation, VCSELs can be very useful for wavelength division multiplexing (WDM) systems. As demonstrated in this report, spatially varying growth rates can be induced by Ar⁺-laser irradiation of growing surfaces with metalorganic species as precursors. To fabricate multi-wavelength arrays with large wavelength spans and yet small physical sizes, we can, therefore, utilize Ar⁺-laser irradiation to create variations, on the plane of wafers, of the cavity length in vertical cavity structures. This approach should be very effective for making multi-wavelength VCSEL arrays for cost-effective WDM applications, since the growth sequence will be the same as that for making single-wavelength VCSELs except that laser irradiation is turned on while growing portions of the FP cavities.

10.2.2 Continued investigation on dopant precursors for laser-induced lateral doping modifications

In this report, it was demonstrated that we can use Ar⁺-laser irradiation to induce dramatic localized n-type doping enhancements. This technique can be used to define current injection areas of microelectronic and optoelectronic devices. Since lateral-doping variations can be induced during epitaxy by turning on lasers, the number of fabrication steps necessary for making devices can be reduced. For example, this technique can be used to create gain-guiding regions of broad-area light emitting diodes (LEDs).

It was found in this report that the doping enhancement is controlled by surface residence time and dissociative-chemisorption energy barrier of the dopant precursor used. We, therefore, can expect that dopants of large bond strengths and large molecular weights would allow large doping enhancements at normal growth temperatures. In this investigation, a survey of available Si and carbon containing precursors should be conducted and Ar⁺-laser assisted doping studies should be performed to confirm the

finding. The aim of such an investigation will be to find best dopant candidates to be used in laser-assisted metalorganic epitaxy for fabricating devices cost-effectively.

APPENDIX A

CHEMICAL BEAM EPITAXY OF AlAs USING NOVEL GROUP-V PRECURSORS

A1 Introduction

High-quality AlGaAs alloys and AlAs are important for GaAs-based optoelectronic devices. Many device structures contain strained active layers grown at moderate temperatures ($\sim 500^\circ\text{C}$). Thus, epitaxy on top of the active layers is desired to be carried out at moderate temperatures to avoid occurrence of strain relaxation in the active layers and to maintain the abrupt heterojunction interfaces. Growth of GaAs-based vertical-cavity surface-emitting lasers (VCSEL) with GaInNAs quaternaries as the active layers, for example, manifests this issue. Much research attention has recently been focused on the optical devices because of their promises for high-performance lasers operating at wavelengths ($1.3\ \mu\text{m}$ and $1.55\ \mu\text{m}$) suitable for optical fiber communication [A1-A3]. Because of the size difference between N and As atoms, there exist highly localized strains in the GaInNAs layers. Therefore, it is essential that the epitaxy of GaAs/AlAs distributed Bragg reflectors (DBR) following the growth of the GaInNAs layers not be performed at high temperatures.

Chemical beam epitaxy (CBE) utilizes enhanced decomposition of group-III metalorganic vapors on reactive surfaces of dangling bonds and is a technique designed for low and moderate growth temperatures ($< 650^\circ\text{C}$). This technique also offers advantages of *in situ* monitoring of growth surfaces with reflection high-energy electron diffraction (RHEED) and flexible control of flow rates of precursors. Furuhashi et al. [A4] published characterization results of $\text{Al}_x\text{Ga}_{1-x}\text{As}$ films ($x=0.1 - 0.2$) grown by CBE with triethylgallium (TEG), a solid source for arsenic (As_4) and three different Al sources (triethylaluminum (TEA), trimethylaluminum (TMA) and dimethylaluminum hydride (DMAH)). They reported that with TMA and DMAH, the hole concentration was more than $10^{18}\ \text{cm}^{-3}$ in the investigated substrate temperature range ($500 - 600^\circ\text{C}$), while with TEA, the hole concentration was $1.2 \times 10^{15}\ \text{cm}^{-3}$ and the mobility $117\ \text{cm}^2/\text{V}\cdot\text{s}$ at 550°C .

Benchimol et al. [A5] investigated composition dependence of the background doping level in $\text{Al}_x\text{Ga}_{1-x}\text{As}$ films grown by CBE at 600 °C - 650 °C using TEA, TEGa and As_4 . With x varying from 0.1 to 0.5, they observed an exponential dependence of hole concentration on x ($\sim 1 \times 10^{19} \text{ cm}^{-3}$ at $x=0.5$). Abernathy et al. [A6] compared impurity backgrounds in AlAs grown from either trimethylamine alane (TMAA) or dimethylethylamine alane (DMEAA) and cracked AsH_3 in the temperature range of 425 °C to 600 °C. In their studies, growth with TMAA at 500 °C produced materials with oxygen levels of $\sim 5 \times 10^{21} \text{ cm}^{-3}$ and carbon $\sim 1 \times 10^{19} \text{ cm}^{-3}$. When DMEAA was used, the carbon and oxygen levels were $\sim 5 \times 10^{17} \text{ cm}^{-3}$. It is well known that the greatest hazard involved in III-V epitaxy is the use of AsH_3 . The search for safer As-containing compounds has been an active area of CBE research [A7-A11]. To date, only tertiarybutylarsine (TBA) and tris(dimethylamino)arsenic (TDMAs) have been demonstrated to be safe liquid-source alternatives to gaseous arsine for III-V epitaxy of high-purity materials by CBE. TBA, however, is too thermally stable to allow for reasonable growth rates at temperatures lower than 525 °C [A8]. Ritter et al. [A8] reported successful growth of $\text{Ga}_{0.47}\text{In}_{0.53}\text{As}$ and GaAs by CBE using cracked TBA. As evidenced by the background carrier concentrations, mobilities and luminescence, the material obtained was of usefully high quality. TDMAs decomposition on GaAs(100) begins at ~ 300 °C [A11], and thus, it can be used for low temperature epitaxy without precracking. In a CBE study by Abernathy et al. [A12], $\text{Al}_{0.36}\text{Ga}_{0.64}\text{As}$ films were grown at 525 °C using TMAA, TEG, and TDMAs. Their results showed that TDMAs exhibited a unique carbon gettering mechanism which lowered the observed carbon concentration relative to that which could be achieved using similar flows of AsH_3 .

We report here CBE of AlAs with TMA and either TDMAs or cracked TBA. The use of TMAA and DMEAA for III-V epitaxy stems from the consideration that the amine saturated Al sources do not form Al-O species. However, the synthesis process of TMAA utilizes ether ($\text{R}_1\text{-O-R}_2$, where R_1 and R_2 are alkyl radicals). On AlAs growth surfaces which are very reactive, the ether can be decomposed resulting in the incorporation of unacceptably high levels of oxygen [A6]. Although DMEAA has been shown to produce dramatically lower oxygen levels in AlAs than TMAA, its chemical stability may recommend against use of this source [A6]. TMA, on the other hand, is

widely used in III-V metalorganic chemical vapor deposition (MOCVD). To address the possibility of presence of methoxides ($((\text{CH}_3)_{3-n}\text{Al}(\text{OCH}_3)_n$ ($n=1, 2$ and 3)), Maeda et al. [A13] demonstrated that highly purified TMA could be prepared by treating TMA with aluminum halides to reduce methoxides. There has been no report in the literature on using TMA to grow AlAs films by CBE because of expected high background carbon concentrations. The purposes of CBE of AlAs carried out in this study are for 1) looking into growth with TMA and novel group-V precursors and 2) investigating the feasibility of growing p-type GaAs/AlAs distributed Bragg reflectors for VCSELs by CBE at moderate growth temperatures. In particular, we have investigated, in the case with TDMAAs, the dependence of the growth rate and background carrier concentration on precursors' flow rates because it was found in this study that growth with TDMAAs produced AlAs films of much better crystal quality than that with TBA.

A2 Experimental methods

This study was carried out in a Perkin Elemer 425 MBE system, equipped with gas lines for metalorganic species and a 1600 l/s turbomolecular pump for the growth chamber. TMA (electronic grade, Air Products and Chemicals) was injected into the growth chamber directly using a mass-flow controller (MFC) downstream of the TMA bubbler. TBA (MOCVD grade, Epichem) was injected into a cracker which operated at around 750 °C during growth runs, while its flow was controlled by an MFC downstream of the TBA bubbler. TDMAAs (electronic grade, Morton) was carried by purified H_2 gas into the chamber, while the flow rate of the H_2 gas into the TDMAAs bubbler was adjusted with an MFC upstream of the TDMAAs bubbler. During a growth run, a semi-insulating epi-ready GaAs(100) substrate was first thermally cleaned under an over-pressure of cracked TBA. A GaAs buffer layer (~ 150 nm) was then grown on the substrate at 590 °C using TEG and cracked TBA prior to the growth of an AlAs film. Substrate temperatures were measured using an infrared optical pyrometer which was calibrated by observing the appearance of 4x RHEED surface reconstruction patterns of a substrate upon thermal desorption of surface oxides at 580 °C. We determined the TBA and TDMAAs absolute incident fluxes in terms of monolayers per second (ML/s) through

group-V induced RHEED-intensity oscillations. The maximum TDMAAs flux achievable during this study was 1.02 ML/s. The V/III incorporation ratio was varied from 1.8 to 6. Growth rates were derived from group-III induced RHEED intensity oscillations. Net carrier concentrations of the AlAs films grown were determined using the van der Pauw-Hall technique on cleaved $5 \times 5 \text{ mm}^2$ samples with Zn/In contacts.

A3 Results and discussion

Fig. A1 shows group-III (TMA) induced RHEED intensity oscillations at the (00) rod of the surface reconstruction on the (1 1 0) recording plane with 0.2 sccm TMA and cracked TBA or TDMAAs. The growth temperature was 510 °C. TBA or TDMAAs was on throughout the recording. The flow of H_2 carrier gas for TDMAAs was 3 sccm, which resulted in 0.95 ML/s absolute TDMAAs incident flux. The TBA flow was 1.4 sccm and it corresponded to 0.95 ML/s group-V induced growth rate. We can see that with cracked TBA, the amplitude of RHEED oscillations damped down more quickly than with TDMAAs, indicating that in the latter case, growth was more through layer-by-layer coalescence of two-dimensional AlAs islands and exhibited a better epitaxial manner. The growth rate derived from the oscillation curves were 0.15 ML/s and 0.17 ML/s, respectively, for TBA and TDMAAs.

To see the dependence of the RHEED behavior on the TMA flow rate, growth runs with 0.75 sccm TMA were carried out with the same growth temperature and group-V flow setups as those of Fig. A1. Fig. A2 shows the group-III induced RHEED oscillations recorded in the same way as Fig. A1. We can see that when TMA flow was increased, there were barely any oscillations with cracked TBA. The situation with TDMAAs was strikingly different, where oscillations lasted for the entire 45 seconds of recording. Fig. A3 displays the RHEED surface reconstruction patterns (upper row of pictures from use of TBA and lower row TDMAAs) on the (1 1 0) recording plane with the growth conditions of Fig. A2 as the growth proceeded. The change in the surface reconstruction pattern was dramatically different as the growth progressed. Even though the reconstruction patterns were similar prior to growth, streaks were almost gone at 1

minute with cracked TBA. An amorphous surface appeared at 6 minutes and remained throughout the rest of the growth. It was found experimentally that an amorphous surface also appeared minutes into a growth at 600 °C with the same TMA flow setting. With TDMAAs, RHEED was streaky after 101 nm (16 minutes) of AlAs growth, which is less than the critical thickness of AlAs on a GaAs substrate (144 nm) calculated using the Matthews-Blakeslee formulae [A14].

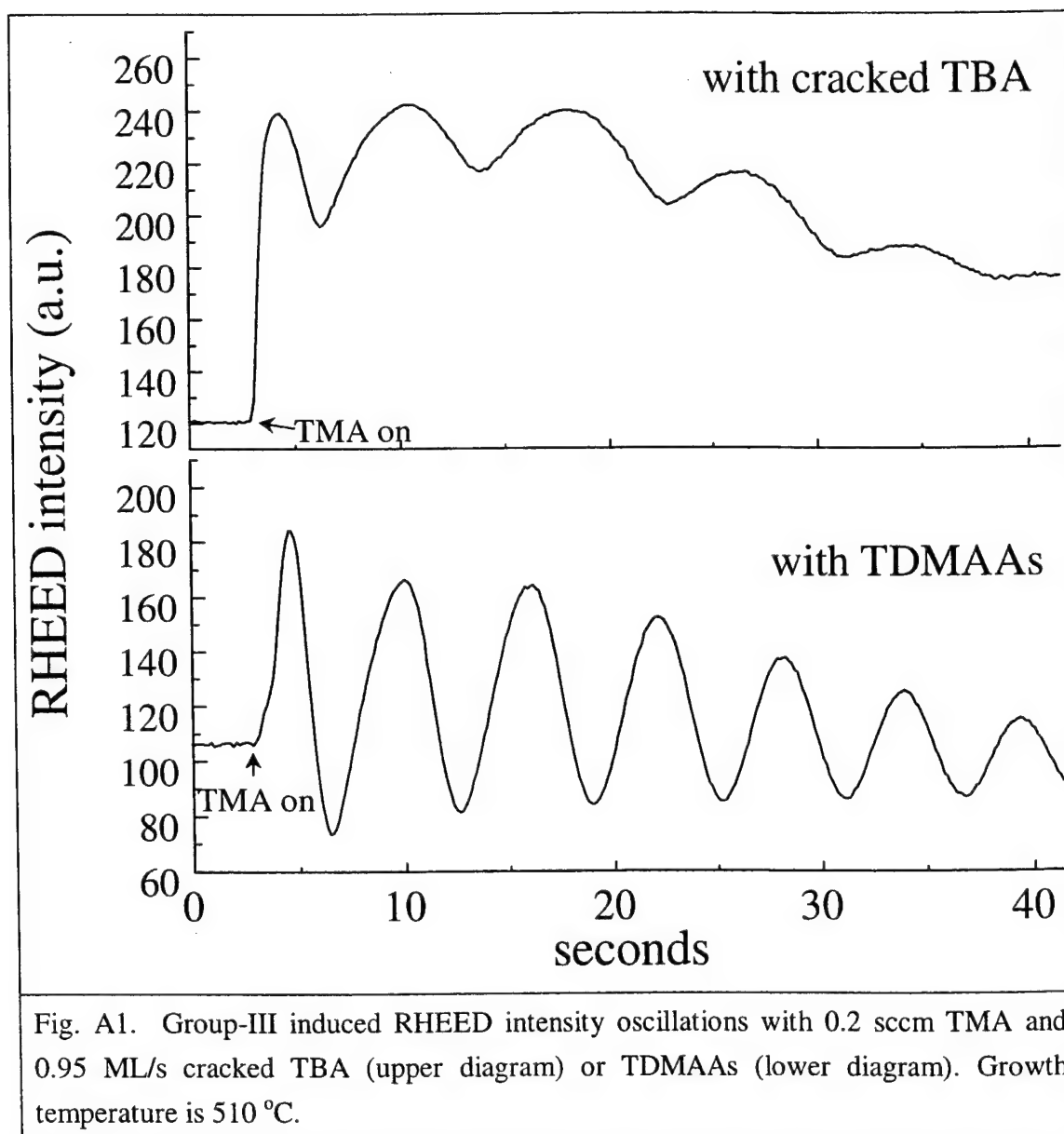
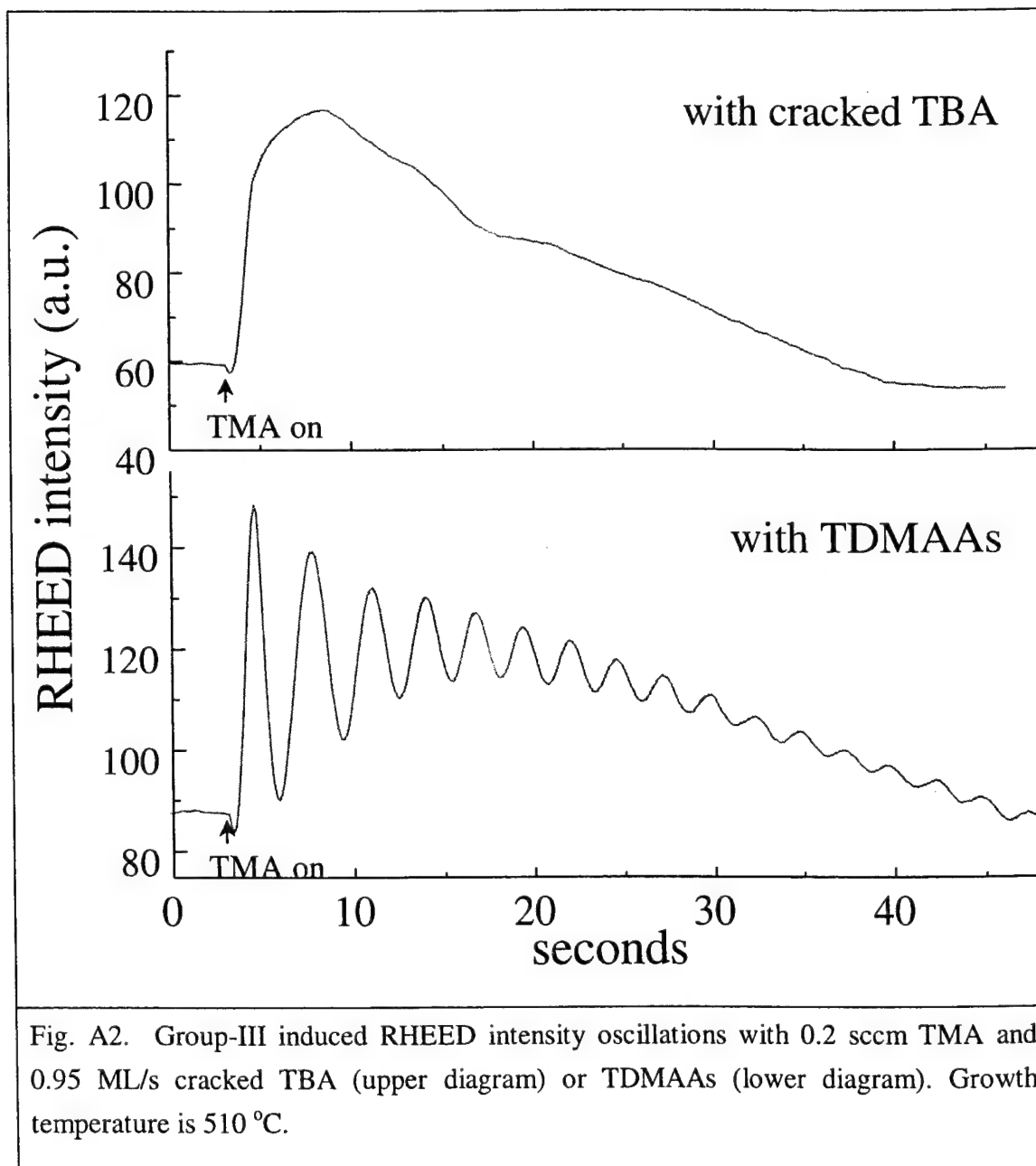


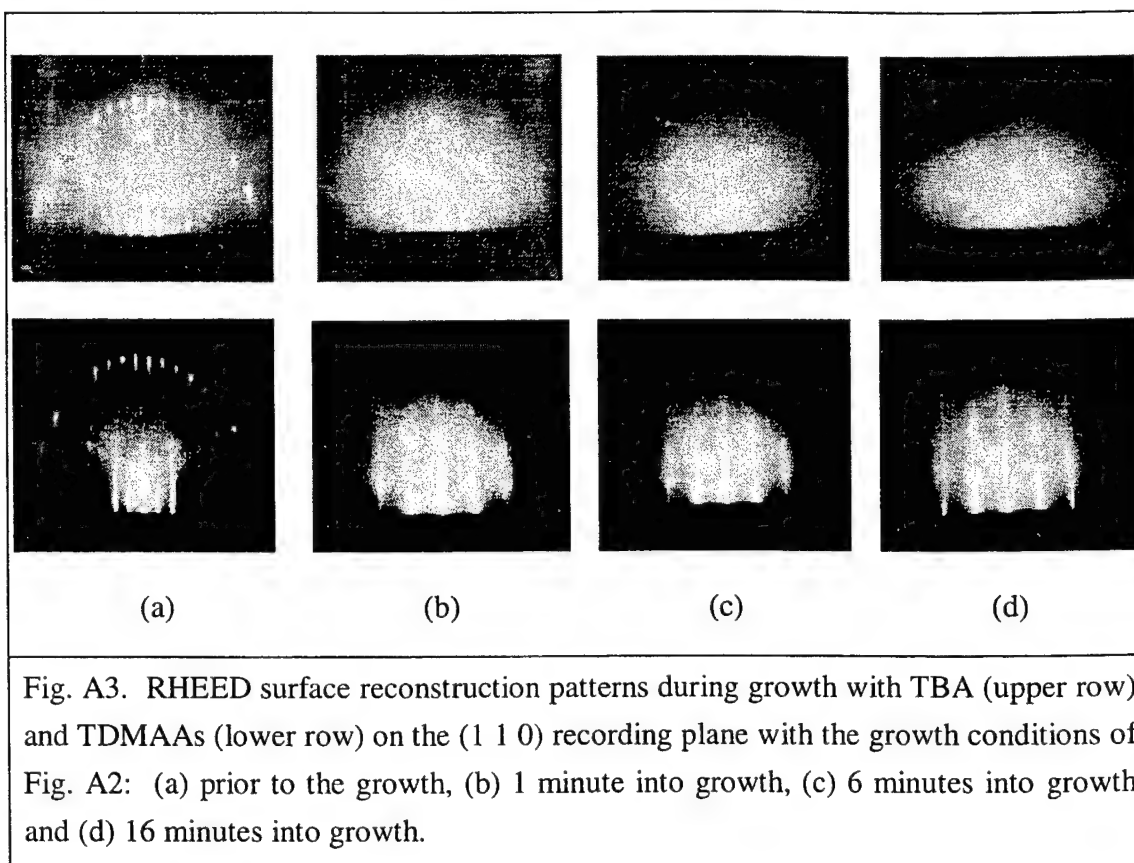
Fig. A1. Group-III induced RHEED intensity oscillations with 0.2 sccm TMA and 0.95 ML/s cracked TBA (upper diagram) or TDMAAs (lower diagram). Growth temperature is 510 °C.

The main decomposition products from cracking TBA are methane, hydrogen, arsenic dimers and possibly, arsenic tetramers [A8]. It seems unreasonable to attribute differences in the growth behavior presented above to the possibility of methane decomposition on reactive AlAs surfaces, since we found in one experiment that AlAs growth at 510 °C with TMA and As₄ from a heated solid arsenic exhibited RHEED behaviors similar to those with cracked TBA. Methyl radicals from TMA may leave a growth surface mainly through its evaporation process because they do not have β hydrogen atoms to transfer to the surface. It is likely that during AlAs growth with cracked TBA, excessive hydrocarbon radicals originating from TMA are trapped into films, due to the strong bonding between the methyl radicals and AlAs surfaces. Trapped hydrocarbon radicals may, in turn, disrupt normal epitaxial processes and result in rough growth surfaces or even materials of no crystal characteristics. Chemisorbed TDMAAs molecules, on the other hand, undergo hydrogen surface transfer reactions forming methylmethyleimine ($\text{CH}_3\text{N}=\text{CH}_2$) which leaves the growth surface immediately [A11]. It is estimated that each TDMAAs parent molecule can contribute, on average, approximately two surface hydrogen atoms at 510 °C [A11]. The fact that the surface reconstruction pattern remained streaky with TDMAAs may be due to H gettering of hydrocarbon radicals on the growing surface. Therefore, based on observations narrated above and discussion of this paragraph, TDMAAs appears to be more suitable for AlAs growth by CBE.

Fig. A4 plots the AlAs growth rate as a function of the TMA flow rate at 510 °C when TDMAAs was used. At this typical CBE growth temperature, the growth rate increased with the TMA flow rate when the flow rate was less than 0.95 sccm, reaching 0.45 ML/s at 0.95 sccm. At even higher flow rates, the site blocking effect due to chemisorbed intermediate decomposition products of TDMAAs and TMA might have played a role in lowering the growth rate. Fig. A5 shows the variation of the epitaxial growth rate with the absolute TDMAAs incident flux at 510 °C at two different TMA flow rates (0.75 sccm and 0.95 sccm). We can see that increasing the TDMAAs flow enhanced the growth rate and that this was especially the case with the larger TMA flow. This finding is in line with our discussion above that hydrogen atoms transferred from

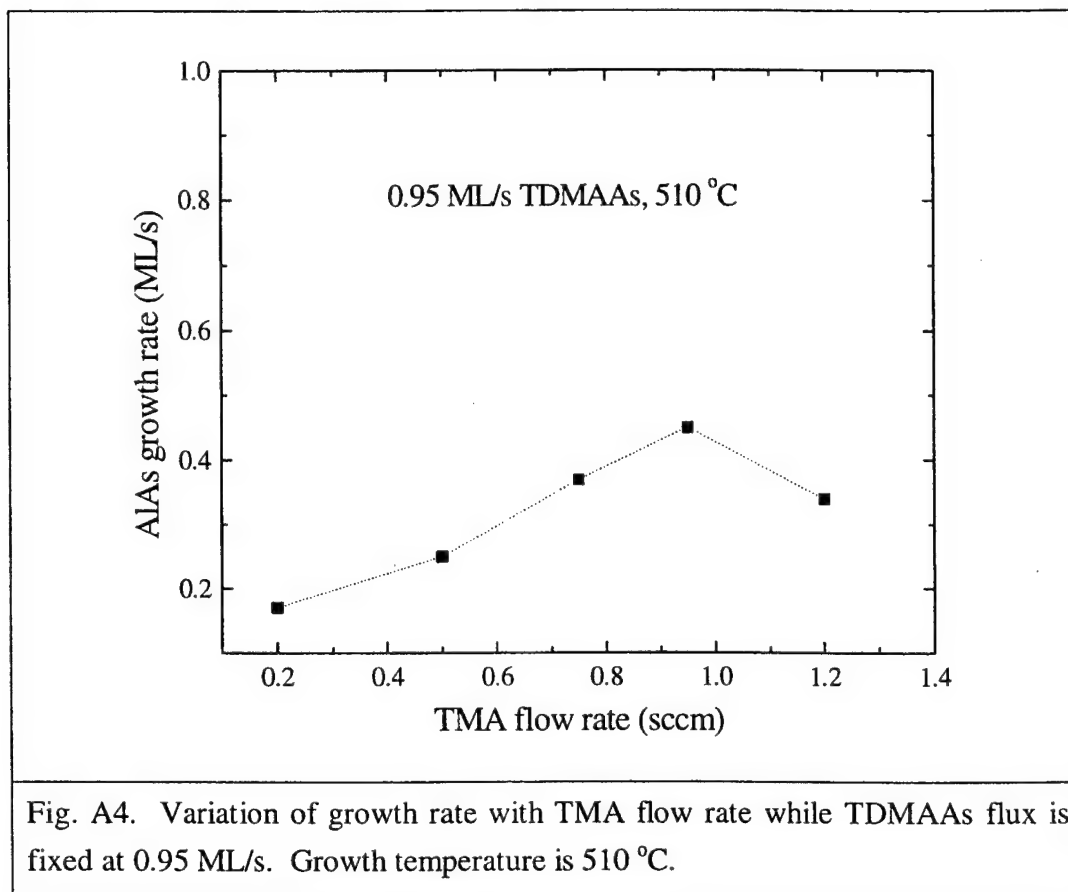
TDMAAs can getter hydrocarbon radicals from TMA and thus free up occupied surface sites for TMA decomposition. It is very likely that by increasing the TDMAAs incident flux further, even larger AIAs growth rates can be obtained. However, the small TDMAAs bubbler used in this study limited the maximum TDMAAs flux to 1.02 ML/s.





Van der Pauw-Hall measurement data of the films grown at 510 °C are plotted in Fig. A6. The TBA data point corresponds to the cracked-TBA sample of Fig. A1 (V/III incorporation ratio = 6.3). Hall measurement of the cracked-TBA sample of Fig. A3 revealed that the sample was not uniform for Hall voltage calculation, indicating that the film was a material of little crystal characteristics in consistence with the RHEED observation. In Fig. A6, the V/III incorporation ratio and the growth rate for each sample grown with TDMAAs are recorded right next to the corresponding data point with the V/III ratio in a bracket. The background carbon concentration depends both on the surface concentration of carbon-containing radicals and the growth rate. Therefore, it is, in principal, a nonlinear function of TMA and TDMAAs incident fluxes. But the data seem indicating that at an approximately same growth rate, the higher the V/III ratio is, the lower the background carbon concentration. This observation is consistent with the fact, as discussed above, that TDMAAs surface decomposition can undergo hydrogen

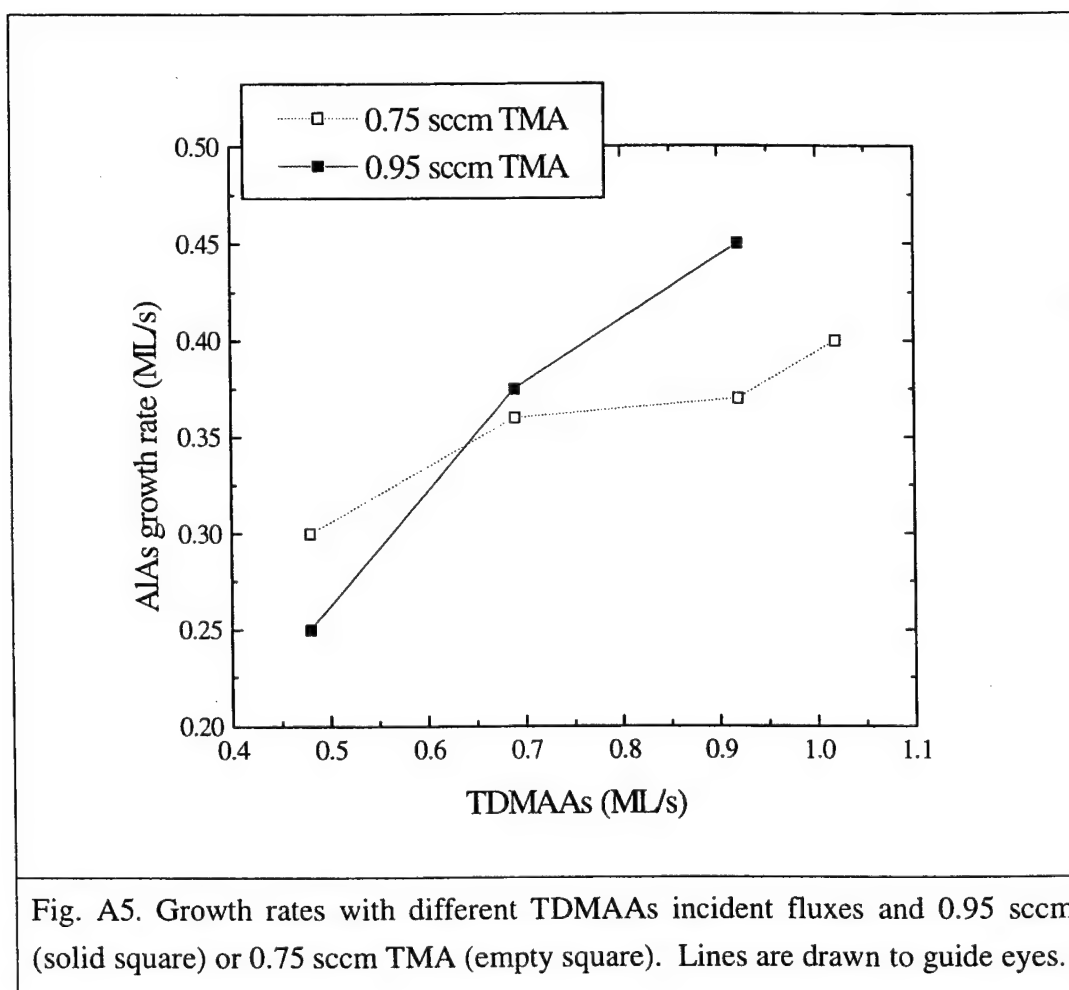
transfer reactions and surface hydrogen atoms can getter carbon-containing radicals on a growing surface and thus, effectively lower the background carbon concentration.

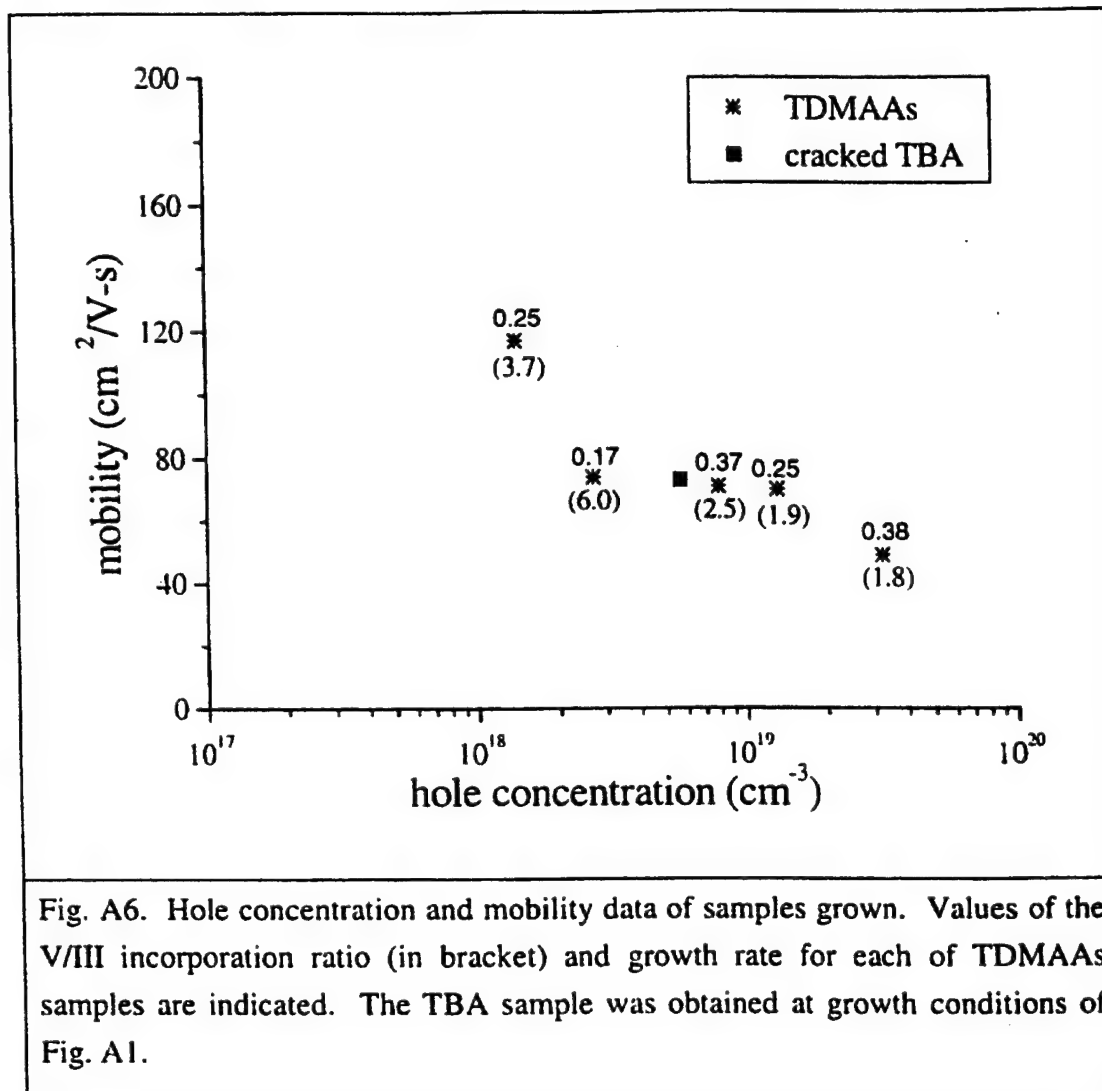


A4 Summary

We have investigated chemical beam epitaxy of AlAs films with novel group-V precursors, namely, tertiarybutylarsine and tris(dimethylamino)arsenic. Growth with cracked TBA, as revealed by observation using RHEED, resulted in rough growth surfaces and poor crystalline quality. With TDMAAs, RHEED patterns remained streaky when AlAs film thickness did not exceed the Matthews-Blakeslee critical thickness. We have related findings from RHEED observations to CBE growth surface chemistry involving inefficient desorption of methyl radicals on the surface and hydrogen atom

gettering of hydrocarbon radicals with presence of TDMAAs. Growth rate variation of AlAs with the temperature has been found to be of typical CBE characteristics, that is, lowering of the growth rate at high group-III flow rates. It has also been shown in this study that the AlAs growth rate increases with increasing absolute TDMAAs incident flux. Variation of the background hole concentration with growth conditions has also been looked into. It is concluded in this study that it is feasible to grow p-type GaAs/AlAs distributed Bragg reflectors at moderate growth temperatures by CBE with TDMAAs and TMA as precursors.





References

- [A1] M. Kondow, K. Shinoda, K. Uomi, and S. Nishimura, *Vertical cavity surface emitting laser; optical transmitter-receiver module using the laser; and parallel processing system using the laser*, US patent application No. 08-769789.
- [A2] K. Iga and M. Kondow, in: *8th Conf. Indium Phosphide and Related Materials*, Institute of Electrical and Electronics Engineers, Piscataway, New Jersey, ThA1-1 (1996).
- [A3] M.C. Larson, M. Kondow, T. Kitatani, K. Nakahara, K. Tamura, H. Inoue, and K. Uomi, *IEEE Photonics Technology Lett.* **10**, 188 (1998).
- [A4] N. Furuhashi, A. Okamoto and H. Hoshino, *J. Cryst. Growth* **102**, 814 (1990).
- [A5] J.L. Benchimol, F. Alexandre, Y. Gao and F. Alaoui, *J. Cryst. Growth* **95**, 150 (1989).
- [A6] C.R. Abernathy and P.W. Wisk, *Solid-State Electronics* **38**, 737 (1995).
- [A7] G.J. Davies, H.D. Shih, and W.T. Tsang, Eds., Proc. Of the Second Inter. Conf. On CBE, *J. Cryst. Growth* **105**, 1 (1990).
- [A8] D. Ritter, M.B. Panish, R.A. Hamm, D. Gershoni, and I. Brener, *Appl. Phys. Lett.* **56**, 1448 (1990).
- [A9] C.R. Abernathy, P.W. Wisk, S.J. Pearton, F. Ren, D.A. Bohling, and G.T. Muhr, *Mater. Res. Soc. Symp. Proc.* **3**, 240 (1992).
- [A10] C.R. Abernathy, P.W. Wisk, S.J. Pearton, F. Ren, D.A. Bohling and G.T. Muhr, *J. Crystal Growth* **124**, 64 (1992).
- [A11] B.Q. Shi and C.W. Tu, *J. Electr. Mat.* **28**, No. 1, 43 (1999).
- [A12] C.R. Abernathy, P.W. Wisk, D.A. Bohling and G.T. Muhr, *Appl. Phys. Lett.* **60** 2421 (1992).
- [A13] T. Maeda, M. Hata, M. Isemura and T. Yako, *Appl. Organometallic Chem.* **5**, 319 (1991).
- [A14] J.W. Matthews and A.E. Blakeslee, *J. Crystal Growth* **27**, 118 (1974).

APPENDIX B

EFFECTS OF Ar⁺ LASER AND HYDROGEN ATOMS ON CARBON DOPING OF GaAs WITH CBr₄

B1 Introduction

In Chapter 8, Ar⁺-laser-assisted Si doping of GaAs with SiBr₄ was explored experimentally and theoretically for better achieving localized n-type doping enhancements. Carbon is a shallow acceptor (ionization energy ~ 26 meV) in GaAs, i.e., carbon being incorporated on an As site [B.1]. Carbon has received much attention as an intentional impurity, particularly in GaAs and Al_xGa_{1-x}As, due to its very low reported diffusion coefficient [B.2]. A preliminary investigation on Ar⁺-laser-assisted C doping of GaAs with carbon tetrabromide (CBr₄) for p-type doping enhancements will be reported in this appendix. CBr₄ was used here because it had been demonstrated to be a very efficient dopant precursor and suitable for applications in gas-source molecular beam epitaxy [B.3].

There have been reports [B.4-B.6] in the literature on the finding that H atoms on a growing surface can getter alkyl radicals on the surface. Experimental runs with use of a home-made H₂ cracker are carried out to look into whether surface H atoms can also getter intermediate products from CBr₄ surface decomposition and the results are also reported here.

B2 Experimental methods

The experimental setup and the gas-manifold configuration for the dopant precursor were the same as those used for the Si doping studies in Chapters 7 and 8. All growth runs were carried out with 0.3 sccm TEGa and a H₂ flow into the TDMAAs bubbler yielding 0.95 ML/s TDMAAs. In addition, the leak-valve setting for CBr₄ was 35 and the pressure upstream of and adjacent to the leak valve 1 Torr for all growth runs. Substrate temperatures were measured using an infrared optical pyrometer which was

calibrated by observing the appearance of 4x RHEED surface reconstruction patterns of a GaAs substrate upon thermal desorption of surface oxides at 580 °C.

Since hydrogen atoms are present on growing surfaces in CBE and MOCVD, it should be interesting to assess the effects of hydrogen atoms on carbon doping. A home-made hydrogen-gas cracker was used to conduct such an assessment. It is a well-established fact (B.7-B.8) that when a tungsten filament is heated to a sufficiently high temperature (> 1000 °C) in hydrogen gas, atomic hydrogen can be produced. The production is due to catalytic reactions of hydrogen molecules on the tungsten surface. Such surface catalytic reactions are, in essence, associated with lowering of dissociation energy of the molecules with presence of tungsten surface dangling bonds. The home-made cracker consists of a coil of tungsten (0.25 mm in diameter, 4N5 grade, ESPI, Inc.) and radiation shields. The tungsten filament is resistively heated and the cracker operation condition is in terms of power supplied to heat the filament. Hydrogen radicals have been shown to be very effective at removing native oxides from the surface of GaAs substrates even at sample temperatures as low as 200 °C (B.9-B.10). To prove that the home-made cracker works, an experimental run for testing H cleaning of the epi-ready GaAs substrate was carried out at 400 °C substrate temperature. Fig. B.1 shows recorded observation of surface-reconstruction RHEED patterns during the run. B.1a is the pattern with the shutter for the cracker port open and the cracker at 270 W operation power for 15 minutes without H_2 flowing into the cracker. It is clear that the surface remained amorphous because of native surface oxides of GaAs. After introduction of 2 sccm H_2 into the cracker for 15 minutes, streaky RHEED patterns appeared as a result of H-atom removal of the oxides. Figs. B.1b and B.1c are the surface-reconstruction RHEED patterns on (1 -1 0) and (1 1 0) recording planes, respectively, at 15 minutes into H irradiation of the surface.

B3 Results and discussion

Fig. B.2 plots hole concentrations from Hall measurement at various substrate temperatures with and without introduction of H atoms onto growing surfaces. The H_2

flow and cracker power were the same as those for obtaining Fig. B.1 pictures. We can see that there existed noticeable changes in the doping concentration but the changes were small. The data seem to be indicating that H atoms may assist CBr_4 decomposition at low substrate temperatures and increase doping concentrations, while they may getter CBr_4 decomposition products at high substrate temperatures and effectively lower the doping concentration.

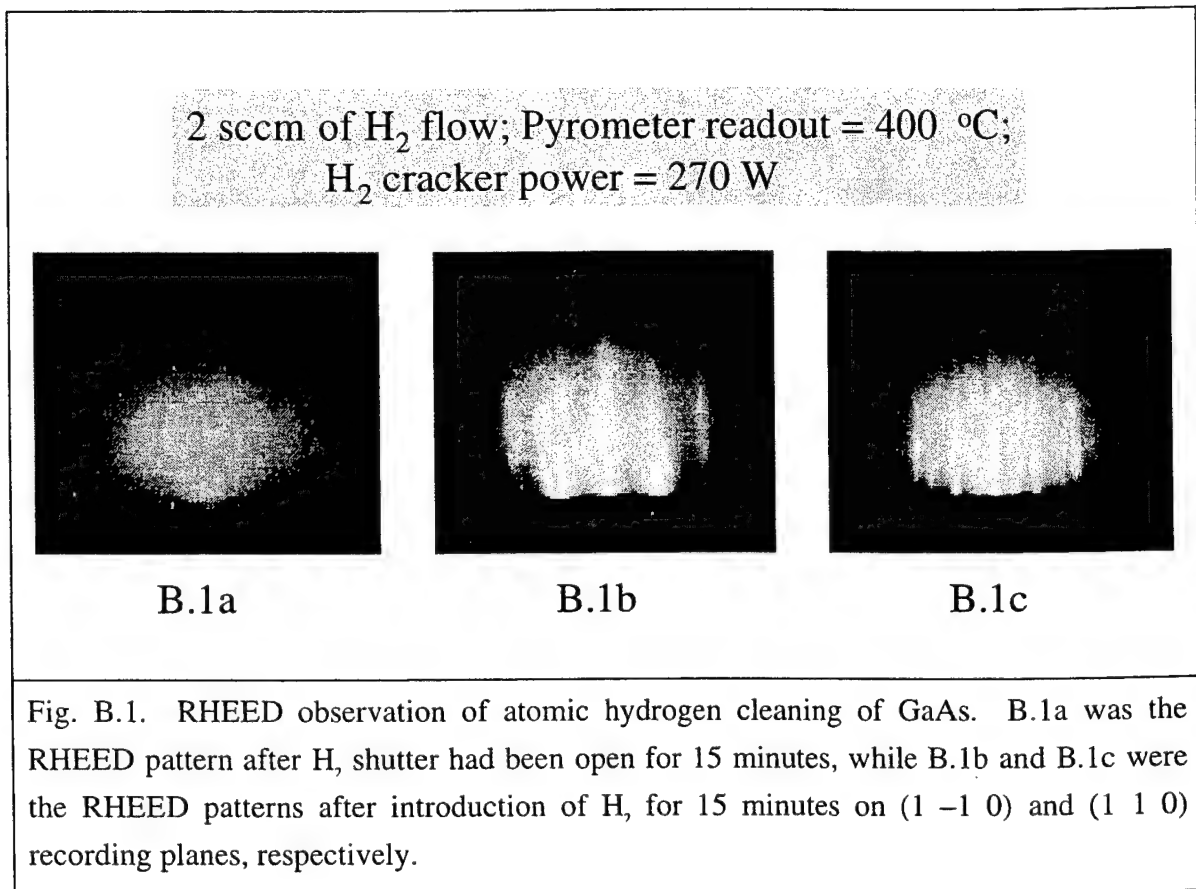
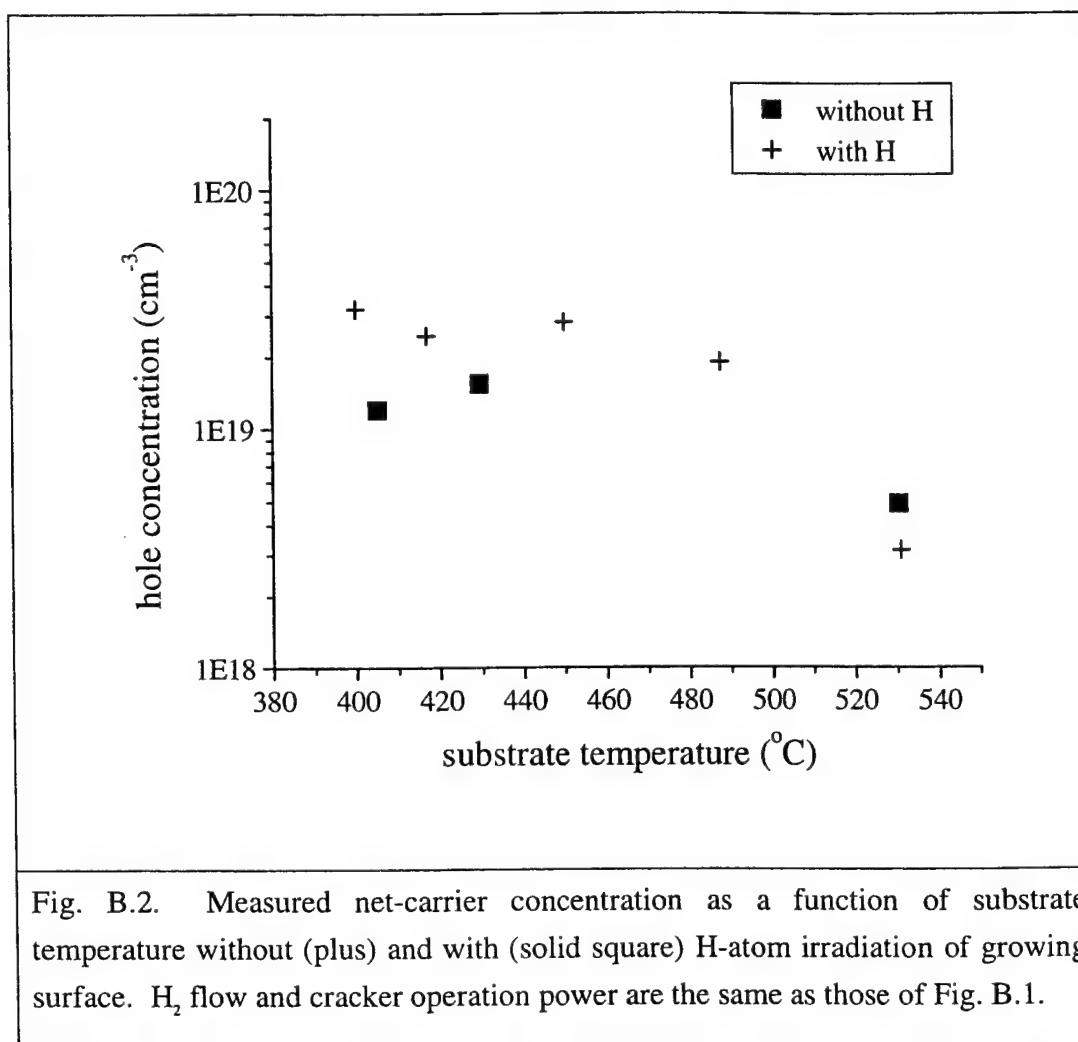


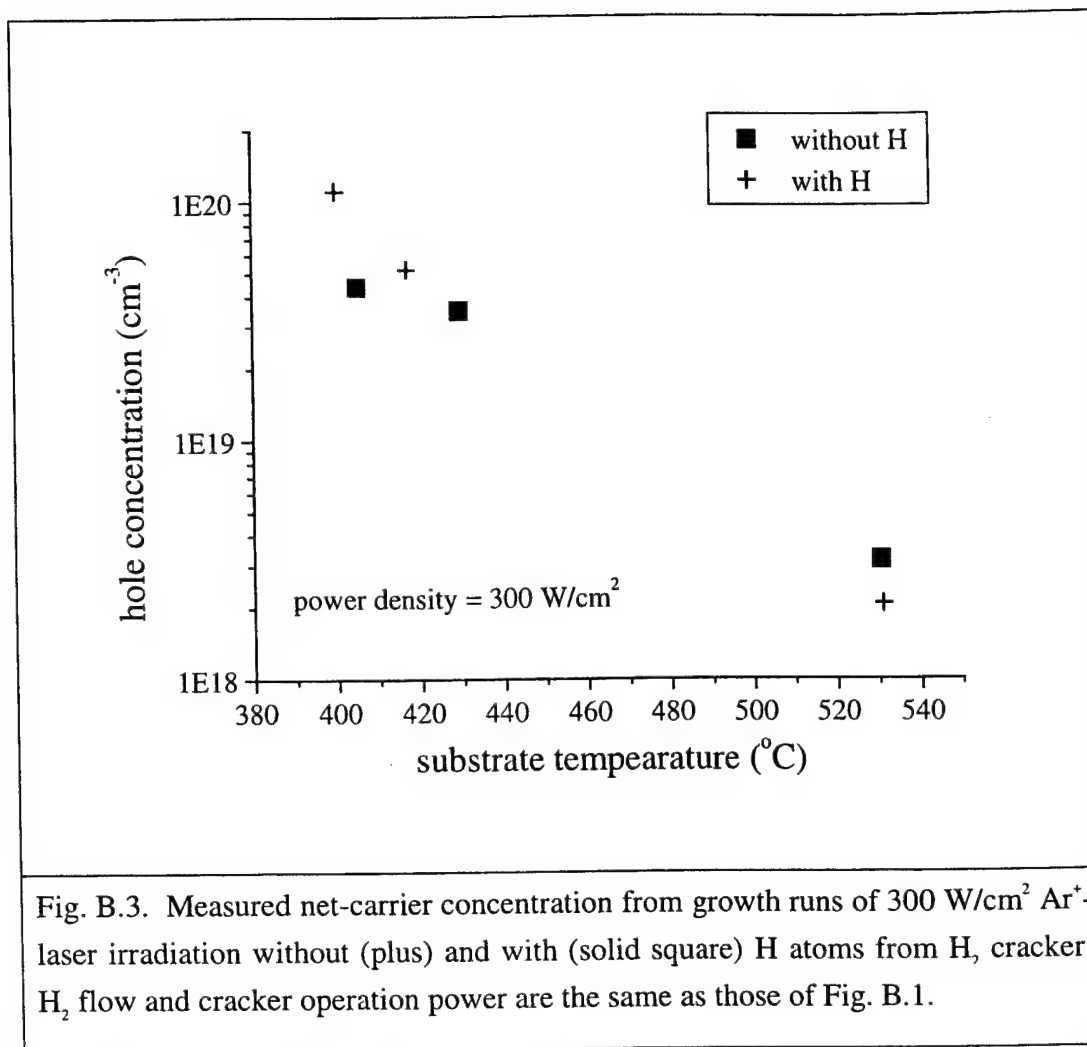
Fig. B.3 shows Hall-measurement data of samples under the same growth conditions as those of Fig. B.2 except that the Ar^+ laser was on for all the growth runs of Fig. B.3. The laser-irradiation power was 300 W/cm^2 . We can see from Fig. B.3 similar effects of H-atom irradiation on the doping concentration to those revealed in Fig. B.2. We can also see that the doping concentration is several times higher with laser

irradiation than without laser irradiation at low growth temperatures, while the opposite behavior is observed at high growth temperatures. One plausible explanation is that H-atom irradiation plays a similar role to photon irradiation, that is, it enhances CBr_4 decomposition at low temperatures and lowers surface populations of CBr_4 decomposition products at high temperatures. The mechanisms responsible for the similar high-temperature effects may be different though: laser irradiation may enhance desorption of those intermediate decomposition products because of laser-induced temperature rise, while H atoms may affect the surface populations of those products through recombination reactions. Fig. B.4 gives mobility data of the samples the net concentrations of which are plotted in Figs. B.2 and B.3. Also shown there is the variation of mobility as a function of the hole concentration calculated using Hilsum's empirical formulae [B.11]. The electronic characteristics of the samples are evidently comparable.

B4 Summary

In line with the investigation of Chapter 8, Ar^+ -laser and/or H-atom assisted p-type doping of GaAs by CBE is reported here. Assisted p-type doping of GaAs with CBr_4 reveals that the effects of Ar^+ -laser and/or H-atom irradiation are overall small. Experimental data also seem to be indicating that H atoms may actually assist in decomposition of the precursor at low growth temperatures, while it may getter carbon radicals at high growth temperatures.





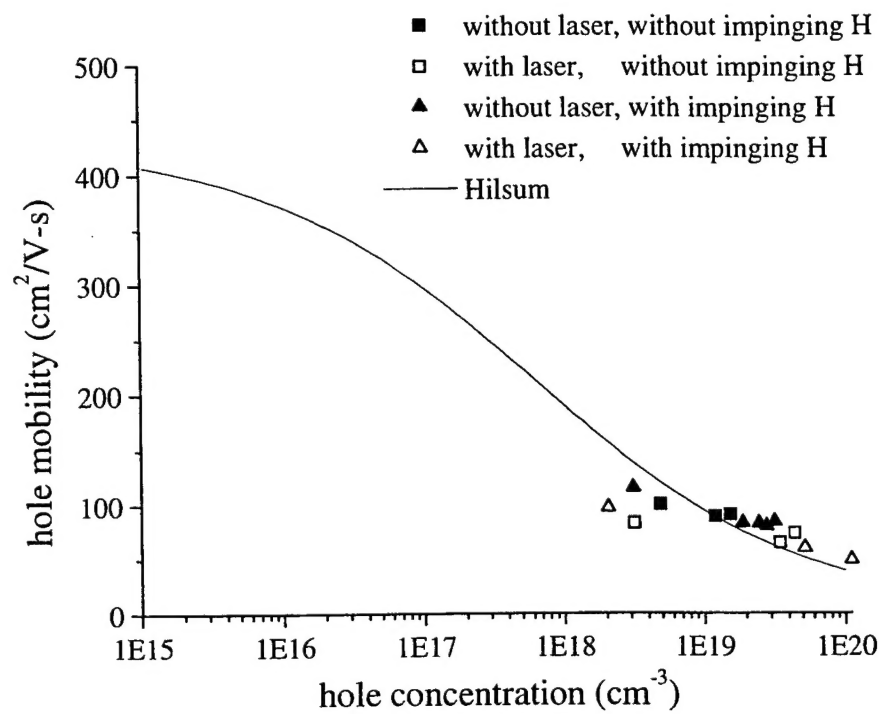


Fig. B.4. Measured mobility of the samples for which the carrier concentrations are plotted in Figs. B.2 and B.3.

References

- [B.1] W. M. Theis, K. K. Bajaj, C. W. Litton and W. G. Spitzer, Appl. Phys. Letters **41**, 70 (1982).
- [B.2] B. T. Cunningham, L. J. Guido, J. E. Baker, J. S. Major, Jr., N. Holonyak, Jr. and G. E. Stillman, Appl. Phys. Letters **55**, 687 (1989).
- [B.3] N. Y. Li, *Ph. D thesis*, University of California, San Diego, California, Chapter 2 (1997).
- [B.4] C. R. Abernathy, P. W. Wisk, S. J. Pearton, F. Ren, D. A. Bohling and G. T. Muhr, J. Crystal Growth **124**, 64 (1992).
- [B.5] B. Q. Shi and C. W. Tu, J. Electr. Mat. **28**, 43 (1999).
- [B.6] C. R. Abernathy, P. W. Wisk, D. A. Bohling and G. T. Muhr, Appl. Phys. Lett. **60**, 2421 (1992).
- [B.7] A. R. Miller, *The adsorption of gases on solids*, the University Press, Cambridge, Great Britain, Chapter 5 (1949).
- [B.8] A. Sutoh, Y. Okada, S. Ohta and M. Kawabe, Jpn. J. Appl. Phys. **34**, L1379-L1382 (1995).
- [B.9] T. Sugaya and M. Kawabe, Jpn. J. Appl. Phys. **30**, No. 3A, L402-404 (1991).
- [B.10] C. R. Abernathy, *Materials Science Forum Vols. 148-149*, 3-26 (1994).
- [B.11] C. Hilsum, *Electron. Lett.*, **10**, 259-260 (1974).

APPENDIX C

PUBLICATIONS AND PRESENTATIONS

C1 Publications

B. Q. Shi and C. W. Tu, "Evaluation of temperature rise on semiconductor surfaces associated with scanning Ar⁺ lasers", submitted to J. Crystal Growth (1999).

B. Q. Shi and C. W. Tu, "Experimental and numerical studies of Ar⁺-laser assisted Si doping of GaAs with SiBr₄ by chemical beam epitaxy", J. Crystal Growth, vol. 210, pp. 444-450 (2000).

B. Q. Shi, M. Kondow and C. W. Tu, "Chemical beam epitaxy of AlAs using novel group-V precursors", submitted to J. Crystal Growth (1999).

B. Q. Shi and C. W. Tu, "A study of Ar⁺-laser assisted Si doping of GaAs by chemical beam epitaxy", Appl. Phys. Lett., vol. 76, pp. 1716-1718 (2000).

B. Q. Shi and C. W. Tu, "An investigation on the mechanisms responsible for Ar⁺-laser induced growth enhancement of GaAs by chemical beam epitaxy", submitted to J. Crystal Growth (1999).

B. Q. Shi and C. W. Tu, "Localized doping enhancement by photon-assisted chemical beam epitaxy", accepted by 1999 MRS Spring Meeting Symposium Proceedings (1999).

B. Q. Shi and C. W. Tu, "Modeling study of silicon incorporation from SiBr₄ in GaAs layers grown by chemical beam epitaxy", J. Crystal Growth, vol. 195, pages 740-745 (1998).

B. Q. Shi and C. W. Tu (1998) "Laser-assisted chemical beam epitaxy of InP with trimethylindium and tertiarybutylphosphine", in *Light Emitting Devices for Optoelectronic Applications and the Twenty-Eighth State-of-the-Art Program on Compound Semiconductors*, edited by H. Q. Hou, R. E. Sah, S. J. Pearton, F. Ren and K. Wada, the Electrochemical Society, Inc., Pennington, New Jersey, pages 366-376 (1998).

B. Q. Shi and C. W. Tu, "A reaction model for chemical beam epitaxy with triethylgallium and tris(dimethylamino) arsine", submitted to J. Crystal Growth (1998).

B. Q. Shi and C. W. Tu, "A kinetic model for tris(dimethylamino) arsine decomposition on GaAs(100) surfaces", J. Electr. Mat., Vol. 28, No. 1, page 43-49 (1999).

B. Q. Shi and C. W. Tu, "Chemical beam epitaxy of InP with Ar⁺ laser irradiation", J. Electrochem. Soc., vol. 146 (7), 2679-2682 (1999).

B. Q. Shi and C. W. Tu (1997), "Simulation of chemical beam epitaxy with triethylgallium and tris(dimethylamino) arsine", in *Compound Semiconductors 1997*, edited by Mike Melloch and

Mark A. Reed, Institute of Physics Publishing, Philadelphia, Pennsylvania, pages 143-146 (1997).

M. Kondow, B. Q. Shi and C. W. Tu, "Chemical beam etching of GaAs using a novel precursor of tertiarybutylchloride (TBCl)", Jpn. Appl. Phys. Lett., vol. 38, L617-L619 (1999).

M. Kondow, B. Q. Shi and C. W. Tu, "In-situ etching using a novel precursor of tertiarybutylchloride (TBCl)", J. Crystal Growth, vol. 209, pp. 263-266 (2000).

C2 Presentations

B. Q. Shi, M. Kondow and C. W. Tu, "Chemical beam epitaxy of AlAs using novel group-V precursors", the 7th International Conference on Chemical Beam Epitaxy and Related Growth Techniques, Tsukuba, Japan, July 27-30, 1999.

B. Q. Shi and C. W. Tu, "An investigation on the mechanisms responsible for Ar^+ -laser induced growth enhancement of GaAs by chemical beam epitaxy", 1999 Electronic Materials Conference, Santa Barbara, California, June 30 through July 2, 1999.

B. Q. Shi and C. W. Tu, "Localized doping enhancement by photon-assisted chemical beam epitaxy", Materials Research Society 1999 Spring Meeting, San Francisco, California, April 5-9, 1999.

B. Q. Shi and C. W. Tu, "A study of metalorganic beam epitaxy of GaAs doped with SiBr_4 ", the 31st Annual Southern California Chapter of American Vacuum Society Symposium, Orange County, California, September 23, 1998.

B. Q. Shi and C. W. Tu, "Modeling study of silicon incorporation from SiBr_4 in GaAs layers grown by chemical beam epitaxy", the Ninth International Conference on Metal Organic Vapor Phase Epitaxy, La Jolla, California, May 31-June 4, 1998.

B. Q. Shi and C. W. Tu, "Laser-Assisted Chemical Beam Epitaxy of InP with Trimethylindium and Tertiarybutylphosphine", the 193rd Meeting of the Electrochemical Society, San Diego, California, May 3-8, 1998.

B. Q. Shi and C. W. Tu, "Simulation of chemical beam epitaxy with triethylgallium and tris(dimethylamino) arsine", the 24th International Symposium on Compound Semiconductors, San Diego, California, September 8-11, 1997.

B. Q. Shi and C. W. Tu, "A kinetic model for tris(dimethylamino) arsine decomposition on GaAs(100) surfaces", the 7th OMVPE Workshop, Dana Point, California, April 14-17, 1997.

M. Kondow, B. Q. Shi and C. W. Tu, "In-situ etching using a novel precursor of tertiarybutylchloride (TBCl)", the 7th International Conference on Chemical Beam Epitaxy and Related Growth Techniques, Tsukuba, Japan, July 27-30, 1999.